al-Farabi Kazakh National University

UDC 539.1(043) The manuscript

**YELEUSHEVA BADIGUL MARATOVNA**

# Radiative capture reactions on light nuclei in stellar and interstellar plasma

8D05308 – Nuclear Physics

Thesis for the degree
of Doctor of Philosophy (PhD)

Local scientific supervisor:
N.A. Burkova, Doctor of Physical and
Mathematical Science, Professor

Foreign scientific supervisor:
R. Kezerashvili, PhD, D.Sc., Professor
(City University of New-York, USA)

Republic of Kazakhstan
Almaty, 2025

## CONTENT

## SYMBOLS AND ABBREVIATIONS

| | |
|---|---|
| WF | wave function |
| MPCM | modified potential cluster model |
| BBN | Big Bang Nucleosynthesis |
| *NN* | nucleon-nucleon (interaction, potential, *etc*.) |
| b | barn, 1b= $10^{-24}$ $sm^2$ |
| μb | microbarn, 1 μb =$10^{-6}$ b |
| fm | fermi, 1 fm=$10^{-13}$ sm |
| MeV | mega-electronvolt |
| meV | milli-electronvolt |
| c.m. | center of mass system |
| l.s. | laboratory system |
| $E_b$ | binding energy |
| $s$ | spin of the target or the incident particle |
| $S$ | Channel spin |
| $C_{a\alpha\, b\beta}^{c\gamma}$ | Clebsch-Gordan coefficient |
| $P_n^m(\theta)$ | Legendre polynomial |
| $\begin{Bmatrix} a & b & c \\ d & e & f \end{Bmatrix}$ | 6j-symbol |
| $M_{S'\nu'}^{S\nu}$ | matrix elements of the transition *M*-matrix |
| $EJ$ | electrical multipole transitions of rank *J* |
| $MJ$ | magnetic multipole transitions of rank *J* |
| $d\sigma/d\Omega$ | differential cross section |
| $S$-factor | astrophysical factor |
| GS | ground state |
| ES | excited state |
| FS | forbidden state |
| AS | allowed state |
| $V_{ab}$ | binary interaction potential |
| ANC | asymptotic normalizing coefficient |
| AC | asymptotic constant |
| $\sigma_{therm}$ | thermal cross section |
| CNO | Carbon-Nitrogen-Oxygen |
| NO | Nitrogen-Oxygen |
| EFT | effective field theory |
| TISM | Translationally invariant shell model |

# INTRODUCTION

**General characteristics of the work.** The thesis presents model calculations of the reaction rates of radiative capture of neutrons on $^{8}$Li, $^{9}$Be and $^{13}$B nuclei and protons on the $^{15}$N isotope to assess scenarios for the evolution of light elements in stellar and interstellar plasma.

**Relevance of research.** Modern Nuclear Astrophysics is a field of theoretical and experimental research covering the most extensive aspects of fundamental and applied physics. One of the directions is associated with the study of nuclear reactions on light nuclei with $A \leq 16$ at low energies. This direction is a path for solving various astrophysical problems [1, 2]. Let us list only some of the most actual ones:

• *the early Universe's formation and evolution theory* is building and developing. So, one of the most critical questions that have not yet found an unambiguous solution is whether the primary cosmological environment is homogeneous or whether the *proton* and *neutron* components delamination occurred [3].

• *models for the synthesis of chemical elements* in the post-Big Bang Nucleosynthesis (BBN) period are developing based on the definition and study of temperature conditions relevant to the formation of various chains of nuclear reactions [4-7].

• based on well-founded nuclear chains, various versions of *networks* are building, which ultimately make it possible to calculate the mass fractions of both stable nuclei and radioactive isotopes, as well as justify different scenarios for the formation and, very importantly, the *accumulation of heavy isotopes*.

• considerable efforts by theorists and experimentalists are associated with evaluating the nuclear processes that form the *solar and stellar Carbon-Nitrogen-Oxygen* (CNO) cycles, which vary depending on the star's mass compared to the Sun's $M_{\odot}$. These data aim to calculate the macro characteristics such as luminosity, lifetime, and possible star rebirth scenarios (red dwarf, neutron star, or supernova).

In the context of the above, the reactions of radiative capture of nucleons on light nuclei ($N,\gamma$) play a distinctive, mainly determining role in nuclear astrophysics since hydrogen (i.e., protons) serves as the primary environment for natural thermonuclear processes, as a result of which secondary neutrons can be produced in significant quantities.

Laboratory studies of nuclear reactions of radiation capture are significantly limited in their capabilities due to objective reasons. The cross sections for reactions with protons $(p,\gamma)$ are strongly suppressed by the Coulomb barrier in the energy range specific for nuclear processes in stars. The known ratio 1eV ~ $1.16 \cdot 10^{4}$ K makes it possible to estimate the range of energies and temperatures of interest for astrophysical problems. For example, the temperature of the Sun is $T_6 \sim 1$ ($T_6 = 10^6$K). However, it is extremely difficult to measure the total reaction cross sections ($p,\gamma$) at energies of ~100 keV and below.

Today, the world's only all-European project The Laboratory for Underground Nuclear Astrophysics (LUNA) collaboration has made real progress in measuring the

cross sections of the radiative proton capture at ultra-low energies on light nuclei but conditioned by stable isotopes as targets [8-10].

The experimental base, which provides direct and indirect measurements of cross sections for radiative neutron $(n,\gamma)$ capture reactions, is today represented by many projects and modern installations equipped with contemporary techniques [11]. However, when dealing with short-lived isotopes, one faces a problem. For example, for the reaction $^{8}$Li($n,\gamma_{0+1}$)$^{9}$Li, only four experimental points are known at two energy values [12]. Measurements of cross sections for the reaction $^{13}$B($n,\gamma_{0+1}$)$^{14}$B are extremely uninformative [13].

Reviews of some successful theoretical models can be found in monographs [14]. In a modern review [15] comments and illustrations on microscopic models like "*ab initio*", effective field theory (EFT), the phenomenological *R*-matrix method, indirect methods, potential model, etc. are presented.

Each of these models has advantages but also constraints. For example, the *R*-matrix method is widely used to analyze reactions with charged particles, in particular ($p,\gamma$) reactions, but only if the total cross sections are provided by detailed measurements. Next, we will discuss this topic in more detail in relation to the reaction $^{15}$N($p,\gamma$)$^{16}$O. Other methods are also commented as necessary when compared with the modified potential cluster model (MPCM). Within MPCM, the results of calculated total cross sections for $^{8}$Li($n,\gamma_{0+1}$)$^{9}$Li, $^{9}$Be($n,\gamma_{0+1+2+3+4+5}$)$^{10}$Be, and $^{13}$B($n,\gamma_{0+1}$)$^{14}$B reactions are presented, as well as astrophysical *S*-factor of the reaction $^{15}$N($p,\gamma$)$^{16}$O, and the corresponding reaction rates.

**Purpose of research is** model calculations of the reaction rates of radiative neutron capture on $^{8}$Li, $^{9}$Be, and $^{13}$B nuclei and protons on isotope $^{15}$N for evaluation of light elements evolution scenarios in stellar and interstellar plasma.

**Research goals:**

1. To calculate the total cross sections and $^{8}$Li($n,\gamma_{0+1}$)$^{9}$Li reaction rate;
2. To calculate the total cross sections $^{9}$Be($n,\gamma_{0+1+2+3+4+5}$)$^{10}$Be reaction with formation of $^{10}$Be in GS and five excited states, as well as corresponding reaction rates;
3. Develop substantiated model approach for the investigation of $^{13}$B($n,\gamma_{0+1}$)$^{14}$B reaction at astrophysical energies. Calculate the total cross section and reaction rate;
4. Re-estimation of the astrophysical *S*-factors of $^{15}$N($p,\gamma$)$^{16}$O in MPCM including the interference effects and non-resonance magnetic dipole *M*1 transition. Evaluate the impact of these factors on the corresponding reaction rate.

**Research objects** are the binary cluster systems of light nuclei and mechanisms of radiative nucleon capture reactions at low and ultra-low energies.

**Research methods:** algebraic methods of the quantum theory of angular momentums, methods of quantum scattering theory, numerical methods for solving the Schrödinger equation of continuum and bound states, numerical integration.

**The connection of the thesis with research programs.**

The research work is carried out in accordance with the following programs:

1. "Study of the rates of some thermonuclear reactions in solar cycles and BBN" (IRN: AP09259021-OT-23, 2021-2023);

2. “Study of the processes of thermonuclear hydrogen combustion in the CNO cycle on the Sun and in stars” (IRN: AP19676483, 2023-2025);

**Scientific novelty:**

1. The total cross sections for radiative $n^8$Li capture at energies in the range from 10 meV to 5 MeV are obtained, which generally agree with the results of experimental measurements. For the first time, a model-free criterion for evaluating the reliability of the calculated reaction rates is proposed due to the binding energy in the nucleon channels $^6$Li$(n,\gamma)^7$Li , $^7$Li$(n,\gamma)^8$Li, and $^8$Li$(n,\gamma)^9$Li. The same criterion allows us to estimate the permissible range of asymptotic constants in the bound state.

2. The partial and total cross-sections of $^9$Be$(n,\gamma_{0+1+2+3+4+5})^{10}$Be reaction are calculated in the energy range from $10^{-5}$ to 5 MeV in the MPCM. The expansion of the energy range to 5 MeV allows to consider five resonances and estimate their signature in the total cross-section. The resonance of $E_x$ = 0.730 MeV is proposed as $^3F_2^1$ state, but not the *P* one as in [16]. Strong sensitivity of the cross sections on the asymptotic constant $C_w$ provided the proper long-range dependence of radial bound *S* wave functions is proved. New results on the complete reaction rate are obtained. Impact of resonances on the reaction rate is demonstrated.

3. The total cross sections of $^{13}$B$(n,\gamma_{0+1})^{14}$B reaction are calculated in MPCM based on *E*1 and *M*1 transitions from $10^{-2}$ eV to 5 MeV *for the first time*. Within the variation of the asymptotic constant, the interval for the thermal cross-section of 5.1- 8.9 mb is proposed. Based on the theoretical total cross-sections at energies of 0.01 eV to 5 MeV, the reaction rate is calculated in the temperature range of 0.01 to 10$T_9$. The ignition $T_9$ values of $^{13}$B$(n,\gamma_{0+1})^{14}$B reaction depending on the neutron number density $\overline{n}_n$ of ~ $10^{22}$ cm$^{-3}$ are determined.

4. For the first time the re-estimation of the astrophysical *S*-factor and reaction rate for the $^{15}$N$(p,\gamma)^{16}$O reaction in the framework of MPCM includes interference of low-lying $^3S_1$ resonances and *magnetic non-resonance M*1 *transition*. The simulation of considering the experimentally observed cascade transitions is suggested.

Comparative analyses of the reaction rates for $^{12}$N$(p,\gamma)^{13}$O, $^{13}$N$(p,\gamma)^{14}$O, $^{14}$N$(p,\gamma)^{15}$O, $^{15}$N$(p,\gamma)^{16}$O reactions involved into different branches of the CNO cycle obtained in the framework of the same model, MPCM is implemented. Temperature windows, prevalence, and significance of each process are determined. The comparison of the reaction rates indicates which slow reactions control the rate and time of cycles of oxygen isotopes nucleosynthesis at particular astrophysical temperatures.

5. For the first-time regularity “*the higher the channel threshold*, *the higher the reaction rate*” for neighbouring isotopes Li, B and N is formulated.

**Defense of Provisions:**

1. Two criteria found for the evaluation of $^8$Li$(n,\gamma_{0+1})^9$Li reaction rate allow to *narrow down* the range of reaction rates and *constrain* the choice of asymptotic constants: the values of thermal cross sections and *correlation* between the energy thresholds and order of reaction rates at low temperatures on lithium isotopes $^{6,7,8}$Li.

2. The partial and total cross-sections of $^9$Be$(n,\gamma_{0+1+2+3+4+5})^{10}$Be reaction calculated in the energy range from $10^{-5}$ to 5 MeV *allows to consider* five $^3D_3^1$, $^3F_2^1$,

$^3F_3$, $^3F_2^2$, and $^3D_3^2$ resonances and *estimate* their signature in the total cross-section. The inclusion of resonances shows their impact on the reaction rate within the factor 4-5 rising at $T_9$ >1, comparing the modern results of Wallner *et al*., 2019 and Mohr *et al*., 2019.

3. The calculations of the total cross sections of $^{13}$B($n$,$\gamma_{0+1}$)$^{14}$B reaction performed in MPCM from $10^{-2}$ eV to 5 MeV provide the proposal for new experimental measurements ISOLDE. The presented data on the reaction rates substantiate the role of $^{13}$B($n$,$\gamma_{0+1}$)$^{14}$B reaction in the Boron-Carbon-Nitrogen chains, this is not the *break-point* of the Boron sequence.

**Personal contribution of the author.** Badigul Yeleusheva took part in all stages of research, including the development the MPCM implementation for studying astrophysical processes of reactions $^8$Li($n$,$\gamma_{0+1}$)$^9$Li, $^9$Be($n$,$\gamma_{0+1+2+3+4+5}$)$^{10}$Be, $^{13}$B($n$,$\gamma_{0+1}$)$^{14}$B and $^{15}$N($p$,$\gamma$)$^{16}$O. Research work was carried out at al-Farabi Kazakh National University, as well as during a foreign internship held at the City University of New York (CUNY, New York, USA, 2023).

**The reliability** of the results, first of all, is due to the fact that the calculations use the algebraic methods of the quantum theory of angular momentum. Moreover, the construction of interaction potentials and calculations of the characteristics of radiative capture reactions based on modern experimental data on level spectra, their width, ACs, cross sections and astrophysical *S*-factors. The reliability and validity of the results is also confirmed by publications in journals recommended by the Committee for Control of Education and Science of the Ministry of Education and Science of the Republic of Kazakhstan, as well as in the proceedings of international scientific conferences.

**Theoretical and practical significance.**

The results of calculations of the reaction cross sections $^8$Li($n$,$\gamma_{0+1}$)$^9$Li and $^{13}$B($n$,$\gamma_{0+1}$)$^{14}$B within the framework of MPCM actually provide a justification for setting up new experimental measurements both at thermal energies and in an extended range up to 5 MeV . It should be noted that the R-matrix approach is in principle not applicable to these reactions. For the reaction $^9$Be($n$,$\gamma_{0+1+2+3+4+5}$)$^{10}$Be, energy regions for which refined experimental data are required are also determined.

Reaction rates $^8$Li($n$,$\gamma_{0+1}$)$^9$Li, $^9$Be($n$,$\gamma_{0+1+2+3+4+5}$)$^{10}$Be, $^{13}$B($n$,$\gamma_{0+1}$)$^{14}$B and $^{15}$N($p$,$\gamma$)$^{16}$O are recommended include in databases.

Reaction rates are calculated by averaging particles over velocities in the plasma according to the Maxwell equilibrium distribution. This distribution assumes a homogeneous model of the Universe. The obtained reaction rates can be taken as a basis for conducting promising studies of the effects of considering the weak non-ideality of stellar plasma, using Tsallis statistics instead of Maxwell statistics.

It is important to continue research to test the hypothesis related to the pattern "*the higher the channel threshold, the higher the reaction rate*" using extended data for neighboring isotopes. This information is of great practical importance both for theoretical model calculations - clarification of model parameters, and for qualitative estimates of reaction rates at low temperatures.

**Research approbation and publications.**

The main results from the dissertation were published in foreign scientific journals with impact-factor: *Frontiers in Astronomy and Space Sciences* [17], *Chinese Physics C* [18-20], also were reported and discussed at the following conferences: *No. XXVII (2022) European Academic Science and Research* [21], *25th European Conference on Few-Body Problems in Physics* (EFB25) (30 July- 4 August, 2023, Mainz, Germany [22].

Publications in scientific journals included and indexed in the Scopus\Web of Science database:

– Dubovichenko S.B., **Yeleusheva B.M.**, Burkova N.A., Tkachenko A.S. The reaction rate of radiative $n^8$Li capture in the range from 0.01 to 10$T_9$ // Frontiers in Astronomy and Space Sciences. – 2023. – Vol. 10. – 1251743.

– Tkachenko A.S., Burkova N.A., **Yeleusheva B.M.**, Dubovichenko S.B. Estimation of radiative capture $^{13}$B($n$,$\gamma_{0+1}$)$^{14}$B reaction rate in the modified potential cluster model // Chinese Physics C. – 2023. – Vol. 47. – 104103.

– Dubovichenko S.B., **Yeleusheva B.M.**, Burkova N.A., Tkachenko A.S. Radiative $^9$Be($n$,$\gamma_{0+1+2+3+4+5}$)$^{10}$Be reaction rate in the potential cluster model // Chinese Physics C. – 2023. – Vol. 47. – 084105.

– Dubovichenko S.B., Tkachenko A.S., Kezerashvili R.Ya., Burkova N.A., **Yeleusheva B.M.** Astrophysical S-factor and reaction rate for $^{15}$N($p$,$\gamma$)$^{16}$O within the modified potential cluster model // Chinese Physics C. – 2024. – Vol. 48. – 044104.

**Thesis structure and volume.** The thesis consists of Introduction, five sections, Conclusion, References. It contains 29 figures and 22 tables. References consists of 196 items. The thesis is set out on 105 pages of printed text.

# 1 THE MPCM APPROACH FOR THE DESCRIPTION OF A NEUTRON AND PROTON INDUCED RADIATIVE CAPTURE REACTIONS ON LIGHT NUCLEI

## 1.1 Theoretical model and formalism

The considered two-particle MPCM is very easy to use since it reduces to solving the problem of two bodies, which is equivalent to the problem of one body in the field of a force center. Therefore, an objection may arise that this model is entirely inadequate for the problem of many bodies, which is the problem of describing the properties of a system consisting of $A$ nucleons. However, this is not entirely true, and further, we will answer this question by explaining the evolution of the cluster system state during the reaction.

Usually, wave functions (WFs) in any cluster model are chosen to correspond to the ground states of nuclei consisting of $A_1$ and $A_2$ nucleons. The total wave functions have the form of an antisymmetrized product of completely antisymmetric internal wave functions of clusters $\Psi(1,\ldots A_1) = \Psi(R_1)$ и $\Psi(A_1+1,\ldots, A) = \Psi(R_2)$ multiplied by the wave function of their relative motion $\Phi(\boldsymbol{r} = \boldsymbol{R}_1 - \boldsymbol{R}_2)$ [23-25]:

$$\Psi = \hat{A}\ \{\Psi(\boldsymbol{R_1})\Psi(\boldsymbol{R_2})\Phi(\boldsymbol{r})\}, \tag{1.1}$$

where $\hat{A}$ is the antisymmetrization operator, acting concerning permutations of nucleons from different clusters of the nucleus, $\boldsymbol{r}$ is the intercluster distance, $\boldsymbol{R_1}$ and $\boldsymbol{R_2}$ are the radius vectors of the mass center of the clusters.

These wave functions are characterized by specific quantum numbers, including *JLS* and Young's diagrams $\{f\}$, they determine the orbital part of WF permutation symmetry of the relative motion of the clusters [24, 25]. In the general case, the possible Young's orbital diagram $\{f\}_L$ of some nucleus $A(\{f\})$, consisting of two parts $A_1(\{f_1\}) + A_2(\{f_2\})$, is the direct outer product of Young's orbital diagrams of these parts $\{f\}_L = \{f_1\}_L \times \{f_2\}_L$ and is determined by the Littlewood theorem [24, 25]. According to Elliot's theorem, each Young's diagram is associated with a certain orbital angular momentum or their combination [24, 25]. For example, the possible orbital Young diagrams of the $p^2$H system, when the {2} diagram is used for the $^2$H nucleus, turn out to be {3}L and {21}L symmetries. The first corresponds to the orbital momentum $L$ = 0, and the second $L$ = 1. For the $p^6$Li system, with the diagram {42} for $^6$Li, we have a possible combination of {52}, {43}, and {421} symmetries. The first of them corresponds to the orbital moment $L$ = 0, 2, the second $L$ = 1, 3, and the third $L$ = 1, 2 [26, 27].

Spin-isospin diagrams are a direct inner product of the spin and isospin Young diagrams of a nucleus from $A$ nucleons $\{f\}_{ST} = \{f\}_S \otimes \{f\}_T$ and for a system with no more than eight particles are given in [28]. For any of these moments (spin or isospin), the corresponding diagram of a nucleus consisting of $A$ nucleons, each of which has a moment equal to 1/2, is constructed as follows. The cells of the first line indicate the number of nucleons that have moments directed in one direction, for example, upwards. In the cells of the second line, if required, the number of nucleons with moments directed in the other direction, for example, down. The total number of cells

in both rows equals the number of nucleons in the nucleus. The moments of the nucleons in the first row, which have a pair in the second row with oppositely directed momentum, are compensated and have, as a result zero total momentum. The sum of the nucleon moments of the first row, which are not compensated by the nucleon moments from the second row, gives the value of the total moment of the entire system [29].

The complete Young diagram of the nucleus is defined similarly as the direct inner product of the orbital and spin-isospin diagrams $\{f\} = \{f\}_{\mathrm{L}} \otimes \{f\}_{\mathrm{ST}}$. The total wave function of the system under antisymmetrization does not vanish identically only if it contains the antisymmetric component $\{1^{\mathrm{A}}\}$, which is realized by multiplying the conjugates $\{f\}_{\mathrm{L}}$ and $\{f\}_{\mathrm{ST}}$. Therefore, diagrams $\{f\}_{\mathrm{L}}$ conjugate to $\{f\}_{\mathrm{ST}}$ are allowed in this channel, and all other orbital symmetries are forbidden since they lead to zero total wave function of the system of particles after its antisymmetrization. Each Young orbital diagram corresponds to a certain state of two particles in relative motion. Therefore, we conclude that in such a system, there are forbidden states (FS) and allowed states (AS) in terms of the relative motion of particles. And if there is a FS in a certain partial wave with a given $L$, then the WF of the AS will have a node since this state will be the second with higher energy in the spectrum of levels of this potential.

For bound states (BS) of two clusters in a nucleus, the interaction potentials within the framework of the MPCM are built primarily based on the requirement to describe the main characteristics of such a nucleus. In this case, the parameters of the potentials, according to the known characteristics of the ground states (GS) of the nuclei, are fixed quite definitely. However, such a requirement is an idealization of the situation in the nucleus since it assumes that there is 100% clustering in the ground state into a two-particle channel. Therefore, the success of this potential model in describing a system of $A$ nucleons in a bound state is determined by how significant the actual clustering of this nucleus in the $A_1$+ $A_2$ nucleon channel is.

However, some nuclear characteristics of the individual, even non-cluster, nuclei can be predominantly due to one specific cluster channel, which has a certain cluster structure with a small contribution from other possible cluster configurations. In this case, the single-channel cluster model used makes it possible to identify the dominant cluster channel and highlight those properties of the nuclear system that are due to it [8]. In addition, the concept of states forbidden by the Pauli principle makes it possible to qualitatively take into account the many-particle nature of the problem in terms of the two-particle interaction potential between clusters [30]. This is another reason why we continue to study the possibilities of MPCM and its applicability for describing a certain range of characteristics of atomic nuclei and thermonuclear reactions.

In addition, when we talk about the probability of the existence of a certain cluster channel in the nucleus, we mean a certain stationary, static state of this nucleus, which does not depend on time, i.e., exists long enough to be considered stationary. At the same time, in certain reaction radiative capture, a dynamic occurs, i.e., a time-dependent transformation in which a pair of clusters from a continuous spectrum of states at positive energy passes into a state at negative energy, i.e., states of the discrete spectrum. It is quite possible to assume that the measurement of the cross sections of such a reaction occurs immediately after its occurrence, i.e., when the final nucleus

was just formed, emitted a γ-quantum, and is not yet stationary. Therefore, it is clear that at these initial moments, the resulting final nucleus is located with almost 100% probability in a channel consisting of initial particles. This can explain the quite apparent success of the MPCM in describing the total cross sections of already 40 reactions of the radiative capture type under the assumption of almost complete clustering of the final nucleus into the initial channel [26, 27] and [31, 32] (and references in these works, and results for $n^{12}$B and $n^{13}$B).

So, let's formulate the basic principles of MPCM and illuminate the differences from the previously used approaches:

1. First, the cluster states are classified according to Young's orbital diagrams, which leads to the concept of FS in some partial waves [26, 27] or [33].

2. Construction of intercluster interaction potentials of the Gaussian type, taking into account these FSs in certain partial waves with a given orbital momentum $L$.

3. The Pauli principle is taken into account due to the use of the FS - MPCM bond, the shell model, and the model of nucleon associations given in [29] or [26, 27].

4. FSs lead to low-lying BSs that exist in intercluster partial potentials and are not physically realized due to the orthogonality of their WFs and ASs functions.

5. For each partial wave with a given orbital momentum and other quantum numbers, $J$, $L$, $S$, and $\{f\}_L$ construct its Gaussian-type potential, which has two parameters, i.e., an explicit dependence of the potential parameters on the orbital diagrams of Young is assumed.

6. The BS potentials are built based on the description of the AC values and the binding energies of such states. Their parameters do not change in the process of calculations or can vary only within the limits of the AC errors since the BS energies are determined very accurately.

7. Potentials of scattering processes are built based on the description of the spectra of the final nucleus or the scattering phases of the particles of the input channel. The parameters of such potentials can only exist within the limits of the energy errors or the widths of the resonant or excited states.

8. As a result, all parameters of the potentials are determined quite unambiguously; if required, they take into account the FS and do not change in the process of calculations of the radiative capture reactions. No additional variation of their parameters for a better description of the available experimental data for the total cross sections or $S$-factors of radiative capture processes is allowed [26, 27].

9. The model is two-particle, but it is built by considering the internal characteristics of clusters - their sizes, charges and masses, quadrupole, and magnetic moments if required to perform calculations of total cross sections or other characteristics of the final nucleus. For example, the magnetic moments of clusters are taken into account when considering $M1$ transitions from scattering states to the BS of the final nucleus. Cluster radii are considered when calculating the final nucleus's size [34]. The quadrupole moments of clusters are considered when calculating the quadrupole moment of the final nucleus [34-38].

10. The WFs of the continuous spectrum of allowed state are matched with their asymptotics, from which the scattering phases and normalizations of such WFs are

determined. The WFs of the discrete spectrum of allowed state are linked with their asymptotics, from which their ACs of such states are determined .

### 1.2 Total cross-section for (*n*,γ) processes. Definitions

We use the well-known formulas for the total cross sections and matrix elements of the operators of electromagnetic transitions [26, 27]. These expressions were given in a similar form in review [39]:

$$\sigma_c(NJ,J_{\rm f}) = \frac{8\pi K e^2}{\hbar^2 k^3}\frac{\mu}{(2S_1+1)(2S_2+1)}\frac{J+1}{J[(2J+1)!!]^2}A_{\rm J}^2(NJ,K)\times \\ \times\sum_{\rm L_i,J_i} P_{\rm J}^2(NJ,J_{\rm f},J_{\rm i})I_{\rm J}^2(J_{\rm f},J_{\rm i}), \tag{1.2}$$

where $K$ – photon wave number, $k$ is wave number related to the nonrelativistic energy in initial center of mass, $\mu$ is reduced mass; $S_1$ and $S_2$ are spin of particles, $A_J$ – reduced matrix elements for $NJ$ multipole transition $NJ = EJ$ or $MJ$, $P_J$ – algebraic factor providing selection rules, $I_J$ – overlapping integrals.

In Eq. (1.2) the matrix elements of $EJ$ - transitions have the following form:

$$P_J^2(EJ,J_f,J_i) = \delta_{S_iS_f}[(2J+1)(2L_i+1)(2J_i+1)(2J_f+1)]\times \\ \times(L_i0J0\,|\,L_f0)^2\begin{Bmatrix} L_i & S & J_i \\ J_f & J & L_f \end{Bmatrix}^2, \tag{1.3}$$

$$A_J(EJ,K) = K^J\mu^J\left(\frac{Z_1}{m^J{}_1}+(-1)^J\frac{Z_2}{m^J{}_2}\right), \tag{1.4}$$

$$I_J(J_f,J_i) = \left\langle \chi_f \left| r^{\rm J} \right| \chi_i \right\rangle. \tag{1.5}$$

Here $S_i, S_f, L_f, L_i, J_f$ and $J_i$ are the total spins and moments of the particles of the initial ($i$) and final ($f$) channels, $m_1, m_2, Z_1, Z_2$ are the masses and charges of the particles of the initial channel, $I_J$ is the integral over the wave functions of initial $\chi_i$ and final $\chi_f$ states as functions of relative motion of clusters with intercluster distance $R$.

For the spin part of the magnetic process $M1(S)$ at $J = 1$, the following expression is obtained $(S_i = S_f = S, L_i = L_f = L)$:

$$P_1^2(M1, J_f, J_i) = \delta_{S_i S_f} \delta_{L_i L_f} \times$$

$$\times \left[ S(S+1)(2S+1)(2J_i+1)(2J_f+1) \right] \begin{Bmatrix} S & L & J_i \\ J_f & 1 & S \end{Bmatrix}^2, \tag{1.6}$$

$$A_1(M1, K) = i \frac{\hbar K}{m_0 c} \sqrt{3} \left( \mu_1 \frac{m_2}{m} - \mu_2 \frac{m_1}{m} \right), \tag{1.7}$$

$$I_J(J_f, J_i) = \left\langle \chi_f \left| r^{J-1} \right| \chi_i \right\rangle. \tag{1.8}$$

Here $m$ is the mass of the nucleus, $\mu_1$, $\mu_2$ are the magnetic moments of the clusters, and the rest of the designations are the same as in the previous expression.

## 2 FORMATION OF PRIMORDIAL $^{9}$Li IN $^{8}$Li($n,\gamma$)$^{9}$Li REACTION

### 2.1 Lithium experiment. Lithium Problem

The implication of an $^{8}$Li($n,\gamma$)$^{9}$Li reaction is under discussion since it was included in the following primordial nucleosynthesis chain suggested by Mao and Champagne [40] and Kajino [3]:

$$\ldots{}^{7}\mathrm{Li}(n,\gamma)^{8}\underline{\mathrm{Li}(n,\gamma)^{9}\mathrm{Li}}(\alpha,n)^{12}\mathrm{B}(\beta^{+})^{12}\mathrm{C}\ldots. \qquad (2.1)$$

The experimental study of the $^{8}$Li($n,\gamma$)$^{9}$Li reaction performed using the Coulomb dissociation method reported in [12] is still the only study since 1998 and provides only two cross-section points. The promising prospect for new experimental measurements is reported in the recent proposal of the study of the breakup of $^{9}$Li on a $^{208}$Pb target at a different energy regime [41]. This process is included in one of the chains of primordial nucleosynthesis.

Since this reaction plays a bridge role from the synthesis of light seed nuclei $A \leq 7$ to the heavy elements, theoretical model calculations are in high demand. The early theoretical calculations of cross sections and reaction rates presented in [40, 42-51] differ significantly from each other. A modern investigation of the $^{8}$Li($n,\gamma$)$^{9}$Li reaction is provided by microscopic models in [52, 53].

It is important to note that along with the sequence (2.1), other branching options involving $^{8}$Li are possible: for example, the chain $^{7}$Li($n,\gamma$)$^{8}$Li($\alpha,n$)$^{11}$B($n,\gamma$)$^{12}$B($\beta^{+}$)$^{12}$C was suggested as a possible explanation for the production of $A \geq 12$ nuclides, observed in very metal-poor stars [54]. This suggestion raised a series of studies of the $^{8}$Li($\alpha,n$)$^{11}$B reaction, covering the test of an inhomogeneous Big Bang model [55], as well as CNO BBN at temperatures $T_9 = 0.5 - 1.2$ [56]. The key role of the $^{8}$Li($\alpha,n$)$^{11}$B reaction is recognized in the production of seed nuclei at $T_9$=2.5-5 later burnt to heavier elements via *r*-capture reactions, during type II supernova explosion [57]. It is worth noting that the reaction $^{8}$Li($\alpha,n$)$^{11}$B has been more extensively studied than the radiative neutron capture on $^{8}$Li, but their rates differ from each other within an order of magnitude [58]. Hence, the continuation of the $^{7}$Li($n,\gamma$)$^{8}$Li chain remains an open area of investigation, and further studies are needed. Specifically, there is no definitive conclusion regarding the comparability of the reaction rates for $^{8}$Li($n,\gamma$)$^{9}$Li and $^{8}$Li($\alpha,n$) $^{11}$B during the crucial temperature range of a standard BBN from $T_9$ = 0.1 - 1.

Present consideration of the $^{8}$Li($n,\gamma$)$^{9}$Li reaction is performed in the framework of the MPCM. This model is based on classifying discrete and continuum orbital states by Young diagrams {f}, which effectively includes the Pauli principle while constructing the corresponding wave functions. The results [59] need to be considered due to recent research on the $^{7}$Li($n,\gamma$)$^{8}$Li reaction [60]. It was suggested that for the $^{8}$Li nucleus, it is necessary to use the Young diagram {431} instead of {44}, assumed previously in [59]. Such a diagram changed the entire structure of forbidden and allowed states for the interaction potentials in the $n$ + $^{8}$Li channel. Therefore, we examined this effect while calculating the total cross sections and reaction rates. The

low-lying resonance at $J^{\pi} = 5/2^{-}$ at the energy $E_x = 4.296(15)$ MeV is considered in comparison with results in [59].

Recently, the properties of $^{9}$Li-bound states and low-lying resonances were studied within the no-core shell model with continuum [52]. The authors note that the *ab initio*-calculated $^{7}$Li($n,\gamma$)$^{8}$Li total cross section at the energies 20 keV to 1.6 MeV in the center-of-mass reference frame is nearly a factor two higher than results in [59]. In the present work, we explain the origin of this discrepancy and come to an acceptable agreement with [52]. The results of the low-temperature reaction rates at $T_9 < 1$ still remain in question. Radiative neutron capture reaction rates on $^{6,7,8}$Li nuclei are compared to estimate the "neutron poisoning" lithium isotope destruction.

### 2.2 Classification of orbital states and structure of $^{9}$Li

For the $^{8}$Li nucleus, as was shown in [60], we consider the Young orbital diagram {431}, so for the $n^{8}$Li system, we have: {431} + {1} = {531} + {441} + {432}. The diagram {531} corresponds to $L$ = 1,2,3 and is forbidden since the *s*-shell cannot contain five nucleons [24]. Allowed diagrams {441} and {432} may be put in compliance with the GS of the $^{9}$Li nucleus in the $n^{8}$Li channel alone with the orbital angular momentum $L$ = 1. Following [24], the scattering states turn out to be mixed by {441} + {432} diagrams, while the bound states refer only to the {441} diagram. It should be noted that FSs appear as bound only in both discrete and continuous spectra.

To reconstruct the GS total angular momentum, parity, and isospin, $T$ = 3/2$^{-}$, 3/2 of $^{9}$Li, we used the $^{8}$Li data, $J^{\pi},T = 2^{+},1$ obtained by [61]. The spin channel $^{n+8}$Li is defined by the vector addition of $^{8}$Li and n total spins, i.e., $S = 2 + 1/2$, and allows two states $S$=3/2 and $S$=5/2. Therefore, a spin-mixed $^{4+6}P_{3/2}$ state is possible for the GS (in the spectral notation $^{2S+1}L_J$), but we consider it a pure $^{4}P_{3/2}$ state. There is only one excited state at an energy of 2.691(5) MeV relative to the GS and binding energy $E_{\rm b}$ = −1.3729(5) MeV. The first excited state (1$^{\rm st}$ ES) with $J^{\pi} = 1/2^{-}$ is assumed a $^{4}P_{1/2}$ state.

Figure 2.1 illustrates the spectrum of the $^{9}$Li nucleus in the $n^{8}$Li channel. The reliable, experimentally confirmed complete data on the total angular momentum, parity, excitation energy $E_x$, and width $\Gamma_{c.m}$ are known for the first resonant state only [61, 62].

This state with $J^{\pi} = 5/2^{-}$ is located at an excitation energy $E_x$ = 4.296(15) MeV relative to GS or 0.232(15) MeV relative to the threshold energy $E_{th}$ of the $n^{8}$Li channel. Such a state is considered as a quartet $^{4}P_{5/2}$ wave. In [63, 64] reported the width $\Gamma_{c.m.}$= 100(30) keV. Based on these data, it is possible to construct a completely unambiguous $^{4}P_{5/2}$ elastic scattering potential with a bound FS. The variations in potential parameters may come only within the accuracy of the resonance width.

The second excited state at $E_x$ = 5.38(6) MeV [1.32(6) MeV above $E_{th}$] with the width $\Gamma_{\rm c.m.}$ = 600(100) keV is identified as a 3/2$^{-}$ state in recent works [52]. For the third excited state, experimental data provide a value of $E_x$ at 6.430(15) MeV and $\Gamma_{c.m}$ = 40(20) keV, but the total angular momentum and parity 7/2$^{-}$ were only predicted in [52]. We consider the strong $E$1 and $M$1 transitions as the estimation of $E$2 transition shows its minor role [59].

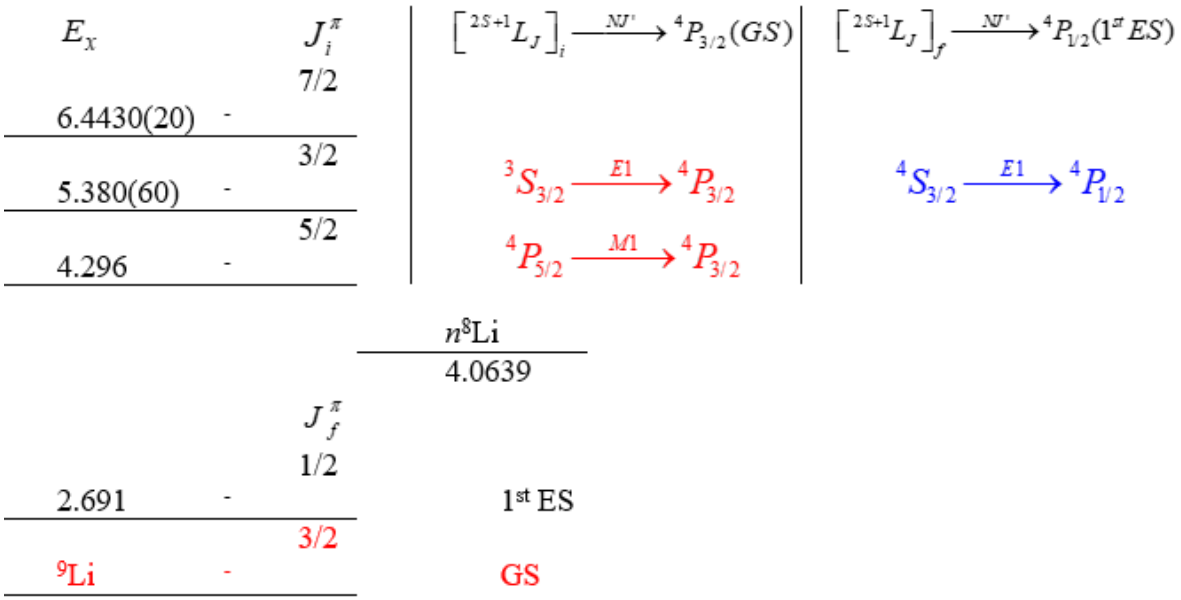


Figure 2.1 – Energy spectrum of $^9$Li in MeV

The Table 2.1 presents all treated transitions to the ground and first excited states of $^9$Li in the $n^8$Li channel and $P_J^2(NJ, J_f, J_i)$ coefficients – Eqs. 1.3, 1.6. The $E1$ dipole capture occurs from the ${}^4S_{3/2}$ scattering wave to the ${}^4P_{3/2}$ GS of $^9$Li. Since we assume that the potentials depend on the Young diagrams, the scattering and bound states have different sets of Young diagrams, and transitions between states with the same angular momentums are allowed.

Table 2.1 – Multipole transitions to GS and 1st ES of the $^9$Li nucleus in the $n^8$Li channel and coefficients $P_J^2(NJ, J_f, J_i)$ in expressions (1.3) and (1.6)

| No. | $[^{2S+1}L_J]_i$ | Transitions | $[^{2S+1}L_J]_f$ | $P_J^2(NJ, J_f, J_i)$ |
|---|---|---|---|---|
| 1 | ${}^4S_{3/2}$ | $E1$ | ${}^4P_{3/2}$ | 4 |
| 2 | ${}^4P_{1/2}$ | $M1$ | ${}^4P_{3/2}$ | 10/3 |
| 3 | ${}^4P_{3/2}$ | $M1$ | ${}^4P_{3/2}$ | 121/15 |
| 4 | ${}^4P_{5/2}$ | $M1$ | ${}^4P_{3/2}$ | 18/5 |
| 6 | ${}^4S_{3/2}$ | $E1$ | ${}^4P_{1/2}$ | 2 |
| 7 | ${}^4P_{1/2}$ | $M1$ | ${}^4P_{1/2}$ | 25/6 |
| 8 | ${}^4P_{3/2}$ | $M1$ | ${}^4P_{1/2}$ | 10/3 |

### 2.3 Construction of interaction potentials

To construct the interaction potentials for the scattering states, we used the resonant-state parameters $E_x$, $\Gamma_{c.m.}$ and $J^\pi$. Non- resonant waves are provided by the potentials leading to the phase shifts close to zero (if there are no FSs), or to 180° if such a state appears in the classification of orbital states according to the Young diagrams.

The parameters of bound state potentials are conditioned by reproducing the data

on the binding energy, matter, and charge radii, and the asymptotic constant [26, 27].

The nuclear two-body interaction potential is represented as a Gaussoid [26, 27]:

$$V(r, SLJ, \{f\}) = -V_0(SLJ, \{f\}) \exp\left[-\alpha(SLJ, \{f\}) r^2\right]. \quad (2.2)$$

### 2.4 Continuous spectrum

The potential parameters of Eq. 2.2 are listed in Table 2.2. These reproduce well the data on the $^4P_{5/2}$ and $^4P_{3/2}$ resonant states in [61, 62]. As for the non-resonant state $^4P_{1/2}$, the corresponding potential is deep enough to include the FS. The *S*-wave does not appear in the $^9$Li spectrum neither as the bound state nor as the resonant state. Therefore, the corresponding potential in Table 2.2 might lead to zero or near-zero phase shifts.

Table 2.2 – Parameters of interaction potentials of $n^8$Li continuum

| No. | $[^{2S+1}L_J]_i$ | $V_0$, MeV | α, fm$^{-2}$ | $E_{res}$, keV | $\Gamma_{c.m.}$, keV |
|---|---|---|---|---|---|
| 1 | $^4P_{5/2}$ | 240.87 | 0.3 | 230(1) | 109(1) |
| 2 | $^4P_{3/2}$ | 1,608.185 | 2.0 | 1,320(10) | 608(10) |
| 3 | $^4P_{1/2}$ | 520.0 | 1.0 | – | – |
| 4 | $^4P_{3/2}$ | 20.0 | 1.0 | – | – |

The corresponding calculated phase shifts are shown in Figure 2.2. The $\delta_{^4P_{5/2}}$ and $\delta_{^4P_{3/2}}$ phase shifts reveal the resonant energy dependence. The non-resonant $\delta_{^4P_{1/2}}$ phase shift corresponds to the potential with the forbidden state No. 3 given in Table 2.2. In accordance with the generalized Levinson theorem, this phase shift starts from 180° [24]. For the non-resonant $^4S_{3/2}$ scattering wave, the parameter no. 4 in Table 2.2 is found, and the corresponding $\delta_{^4S_{3/2}}$ phase shift shows smooth energy dependence, as shown in Figure 2.2.

The comparison between phase shifts obtained in the MPCM and *ab initio* NCSMC calculations (digitalized] data obtained in [52]) is shown in Figure 2.2. Phase shifts $\delta_{^4P_{3/2}}$ illuminate rather well the agreement of both models within ~10° at the energies following the resonance at 230 keV. $\delta_{^4S_{3/2}}$ phase shifts are also very close up to ~3,500 keV, and the difference rises up to ~20° at the edge of the treated energy interval $E_{c.m.}$ = 5 MeV. The visual distinction is observed in the energy dependence of $\delta_{^4P_{3/2}}$ shifts, both in the resonance position and in the whole energy range. In advance, we may state that the $^4P_{3/2}$ wave provides a second very wide resonance at 1.320 MeV in cross sections via *M*1 transition and plays a moderate role.

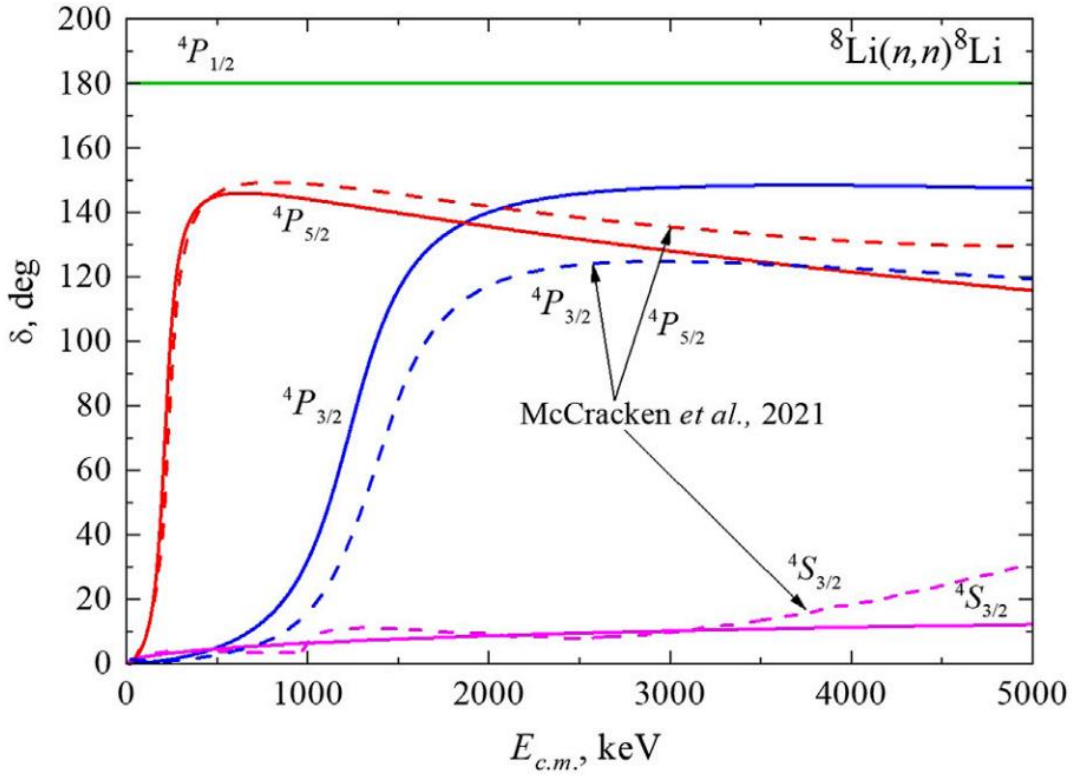


The solid curves are the results of MPCM calculations with the potential parameters given in Table 2.2; dashed curves are *ab initio* results obtained in [52] (digitalized).

Figure 2.2 – Phase shifts of elastic $n^8$Li scattering

### 2.5 Discrete spectrum

The following data on the ANC are considered to build the GS potential. The experimental values are deduced from the data on the neutron transfer reaction $^8$Li($d$,$p$)$^9$Li$_{g.s.}$ obtained in [65]. $A_{NC}$ = 0.96(8) fm$^{-1/2}$, and in the study in [61], $A_{NC}$ = 1.15(14) fm$^{-1/2}$. Their average value $A_{NC}$ = 1.06(10) fm$^{-1/2}$ agrees with the results obtained in [66], who reported a calculated value of 1.08 fm$^{-1/2}$ for $A_{NC}$ GS. In [66] also provided theoretical values of the spectroscopic factors 0.6 and 1.1 obtained by two methods, which correspond to an average value of $S_F$ = 0.85(25). Other data on the spectroscopic factors are given in Table 2.3.

Estimation within the aforementioned limits for $A_{NC}$ = 0.88 – 1.29 fm$^{-1/2}$, and the range for the spectroscopic factor $S_F$ = 0.44 – 1.03 (Table 2.3) results in $C_w$ = 0.95 – 2.03. In recent ab initio extended network calculations, $A_{NC}$ = 1.23(6) fm$^{-1/2}$ was reported, along with spectroscopic factors $S_F$ = 0.83 – 1.06 [67]. At the edges of these intervals, we obtain $C_w$ = 1.30 – 1.42. In [68] obtained, for the first ES of the $^9$Li nucleus, $A_{NC}$ = 0.4 fm$^{-1/2}$ (unfortunately, no uncertainties are available) at $S_F$ = 0.55, which leads to C = 0.54 fm$^{-1/2}$ or the dimensionless constant $C_w$ = 0.77 at $S_F$ = 0.698. In CDFE (2023) for GS, the calculations yield $A_{NC}$ = 1.140(13) fm$^{-1/2}$, and for the first ES, $A_{NC}$ = 0.308(7) fm$^{-1/2}$, which leads to $C_w$ = 0.60(1) at $S_F$ = 0.55. [66] reported, for the first ES, $A_{NC}$ = 0.33 fm$^{-1/2}$ at $S_F$ = 0.38(6), which yields $C_w$ = 0.76(4). The potential

parameters for the bound ground and excited states of the $^9$Li in $n^8$Li channel are summarized in Table 2.4. In the present calculations, we use an $^8$Li radius equal to 2.327 ± 0.0298 fm [69]. The radius of $^9$Li is 2.2462 ± 0.0315 fm [69, 70] used radii values 2.299(32) fm for $^8$Li and 2.217(35) fm for $^9$Li. In [71] obtained, for these radii, 2.30(4) fm and 2.24(4) fm. The neutron charge radius is assumed to be zero, and the mass radius of 0.8414 fm coincides with the known proton radius (NIST, 2019). The upper and lower sets refer to the GS and first ES interaction potentials, respectively, defined in Table 2.4, and differ by the $C_w$ values but lead to the same binding channel energy.

Table 2.3 – Spectroscopic factors for the GS of $^9$Li in the $n$ + $^8$Li channel

| Reference | Reaction from which $S_F$ is determined | Spectroscopic factor for $n$ +$^8$Li$_{GS}$ |
|---|---|---|
| Li *et al.* (2005) [48] | $^8$Li($d$,$p$)$^9$Li | 0.68 (14) |
| Wuosmaa *et al.* (2005) [72] | $^2$H($^8$Li,$p$)$^9$Li | 0.90 (13) |
| Wiringa (2021) [73] | $^9$Be($^8$Li, $^9$Li) $^8$Be | 0.62 (7) |
| Kanungo *et al.* (2008) [74] | $d$($^9$Li,$t$)$^8$Li | 0.65 (15) |
| | $d$($^9$Li,$t$)$^8$Li | 0.59 (15) |
| | Value interval | 0.44–1.03 |
| | Mean value | 0.74 (30) |

Table 2.4 – Parameters of the bound ground and excited state potentials of the $^9$Li in $n^8$Li channel and calculated asymptotic constant $C_w$, $R_{ch}$, and $R_m$ radii, and binding energy $E_b$

| No. | $[^{2S+1}L_J]_i$ | $V_0$, MeV | $\alpha$, fm$^{-2}$ | $C_w$ | $R_{ch}$, fm | $R_m$, fm | $E_b$, MeV | Set |
|---|---|---|---|---|---|---|---|---|
| 1 | $^4P_{3/2}$, GS | 295.28320 | 0.33 | 1.40(1) | 2.36 | 2.43 | 4.06390 | Upper |
| 2 | $^4P_{3/2}$, GS | 600.07219 | 0.70 | 0.93(1) | 2.35 | 2.35 | 4.06390 | Lower |
| 3 | $^4P_{1/2}$,1$^{st}$ES | 295.6387 | 0.35 | 0.77(1) | 2.37 | 2.37 | 1.37290 | Upper |
| 4 | $^4P_{1/2}$,1$^{st}$ES | 581.05205 | 0.07 | 0.58(1) | 2.36 | 2.36 | 1.37290 | Lower |

### 2.6 Total cross sections of radiative $n^8$Li capture

The results of the present calculation of the integral total and partial cross sections are shown in Figure 2.3a. Strong sensitivity on the $C_w$ values is observed for the upper and lower sets. The input of the first ES into the total cross sections is negligible if compared with that of the GS in both cases. The dipole electric $E1$ transition from the $^4S_{3/2}$ wave to $^4P_{3/2,1/2}$ bound states provide low-energy cross sections and serves as a base for the resonant magnetic $M1$ transitions. Both resonances $^4P_{5/2}$ and $^4P_{3/2}$ are present at the energies ~230 keV and 1.32 MeV.

The comparison of the cross sections calculated in the MPCM and within the microscopic models [52, 53], along with the experimental data [12], is shown in Figure 2.3b. The red band is obtained by varying $C_w$ between 0.93 and 1.4.

The results on σ(E) obtained in [53] differ essentially in the whole energy range and reach the lower error bar limits only. Therefore, it is more reasonable to compare the MPCM and *ab initio* results obtained in [52]. The difference is observed at the

energies close to the first resonance $^4P_{5/2}$: the lower set (red dash-double-dotted curve) and *ab initio* cross sections (blue dashed curve) are comparable, contrary to the upper set application (red solid curve). Out of the resonance range $E_{c.m.} > 300$ keV and up to 1 MeV, the upper set and *ab initio* cross sections practically coincide and fit the second experimental point fairly well. The low-energy cross-section part is discussed in the following sections. The total capture cross section of thermal and cold neutrons shows the following energy dependence:

$$\sigma_{\text{ap}}(\mu\text{b}) = \frac{A}{\sqrt{E(\text{keV})}}. \tag{2.3}$$

Based on one available point, the $\sigma(E_{min})$ constant A(μb·keV$^{1/2}$) is determined, and calculation of the thermal cross section at 25.3 meV may be implemented according to Eq. 2.3. The results on $\sigma_{therm}$ obtained in the present work and recalculated with data obtained in [52, 53] are presented in Table 2.5, as well as the value obtained in [44]. In work [59] was observed $\sigma_{therm} = 41.3(1)$ mb. The accuracy of approximation (Eq. 13) is approximately 0.6% and 0.7% for the upper and lower sets, respectively.

Table 2.5 – Evaluated thermal cross sections in the $n^8$Li channel

| Reference | $E_{min}$, keV | $\sigma(E_{\text{min}})$, μb | $A$, μb·keV$^{1/2}$ | $\sigma_{therm}$, *m*b |
|---|---|---|---|---|
| Present, upper set | $10^{-5}$ | 74,485.75 | 235.54 | 46.8 |
| Present, lower set | $10^{-5}$ | 38,179.97 | 120.74 | 24.0 |
| McCracken et al. [52] | 20 | 95.125 | 425 | 85 |
| Dong et al. [53] | 8.55 | 11.58 | 33.86 | 6.7 |
| Descouvemont [44] | 25 | 38 | 190 | 37.9 |

A comparison between various $\sigma_{therm}$ values shows that the upper set results are in agreement with the data obtained in resonating group method [44]. Both these values are comparable with thermal cross sections for the neutron capture on $^6$Li and $^7$Li calculated in MPCM. In [75] reported theoretical values of $\sigma_{therm} = 39.7$ mb for $n + ^6$Li and $\sigma_{therm} = 44.2$ mb for $n + ^7$Li [60]. The results on $^6$Li and $^7$Li are in excellent agreement with experimental data [14]. Therefore, in the context of this background, the results of works [52, 53] on $\sigma_{therm}$ do not look consistent.

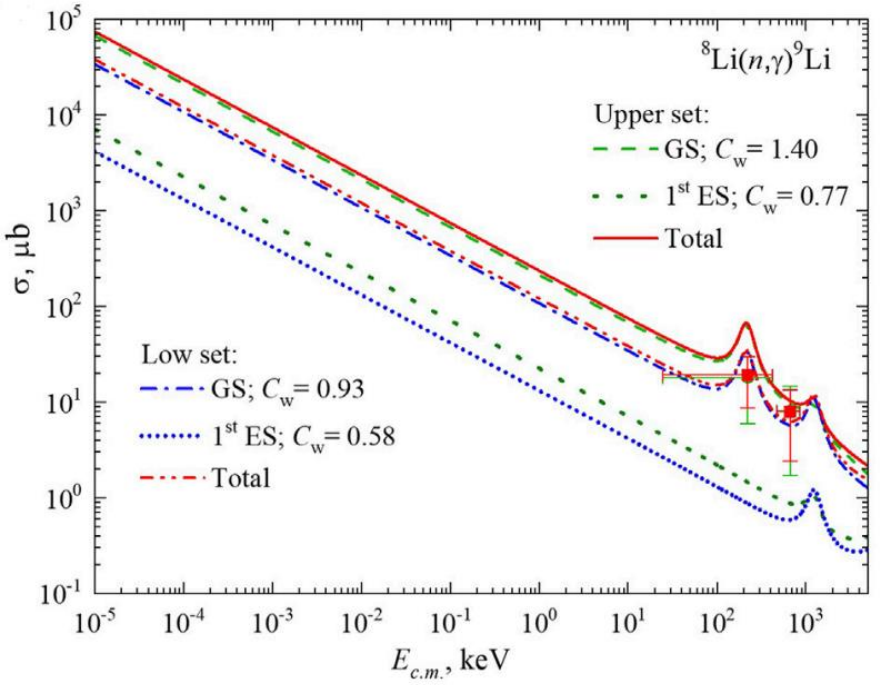


a)

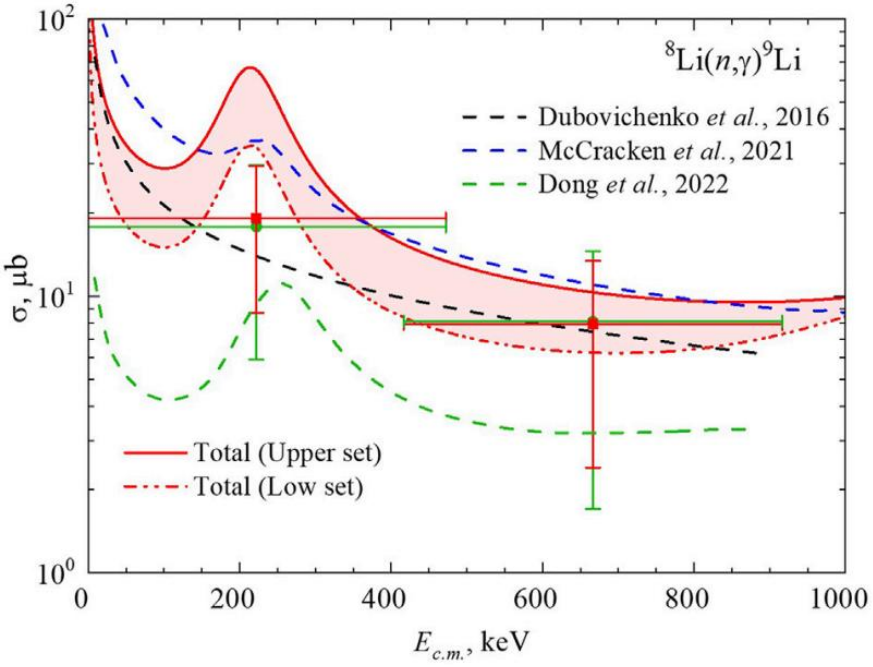


b)

Experimental data on $^9$Li Coulomb dissociation obtained in [12]: green dots on the Pb target and red squares on the U target.
a) MPCM calculations are explained in the legend.
b) Comparison of the MPCM and microscopic calculations: present MPCM total cross sections are the same as in panel (A), the blue dashed curve shows the ab initio results obtained in [52], and the green dashed curve shows the results obtained in [53] (digitalized). The black dashed curve shows the results obtained in [59].

Figure 2.3 – Total cross sections of radiative $^8$Li($n$,$\gamma$)$^9$Li capture in the GS and 1$^{st}$ ES of the $^9$Li nucleus

### 2.7 Reaction rate of radiative $n^8$Li capture

The well-known expression for the radiative neutron capture reaction rate in terms of the Maxwellian averaged cross sections is:

$$N_A\langle\sigma v\rangle = 3.7313\cdot 10^4 \mu^{-1/2} T_9^{-3/2} \int_0^\infty \sigma(E) E \exp(-11.605E/T_9) dE, \quad (2.4)$$

where $E$ is expressed in MeV, the total cross section $\sigma(E)$ is represented in μb, μ is the reduced mass in amu, and $T_9$ is the temperature in $10^9$ K [76]. Based on the total cross sections shown in Figure 2.3a, the corresponding reaction rates are presented in Figure 2.4a. The band refers to the upper and lower sets of GS and first ES interaction potentials, as shown in Table 2.4, applied to calculate total cross sections. The temperature dependence of $N_A\langle\sigma v\rangle_{\mathrm{MPCM}}$ shows near coherent behavior for the upper and lower $C_w$ sets, with a moderate plateau transforming into a noticeable increase above 0.2–0.3 $T_9$ due to the resonance at 232 keV. The second resonance at 1.3 MeV is not observed. The capture to the first excited state may be regarded as a minor correction to the GS reaction rate.

A comparison of MPCM new results and calculations obtained in [52, 53], as well as early data obtained by [59], is presented in Figure 2.4b. The *ab initio* reaction rate [52] (blue dashed curve) exceeds results at low temperatures and approximately coincides in the resonance region. A noticeable decrease in $N_A\langle\sigma v\rangle_{ab}$ initio is observed at $T_9 > 1$. The *ab initio* cross section is calculated in the energy region $E_{c.m.}$ = 20 keV–1.6 MeV so that the energy interval extension will lead a reaction rate at $T_9 > 1$. We consider the equality of the "upper set" $N_A\langle\sigma v\rangle_{\mathrm{MPCM}}$ and $N_A\langle\sigma v\rangle_{ab}$ initio at $T_9 \simeq 1$ in Figure 2.4b accidental. The great difference between reaction rates appears at $T_9 < 1$. Both model calculations MPCM and *ab initio* do not agree with the results obtained in [53] (green dashed curve in Figure 2.4b). Since 1988 [42], significant efforts have been made to find the consensus on the reaction rate value at $T_9 = 1$, useful in the context of BBN. Table 2.6 shows the comparison of different results for the reaction rates, which are partially taken from the studies in [47, 50, 53, 59]. We complemented the data on the reaction rates with the neutron number densities $n_n$, which may be referred to as the *r*-process ignition threshold density since it is calculated under the condition of equality of the $^8$Li mean lifetime and neutron capture time $\tau_\beta \approx \tau(n,\gamma)$ following the general definitions in [77]:

$$n_n = \frac{1}{\tau_\beta}\cdot\frac{1}{\langle\sigma_n, {}_y v\rangle} \quad (2.5)$$

The isotope $^8$Li is unstable with a half-life time $t_{1/2}$ = 838.79 ± 0.36 ms [11] or $\tau_\beta$ = 1.186 s.

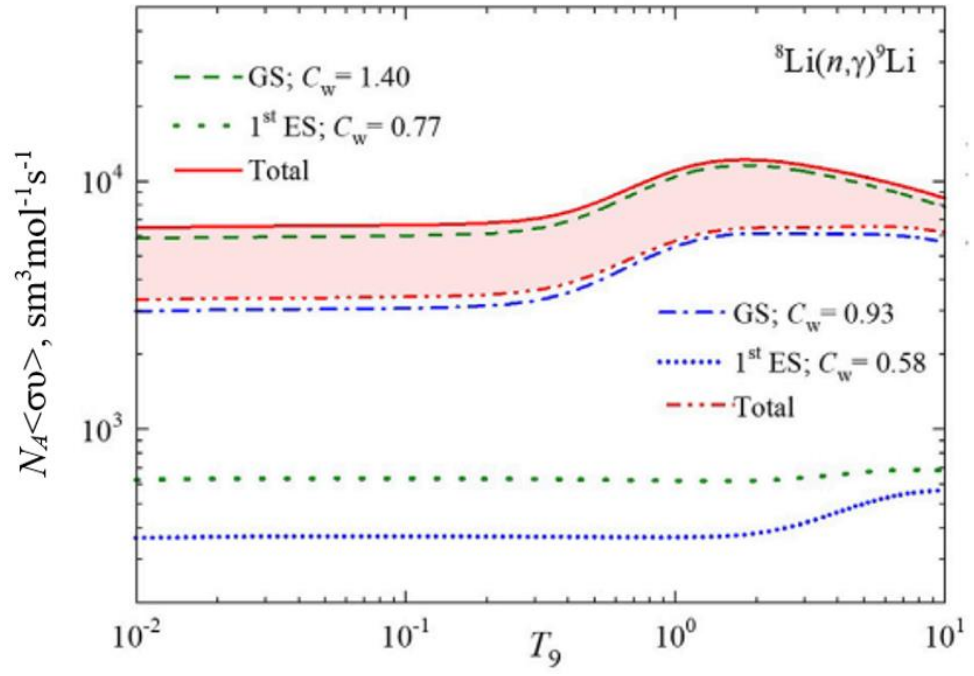


a)

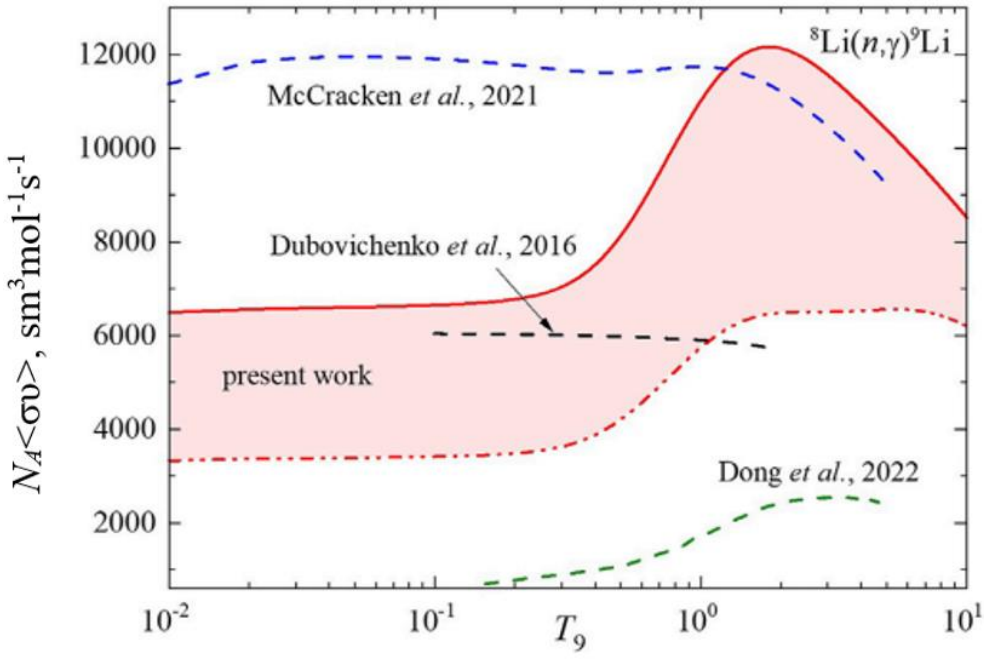


b)

a) MPCM calculations are explained in the legend.
b) Comparison of MPCM and microscopic calculations: present MPCM reaction rates are the same as in panel (A), the blue dashed curve shows the *ab initio* results obtained in [52], and the green dashed curve shows the results obtained in [53] (digitalized). The black dashed curve shows the results from [59].

Figure 2.4 – Reaction rate of radiative $^8$Li($n$,$\gamma$)$^9$Li capture to the GS and 1$^{st}$ ES of $^9$Li

The estimated neutron number densities $n_n$ given in Table 2.4 condition the start of the *r*-process on $^{8}$Li at $T_9 = 1$ and lay in the interval $1.2 \cdot 10^{19}$- $6.3 \cdot 10^{20}$ cm$^{-3}$, which brings forth a difference of up to the factor 50 with respect to the listed datasets.

Following the study in [78], the typical conditions for the *r*-process $n_n = 3 \cdot 10^{23}$ cm$^{-3}$ and $T_9 \sim 1$ require both an explosive environment and high-density neutron-rich matter. In this context, the difference in the reaction rate data given in Table 2.4 seems not so crucial.

Table 2.6 – Comparison of reaction rates for the direct capture of the $^{8}$Li($n,\gamma$)$^{9}$Li reaction at $T_9 = 1$

| References | Reaction rate |
|---|---|
| Experiment | |
| Zecher *et al.*, 1998 [12] | <7200 |
| Kobayashi *et al.*, 2003 [47] | <790 |
| Li *et al.*, 2005 [48] | 4000 |
| Guimaraes *et al.*, 2007 [49] | 3270 |
| Gupta *et al.*, 2022 [41] | <790 |
| Theory | |
| Malaney & Fowler, 1988 [42] | 43000 |
| Mao and Champagne, 1991 [40] | 21000 |
| Thieleman *et al.*, 1991 [43] | 3350 |
| Descouvemont, 1993 [44] | 5300 |
| Rauscher *et al.*, 1994 [45] | 4500 |
| Bertulani, 1999 [46] | 2200 |
| Banerjee *et al.*, 2008 [50] | 2900 |
| Ma *et al.*, 2012 [51] | <4300 |
| Dubovichenko, 2016 [59] | 5900 |
| McCracken *et al.*, 2021 [52] | 11770 |
| Dong *et al.*, 2022 [53] | 1479 |
| *Present, 2023* | ***Up**: 11000; **Low** : 5740* |
| | ***Adopted** : 8370* |

We still see a challenge in finding any cross-points that allow us to resolve the problem of variable $^{8}$Li($n,\gamma$)$^{9}$Li reaction rates. Another one is based on the experience of studying the radiative capture reaction rates on the group of the neighboring isotopes. For example, it was found that low-temperature reaction rates for $^{10-13}$B($n,\gamma$)$^{11-14}$B conditioned by the *S*-wave capture outside of the resonance energy region show some regularity - the higher the channel threshold, the higher the reaction rate [22]. The same effect is observed for the proton capture on the nitrogen isotopes $^{12,13,15}$N($p,\gamma$)$^{13,14,16}$O [79], and an exception is given by the reaction $^{14}$N($p,\gamma$)$^{15}$O as *S*-wave capture occurs via a weak *E*2 transition contrary to more advanced *E*1 or *M*1.

Figure 2.5 shows the reactions rates on lithium isotopes $^{6,7,8}$Li calculated in the MPCM. We observe that the order of magnitude of $N_A\langle\sigma v\rangle$ below ~ 0.2 $T_9$ fits the threshold energy relation $E_{th}(n^6\text{Li}) > E_{th}(n^8\text{Li}) > E_{th}(n^7\text{Li})$ if, for the reaction $^8\text{Li}(n,\gamma_{0+1})^9\text{Li}$, we take the upper set results.

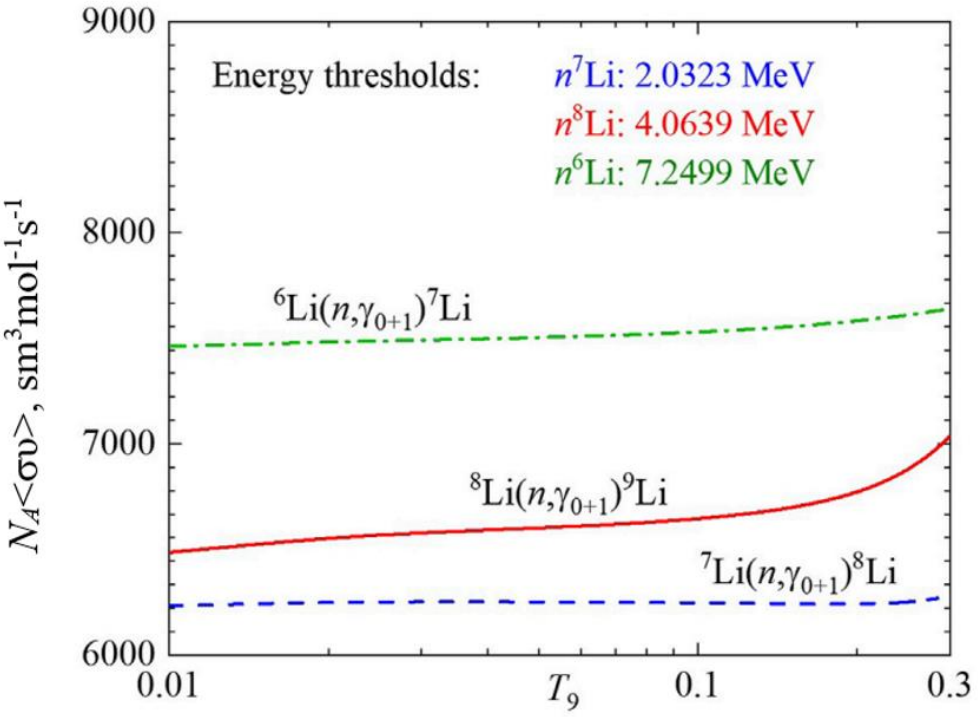


Figure 2.5 – The reaction rates of radiative neutron capture for $^6\text{Li}(n,\gamma_{0+1})^7\text{Li}$ [75], $^7\text{Li}(n,\gamma_{0+1})^8\text{Li}$ [60], and $^8\text{Li}(n,\gamma_{0+1})^9\text{Li}$ present results for the upper set in Figure 2.4

The reaction rates corresponding to the MPCM lower set, as well as ab initio calculations in [52], and data obtained in [53] do not fit the aforementioned regularity. It must be underlined that the reactions $^6\text{Li}(n,\gamma_{0+1})^7\text{Li}$ [75] and $^7\text{Li}(n,\gamma_{0+1})^8\text{Li}$ [60] are examined much better as they directly concern the well-known lithium problem [80].

### 2.8 Concluding remarks

Following results on the $^7\text{Li}(n,\gamma_{0+1})^8\text{Li}$ reaction [60], we reconsider the reaction $^8\text{Li}(n,\gamma_{0+1})^9\text{Li}$. The total cross sections and reaction rates are calculated for the reaction $^8\text{Li}(n,\gamma_{0+1})^9\text{Li}$, including the corrections inserted for the interaction potentials comparing the early work [59].

The experimentally proved resonance at $E_{c.m.} = 0.232$ MeV in the $^4P_{5/2}$ wave and ab initio-predicted $^4P_{3/2}$ resonance at 1.32 MeV [52] are considered. The intensity of $^4P_{5/2}$ resonance depends strongly on the range of asymptotic constants $C_w$, as well as the cross sections as a whole, which is observed in the temperature $T_9$ dependence of the reaction rates.

The minor role of the $(n,\gamma_1)$ process is proved; therefore, the GS transitions are dominant. The variation in the GS asymptotic constant $C_w$ = 0.93–1.40 leads to the values of the reaction rate 5,740-11,000 cm$^3\cdot$mol$^{-1}\cdot$s$^{-1}$ at temperature $T_9$ = 1 relevant

for the r-formation of $^{9}$Li. The upper value nearly coincides with the *ab initio* reaction rate 11,770 $cm^3 \cdot mol^{-1} \cdot s^{-1}$ at $T_9$ = 1 [52], but we acknowledge this agreement as occasional.

We suggest two criteria to narrow down the range of reaction rates in study. The first one concerns the values of thermal cross sections. Analysis of $\sigma_{therm}$ values leads us to conclude that the upper set calculations yielding 46.8 mb ($C_w$ = 1.40) are more relevant as they conform to estimations carried out in [44] and data on the $^{6}$Li and $^{7}$Li isotopes [14].

The second criterion is related to the reaction rates of radiative neutron capture on lithium isotopes $^{6,7,8}$Li. The examined correlation between the energy thresholds and order of reaction rates at low temperatures beyond the possible resonances $T_9 < 0.2$ leads to the conclusion that upper-set calculations are more reasonable (see Figure 2.5).

The recent results on the reaction rates obtained in [52, 53] show substantial differences, both qualitative and quantitative. The present calculations do not eliminate this discrepancy. The new measurements proposed in [41] may clarify the situation.

## 3 THE RADIATIVE NEUTRON $^{9}$Be($n,\gamma_{0+1+2+3+4+5}$)$^{10}$Be CAPTURE

### 3.1 The role of $^{9}$Be($n,\gamma_{0+1+2+3+4+5}$)$^{10}$Be reaction in the Lithium-Beryllium-Boron-Carbon (Li-Be-B-C) chain

Synthesis of $^{9}$Be means overcoming the well-known gap with $A = 8$. Therefore, the $^{9}$Be as the *seed nucleus* may be incorporated in branching chains leading to the carbon isotopes production. More than 30 years have passed since Malaney & Fowler raised the discussion on the $^{9}$Be production and suggested additions to the standard nuclear reaction network for developing the inhomogeneous model of BBN [81]. While discussing the role of the radioactive isotopes in the formation of stable elements at the early stage of the Universe's evolution, the set of chains has been proposed (see the network in Figure 1 in [82]). Later, two chains essential for the production of neutron-rich isotopes were suggested in [3]:

$$\ldots{}^{4}\mathrm{He}(^{3}\mathrm{H},\gamma)^{7}\mathrm{Li}(n,\gamma)^{8}\mathrm{Li}(\alpha,n)^{11}\mathrm{B}(n,\gamma)^{12}\mathrm{B}(e^{-}\nu)^{12}\mathrm{C}(n,\gamma)^{13}\mathrm{C}(n,\gamma)^{14}\mathrm{C}(n,\gamma)^{15}\mathrm{C}(e^{-}\nu)^{15}\mathrm{N}\ldots, \quad (3.1)$$

$$\ldots{}^{7}\mathrm{Li}(n,\gamma)^{8}\mathrm{Li}(\mathrm{n},\gamma)^{9}\mathrm{Li}(e^{-}\nu)\underline{^{9}\mathrm{Be}(n,\gamma)^{10}\mathrm{Be}}(e^{-}\nu)^{10}\mathrm{B}(n,\gamma)^{11}\mathrm{B}(n,\gamma)^{12}\mathrm{B}(e^{-}\nu)^{12}\mathrm{C}\ldots. \quad (3.2)$$

Path (3.1) is the Lithium-Boron-Carbon (Li-B-C) chain, and (3.2) is the Lithium-Beryllium-Boron-Carbon (Li-Be-B-C) chain. Reaction $^{9}$Be($n,\gamma$)$^{10}$Be in (3.2) plays the role of trigger for ignition of the B-C path. That is reasonable as $^{10}$Be is the long-lived isotope ($1.387\times10^{6}$ years) and, therefore, may play the role of seed nucleus. One may find the balance between the (3.1) and (3.2) scenarios while all corresponding reaction rates are well-defined.

One more concern to $^{9}$Be($n,\gamma$)$^{10}$Be process: Terasawa and coworkers raised the discussion on the critical reaction flows leading to the production of carbon isotopes (Figure 6 in [6]). It was pointed out in [6] that the switch off the $^{10}$Be($\alpha,\gamma$)$^{14}$C reaction in the Be-isotope chain is leading to the ignition of Li-Be-C reaction flow:

$$\ldots{}^{7}\mathrm{Li}(n,\gamma)^{8}\mathrm{Li}(n,\gamma)^{9}\mathrm{Li}(e^{-}\nu)\underline{^{9}\mathrm{Be}(n,\gamma)^{10}\mathrm{Be}}(n,\gamma)^{11}\mathrm{Be}(n,\gamma)^{12}\mathrm{Be}(e^{-}\nu)^{12}\mathrm{B}(e^{-}\nu)^{12}\mathrm{C}\ldots. \quad (3.3)$$

We will pay special attention to the $^{9}$Be($n,\gamma$)$^{10}$Be reaction in the beryllium paths (3.2) and (3.3). The motivation concerns the disputing point of view on the origin of $^{10}$Be: the current position is that $^{10}$Be *cannot be produced by thermonuclear reactions* in stars [83] but is processed via cosmic-ray spallation [84].

Meanwhile, the rate of $^{9}$Be($n,\gamma$)$^{10}$Be reaction is included in the network for calculation of the abundance of the beryllium isotopes in the context of BB nucleosynthesis up to CNO [5, 85].

The role of the $^{9}$Be($n,\gamma$)$^{10}$Be reaction in chains (3.2) and (3.3) is still unclear today. The reason is that only one modeless result on the reaction rate published by Rauscher in 1994 was included in the network calculations [45]. Nowadays, there are two more reports on the reaction rate based on the model calculations [16, 86]. Below we show that these results do not confirm those in [16]. The present paper, along with [16, 86], is aimed to attract attention to the $^{9}$Be($n,\gamma$)$^{10}$Be reaction and reconsider its astrophysical status in elements evolution according to (3.2) and (3.3) branching.

We propose the practical goal to reproduce the cross-sections of nucleon-induced radiative capture reactions on the 1p-shell nuclei ($A \leq 16$) within the same model approach, ad hoc MPCM, and finally to calculate the corresponding reaction rates [26, 27]. The idea is to complete the sequences like (3.1). Recently we presented the calculations on the reactions $^{7}$Li$(n,\gamma)^{8}$Li [87], $^{10}$B$(n,\gamma)^{11}$B [78], $^{11}$B$(n,\gamma_0)^{12}$B [88], and $^{11}$B$(n,\gamma_{0+1+2+3+4})^{12}$B [89].

Preliminary research of $^{9}$Be$(n,\gamma)^{10}$Be reaction which was done nearly ten years ago [90] and recognized it as an estimative one for the following reasons:

(a) The cross-sections for the capture to the ground state and four excited states (ESs) have been calculated in the energy range from 10 meV (1 meV = $10^{-3}$ eV) up to 1 MeV. Only two experimental points at 25 meV [91] and 25 keV [92, 93] were available as benchmarks.

(b) Only one $^{3}D_3$ resonance at 622 keV in l.s. was considered in [90]. Extension of the energy interval from 1 MeV to 5 MeV allows the inclusion of four more resonances in the present consideration. Their effect on the cross-sections and the reaction rates is demonstrated.

(c) The calculation procedure of the overlapping integrals is re-examined compared to [90] (see for details Section 6).

(d) The reaction rate is not calculated in [90].

In the present work within the MPCM, we consider the $^{9}$Be$(n,\gamma_{0+1+2+3+4+5})^{10}$Be reaction in the region of thermal and astrophysical energies of 10 meV up to 5 MeV, considering the formation of $^{10}$Be both in the GS and five ESs below $n^{9}$Be threshold, as well as five low laying resonances. Present research of $^{9}$Be$(n,\gamma)^{10}$Be also covers new experimental data on the thermal neutron capture cross-section [75, 94]. Theoretical calculations are now relevant, while the experimental study of the $^{9}$Be$(n,\gamma)^{10}$Be reaction is insufficient. Recent measurements of the total cross-section σ for this reaction added two points [86]; therefore, 6 points are available now above 1 MeV [90, 92, 93].

We also compare the MPCM reaction rate with the modelles calculations [45] and direct radiative capture model results [16, 86].

### 3.2 Classification of orbital states for the $n^{9}$Be system

Consider the classification of orbital states of clusters based on Young's diagrams for the $^{9}$Be nucleus. Assuming that this system consists of 8 + 1 particles, we can use diagrams {44} and {1} for them. In this case, for $^{9}$Be, we obtain two possible orbital symmetries {54} + {441}. The first is forbidden since it contains five cells in one row, and the second belongs to the allowed one. The diagram {441} corresponds to the ASs in the $n^{8}$Be system.

Therefore, for the $n^{9}$Be system, we have: {441} + {1} = {541} + {442} + {4411}. This set contains FS with the diagram {541} for the orbital angular momentums $L$ = 1, 2, 3,… and AS with configuration {4411} and $L$ = 1, 3. Orbital angular momentums $L$ are determined by Elliott's rule [95, 96]. Diagram {442} is apparently allowed one with $L$ = 0, 2,… and is relevant to allowed BSs in $S$ and $D$ waves. We limited to the minimum values of the orbital angular momentum $L$ = 0, 1, 2.

The quantum numbers of $^9$Be are $J^\pi, T = 3/2^-$, and for $^{10}$Be, they are $J^\pi, T = 0^+, 1$ [97, 98]. The $n^9$Be potential refers to the $^3P_0$ wave corresponding to the Young's diagrams {541} and {4411}. The first diagram is forbidden, and the second one is allowed. The diagram {4411} matches the GS of the $^{10}$Be nucleus in the $n^9$Be channel. The other $^3P_J$ waves correspond to the allowed bound excited states. Similar potentials are used for the continuous partial waves.

We assume that there is a bound AS for the {442} diagram in the $^3S$ wave without FS. It may correspond to the third excited state (3$^{rd}$ ES) with $J^\pi = 1^-$ and excitation energy of 5.9599 MeV.

In the $^3D$ wave containing a bound FS for the {541} diagram, there is also a bound AS for {442}. It may correspond to the fifth excited state (5$^{th}$ ES). The same classification is done for all other partial waves. Therefore, we unambiguously fix the structure of the forbidden and allowed states in each partial potential for $L$ = 0, 1, 2. Note that the number of BSs, forbidden or allowed in any partial potential, determines the number of WF nodes at short distances [25]. Recall the radial bound state function corresponding to the minimum energy has no node, and the next in energy BS has one node, etc. [24].

### 3.3 Interaction potentials for the $n^9$Be system

The Figure 3.1 illustrates the spectrum of the $^{10}$Be nucleus and guides further calculations. It shows six bound states, *ad hoc* one ground, and five excited states. Five resonances above threshold $E_b$ = 6.8122 MeV are included in the consideration.

Let us comment briefly information on Figure 3.1. Note, experimental data of the $^{10}$Be level are well defined today. The corresponding compilation on the excitation energies $E_x$, total angular momentums and parity $J^\pi$, as well as the total widths of exited states $\Gamma$ [97, 98].

Following the algebraic expression for the reduced matrix elements (1.3) the selection rules are coming for the electric multipole transitions $EJ$ of J multipolarity:

$$\mathbf{L_i} + \mathbf{J} = \mathbf{L_f}, \ \mathbf{L_i} + \mathbf{S} = \mathbf{J_i}, \ \mathbf{L_f} + \mathbf{S} = \mathbf{J_f}, \ \mathbf{J_i} + \mathbf{J} = \mathbf{J_f}, \tag{3.4}$$

where notations are explained in Section 1.2. Based on relations (3.4) the allowed transition channels from the initial resonance states to the final bound states of $^{10}$Be $[^{2S+!}L_J]_i \xrightarrow{NJ} [^{2S+!}L_J]_f$ are pointed in central and right columns.

As it is seen in Figure 3.1 the ground and 4$^{th}$ excited states are $J^\pi = 0^+$ ones, therefore they are provided by the same $E2$ transition. The analoguous situation is observed for the 1$^{st}$ and 2$^{nd}$ excited states $J^\pi = 2^+$, but intial channel is formed due to all five resonance states. Transitions to the 3$^{rd}$ and 5$^{th}$ excited states are not allowed via resonance states in continuum. In subsections 3.3.1 and 3.3.2 the detailed procedure of construction the corresponding interaction potential for the bound and excited states is presented.

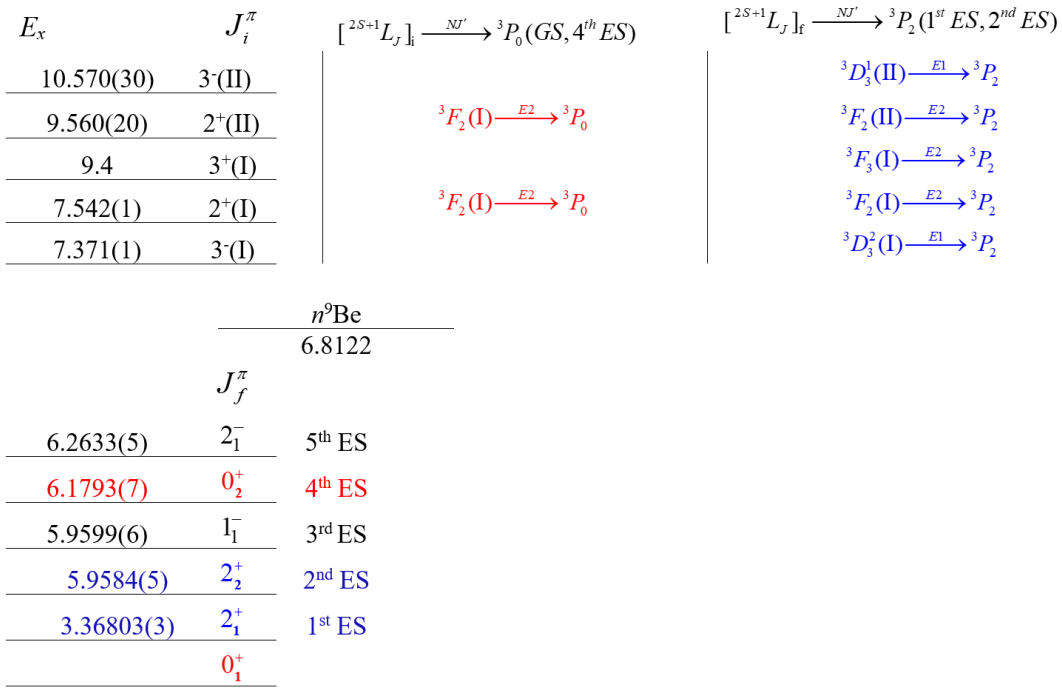


$J_{\mathbf{N}}^\pi$ – low index **N =1** or **2** indicates the order of appearing the state with the same momentum $J$ in the spectrum of $^9$Be. In the case of the continuum spectrum, the corresponding indication is given as Roman numbers.

Figure 3.1 – Spectrum levels in MeV (c.m.) of the $^{10}$Be nucleus with the indication of quantum numbers $J^\pi$, $T$ [97, 98] (arbitrary energy scale)

### 3.4 Bound states interaction potentials

The bound state parameters $V_0$ and $\gamma$ are found unambiguously by matching the binding energy, charge radius, and AC. While the binding energy and charge radius can be calculated with high accuracy, the most significant uncertainties are caused by the AC. Let us start with the definition of AC. The dimensionless constant $C_w$ is found from the following relation:

$$\chi_L(r) = \sqrt{2k_0} C_w W_{-\eta L+1/2}(2k_0 r). \tag{3.5}$$

Here, $W_{-\eta L+1/2}$ is Whittaker function, $k_0$ is a wave number related to the binding energy $E_b = k_0^2 / 2\mu$. In case $\eta = 0$, the analytical form of the Whittaker function is:

$$W_{0,l}(z) = e^{-z/2} \sum_{n=0}^{l} z^{-n} \frac{(l+n)!}{(l-n)!n!}. \tag{3.6}$$

Let us present all variants for ACs, which include asymptotic normalization coefficient (ANC), dimensionless asymptotic constant $C_w$, and spectroscopic factor $S_F$.

The dimensional asymptotic constant $C$ (in fm$^{-1/2}$) is related to $A_{NC}$ via the spectroscopic factor $S_F$:

$$A_{NC} = S_F \times C^2. \tag{3.7}$$

Along with relation (3.5), the asymptotics of WF may be written via the dimensional constant $C$:

$$\chi_L(r) = CW_{-\eta L+1/2}(2k_0 r). \tag{3.8}$$

Comparison of relations (3.5) and (3.8) shows the following interrelation of the asymptotic constants:

$$C = \sqrt{2k_0} C_w. \tag{3.9}$$

The available information on the spectroscopic factors $S_F$ and ACs $A_{NC}^2$ for the GS of $^{10}$Be is given in Table 3.1 [16, 66, 99-106]. The relation $C_w^2 = A_{NC}^2 / (S_F 2k_0)$ is used for the calculation of values $C_w$.

The data on the spectroscopic factors $S_F$ for the virtual decay of $^{10}$Be$^*$ in ESs are presented in Table 3.2: experimental values are from [99, 100, 107, 108] and the calculated ones from the [16, 66, 101-106, 109]

Table 3.1 – Data on the spectroscopic factors $S_F$ and calculated constants $C_w$. for the GS of $^{10}$Be ($J_N^\pi = 0_1^+$) corresponding the $A_{NC}$=9.12 fm$^{-1}$ [66]

| Reference | $S_F$ | $C_w$ |
|---|---|---|
| Experiment | | |
| Bockelman *et al.*, 1951 [99], Variational method | 2.357 | 2.231 |
| Darden *et al.*, 1976 [107], DWBA | 2.1 | 2.07 |
| Harakeh *et al.*, 1980 [108], DWBA | 1.58 | 1.81 |
| Lukyanov *et al.*, 2014 [100], Optical model | 1.65 | 1.85 |
| *Average, present calculations* | $\overline{S_F} = 1.922$ | $\overline{C_w} = 1.990$ |
| Theory | | |
| Schmidt-Rohr *et al.*, 1964 [101], Born Approximation | 1.67 | 1.89 |
| Cohen & Kurath, 1967 [102], 1p shell model | 2.3565 | 2.231 |
| Anderson *et al.*, 1974 [103], DWBA | 1.21 | 1.54 |
| Mughabghab, 1985 [104], Spin-spin interaction | 2.1 | 2.07 |
| Ogawa *et al.*, 2000 [105], Stochastic variational method | 2.24 | 2.14 |
| Lee *et al.*, 2007 [106], Shell model | 2.44 | 2.30 |

Continue of Table 3.1

| | | |
|---|---|---|
| Grinyer *et al.*, 2011 [109], *ab initio* | 2.36 | 2.23 |
| Grinyer *et al.*, 2011 [109], Variational Monte Carlo | 1.93 | 2.01 |
| Timofeyuk, 2013 [66], 0-*p* shell model | 1.515 | 1.77 |
| Mohr, 2019 [16], Direct capture model | ~1.06 | 1.36 |
| Mohr, 2019 [16], Direct capture model | 1.58 | 1.81 |
| *Average, present calculations* | $\overline{S_F} = 1.923$ | $\overline{C_w} = 1.980$ |

Table 3.2 – Data on the spectroscopic factors $S_F$ for the ESs of $^{10}$Be$^*$

| Reference | 1st ES, $2_1^+$ | 2nd ES, $2_2^+$ | 3rd ES, $1_1^-$ | 4th ES, $0_1^+$ | 5th ES, $2_1^-$ |
|---|---|---|---|---|---|
| Experiment | | | | | |
| Bockelman *et al.*, 1951 [99], Variational method | 0.274 | 0.421 | – | – | – |
| Darden *et al.*, 1976 [107], DWBA | 0.23 | ≤1.0 | – | – | 0.065 |
| Harakeh *et al.*, 1980 [108], DWBA | 0.38 | ≤0.73 | ≤0.14 | – | 0.08 |
| Lukyanov *et al.*, 2014 [100], Optical model | 1.00 | 1.40 | 0.43 | – | 0.26 |
| ***Average*** | **0.471** | **0.888** | **0.285** | **–** | **0.135** |
| Theory | | | | | |
| Schmidt-Rohr *et al.*, 1964 [101], Born Approximation | 0.24 | – | – | – | – |
| Cohen & Kurath, 1967 [102], Shell model | 0.1261 | 0.1899 | – | – | – |
| Anderson *et al.*, 1974 [103], DWBA | 0.17 | 0.54 | 0.36 | – | 0.20 |
| Mughabghab, 1985 [104], Spin interaction | 0.23 | – | – | 0.031 | – |
| Ogawa *et al.*, 2000 [105], Variational method | 0.23 | 0.40 | 0.79 | 0.10 | – |
| Mohr, 2019 [16], Direct capture model | 0.38 | <0.73 | <0.14 | – | 0.08 |
| Mohr 2019 [16], Direct capture model | 0.17 | 0.54 | – | – | – |
| ***Average*** | **0.2209** | **0.4800** | **0.43** | **0.0655** | **0.14** |

The calculated results on the binding energy $E_b$, charge $R_{ch}$, and matter radii $R_m$ within the MPCM are presented in Table 3.3.

Table 3.3 – Potential parameters of the bound GS and ESs of the $^{10}$Be nucleus in the $n^9$Be channel. The excitation energies $E_x$ are taken from [97, 98]. Binding energy $E_b$, charge $R_{ch}$, and matter radii $R_m$ in fm and constant $C_w$ are calculated using potentials with parameters $V_0$ and $\gamma = 0.4$ fm

| No | $E_x$, MeV | $J^\pi$ | $\left[{}^{2S+1}L_J\right]_f$ | $V_0$, MeV | $E_b$, MeV | $R_{ch}$ | $R_m$, | $C_w$ |
|---|---|---|---|---|---|---|---|---|
| 1 | 0 | $0_1^+$ | ${}^3P_0^1$ | 363.351572 | -6.81220 | 2.53 | 2.54 | 1.72(1) |
| 2 | 3.36803(3) | $2_1^+$ | ${}^3P_2^1$ | 345.676475 | -3.44417 | 2.54 | 2.57 | 1.14(1) |
| 3 | 5.9584(5) | $2_2^+$ | ${}^3P_2^2$ | 328.584340 | -0.85380 | 2.55 | 2.69 | 0.60(1) |
| 4 | 5.9599(6) | $1_1^-$ | ${}^3S_1$ | 33.768513 | -0.85230 | 2.56 | 2.76 | 1.24(1) |
| 5 | 6.1793(7) | $0_2^+$ | ${}^3P_0^2$ | 326.799005 | -0.63290 | 2.56 | 2.72 | 0.53(1) |
| 6 | 6.2633(50) | $2_1^-$ | ${}^3D_2$ | 248.148914 | -0.54890 | 2.53 | 2.52 | 0.057(1) |

For the potential of the GS binding energy, the value 6.812200 MeV is obtained with an accuracy of $10^{-6}$ MeV, a mean square charge radius equals 2.53 fm, and a matter radius is 2.54 fm. The AC error is determined by averaging over the interval 4 16 fm, where the AC remains practically stable.

The potential of the first excited state (1st ES) ${}^3P_2^1$ at an excitation energy of 3.36803(3) MeV $^{10}$Be [-3.44417] is obtained with $J^\pi = 2^+$. Here and further in brackets energy relative to the threshold $n^9$Be is pointed in MeV. Such potential has one bound FS at {541}. Since data on the AC of this and other ESs are absent, the parameter γ is the same as for the GS potential.

For the potential of the second excited state (2nd ES) ${}^3P_2^2$ at an excitation energy of 5.9584(5) MeV $^{10}$Be [-0.85381] with $J^\pi = 2^+$ is obtained. It also has one FS.

At excitation energy of 5.9599(6) MeV [-0.8523], the third excited state (3rd ES) with quantum numbers $J^\pi = 1^-$ is reported in [97]. Such an excited state considered as bound AS in the ${}^3S_1$ wave related to {422} Young's diagram.

The fourth excited state (4th ES) at an energy of 6.1793(7) MeV [-0.6329] coincides in its quantum numbers $J^\pi, T = 0^+, 1$. with the GS [97].

The fifth excited state (5th ES) at an energy of 6.2633(50) MeV relative to the GS [-0.54890] with quantum numbers $2_1^-$ refers to the ${}^3D_2$ state [97]. The 5th ES was not considered earlier, and here we estimate the value of its contribution to the total $n^9$Be capture cross-sections.

While calculating the charge and matter radii of $^{10}$Be the $^9$Be nucleus radius equal to the 2.518(12) fm from [110] was used. The neutron charge radius equals zero, and its matter radius is the same as the proton radius 0.8775(51) fm given in the database [111]. To demonstrate the quality of present calculations of the $R_{ch}$ charge and $R_m$ matter radii, the suggestion compiling the experimental data on these values and available model calculations in Table 3.4.

Table 3.4 – Data on the $R_{ch}$ charge and $R_m$ matter radii

| Reference | States | $R_m$, fm | $R_{ch}$, fm |
|---|---|---|---|
| Experiment | | | |
| Ozawa *et al.* 2001 [112], Glauber Model | | $2.30 \pm 0.02$ | $2.30 \pm 0.02$ |
| Nörtershäuser *et al.* 2009 [113], Isotopic shift | GS, $0_1^+$ | 2.357(18) | 2.357(18) |
| Descouvemont & Itagaki 2020 [114], Stochastic variational method | | $2.44 \pm 0.02$ | $2.44 \pm 0.02$ |
| *Average values* | | $2.3657 \pm 0.02$ | $2.3657 \pm 0.02$ |
| Theory | | | |
| Liatard *et al*. 1990 [115], Microscopic model | | $2.479 \pm 0.028$ | – |
| Ogawa *et al.* 2000 [105], Stochastic variational method | | 2.28 | 2.35 |
| Wang *et al.* 2001 [116], Relativistic Mean Field | GS, $0_1^+$ | 2.40 | – |
| Timofeyuk, 2013 [66], 0-p shell model | | – | 3.042 |
| Ahmad *et al.* 2017 [117], Glauber Model | | $2.36 \pm 0.04$ | – |
| *Average values* | | $2.3798 \pm 0.034$ | 2.696 |
| Ogawa *et al.* 2000 [105], Stochastic variational method | 1st ES, $2_1^+$ | 2.41 | 3.47 |

The summary on the spectroscopic factor $S_F$ and $C_w$ for the GS of $^{10}$Be shows very close average values for the experimental ($\bar{S}_F^{exp.} = 1.922$, $\bar{C}_w^{exp.} = 1.99$) and theoretical ($\bar{S}_F^{theor.} = 1.923$, $\bar{C}_w^{theor.} = 1.98$) ones. At the same time, the corresponding intervals differ. In the case of experiment, one has: $1.58 \le \bar{S}_F^{exp.} \le 2.357$ and $1.85 \le \bar{C}_w^{exp.} \le 2.23$, and theoretical intervals are $1.06 \le \bar{S}_F^{theor.} \le 2.62$ and $1.36 \le \bar{C}_w^{theor.} \le 2.41$. The value for the asymptotic constant $C_w$ for the GS of $^9$Be obtained in present calculations equals 1.72(1), which is within the pointed intervals.

There are no data on the ANC for the excited states of $^{10}$Be. The obtained $C_w$ in Table 3.3 may be assumed as the proposed ones for the 1st – 5th ESs. Based on the interaction potentials with parameters from Table 3.3, the radial wave functions of the BSs have been calculated as the numerical solutions of the radial Schrödinger equation. The description of the developed algorithm one may find in [33, 118].

BS radial WFs are shown in Figure 3.2. Their node or nodeless behavior is the signature of the Young's diagrams classification relative to the number of ASs and FSs in a given partial wave. These functions are the constituents of the overlapping integrals (3.5) and (3.8).

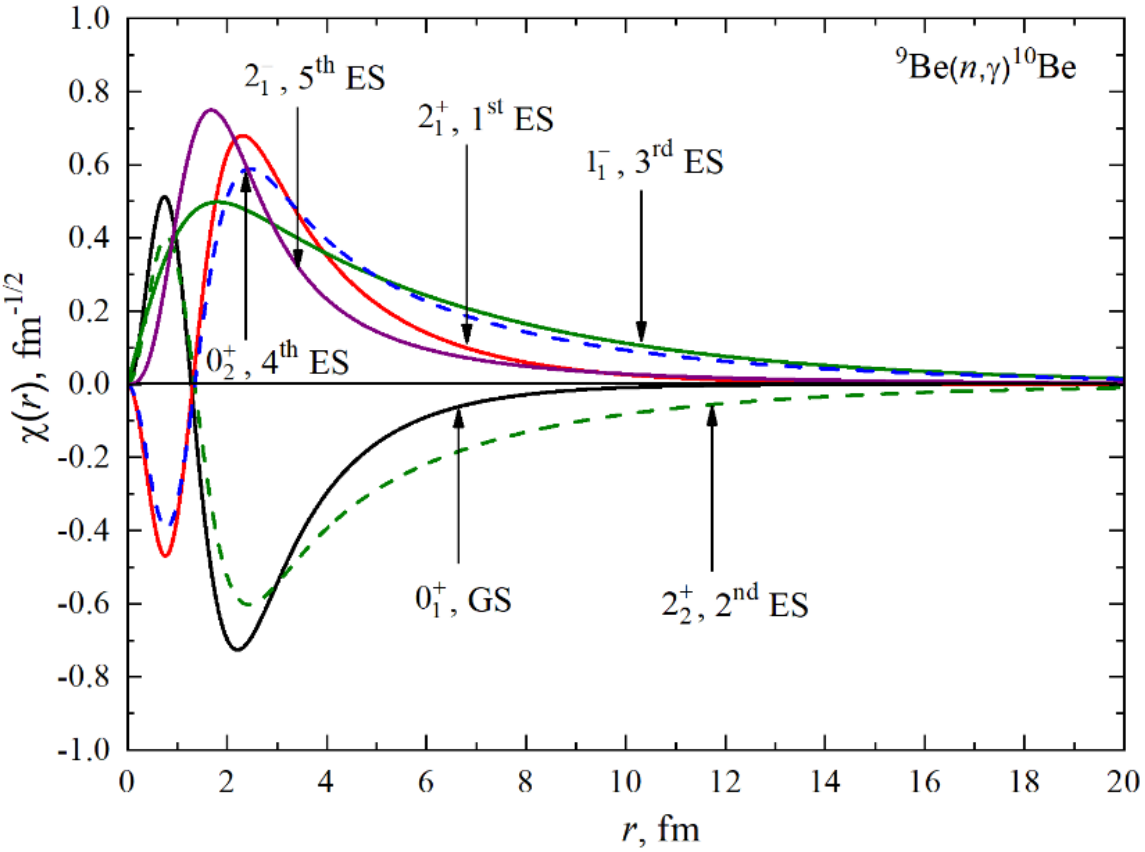


Figure 3.2 – Radial wave functions of the bound states in the $n^9$Be channel calculated with the potentials from Table 3.3

### 3.5 Scattering states interaction potentials

Following Figure 3.1, we consider five resonance states of $n^9$Be at energies less than 5.0 MeV. We use the characteristics of the energy levels to construct the scattering potentials: fitting the excitation energy $E_x$ and level width $\Gamma_{c.m.}$, the parameters $V_0$ , and γ are determined. The results for the matched parameters of the scattering potentials are given in Table 3.5. The calculated values of the $E_{\text{res}}$ and $\Gamma_{c.m}$ are in good agreement with the experimental data [97, 98].

Let us comment on Table 3.5 and its illustration in Figure 3.3. In the spectrum of the $^{10}$Be nucleus in the $n^9$Be channel, there is an above-threshold $J^\pi = 3^-$ level at the energy of 0.622(1) MeV in l.s. or 0.559(1) keV in c.m. and width of $\Gamma_{c.m.} = 15.7$ keV [97]. We compare it to the resonance $^3D_3^1$ in the elastic $n^9$Be scattering channel.

For the potential of the resonance $^3D_3^1$ scattering wave at 559(1), keV corresponding parameters are the same as in [90]. The elastic scattering phase shift for this potential is shown in Figure 3.3 by a solid red curve and has a resonance character, reaching 90(1)° at 559(1) keV. The potential contains the bound FS related to the diagram {541} following the above classification, and the state for {422} is considered unbound. The width of such a resonance is equal to 15(1) keV, which is in good agreement with the results of [97].

Table 3.5 – Parameters of the potentials of the resonant and nonresonant scattering states in the $n^9$Be channel. The excitation energy of $E_x$ (MeV) levels and their width $\Gamma_{c.m.}$ (keV) are taken from experimental data [97, 98]. Resonance energies $E_{res}$ (MeV) and widths $\Gamma_{c.m.}$ (keV) are calculated with the parameters $V_0$ and $\gamma$

| No. | $E_x$, *expt.* | $\Gamma_{c.m.}$, *expt.* | $J^\pi$ | $^{2S+1}L_J$ | $V_0$, MeV | γ, fm$^{-2}$ | $E_{res}$, *theor.* | $\Gamma_{c.m.}$, *theor.* |
|---|---|---|---|---|---|---|---|---|
| 1 | **7.371(1)** | **15.7(5)** | **3$^-$** | $^3D_3^1$ | **457.879** | **0.35** | **0.559(1)** | **15(1)** |
| 2 | **7.542(1)** | **6.3(8)** | **2$^+$(I)** | $^3F_2^1$ | **211.667** | **0.11** | **0.730(1)** | **6(1)** |
| 3 | 9.4 | 291(20) | 3$^+$ | $^3F_3$ | 220.685 | 0.12 | 2.588(1) | 283(1) |
| 4 | 9.560(20) | 141(10) | 2$^+$(II) | $^3F_2^2$ | 337.83 | 0.18 | 2.748(1) | 146(1) |
| 5 | 10.570(30) | 200(100) | 3$^-$ | $^3D_3^2$ | 1953.33 | 1.5 | 3.758(1) | 187(1) |
| 6 | No res. | – | 1$^-$ | $^3D_1$ | 300.0 | 0.35 | – | – |
| 7 | No res. | – | 1$^+$ | $^3P_1$ | 206.0 | 0.4 | – | – |

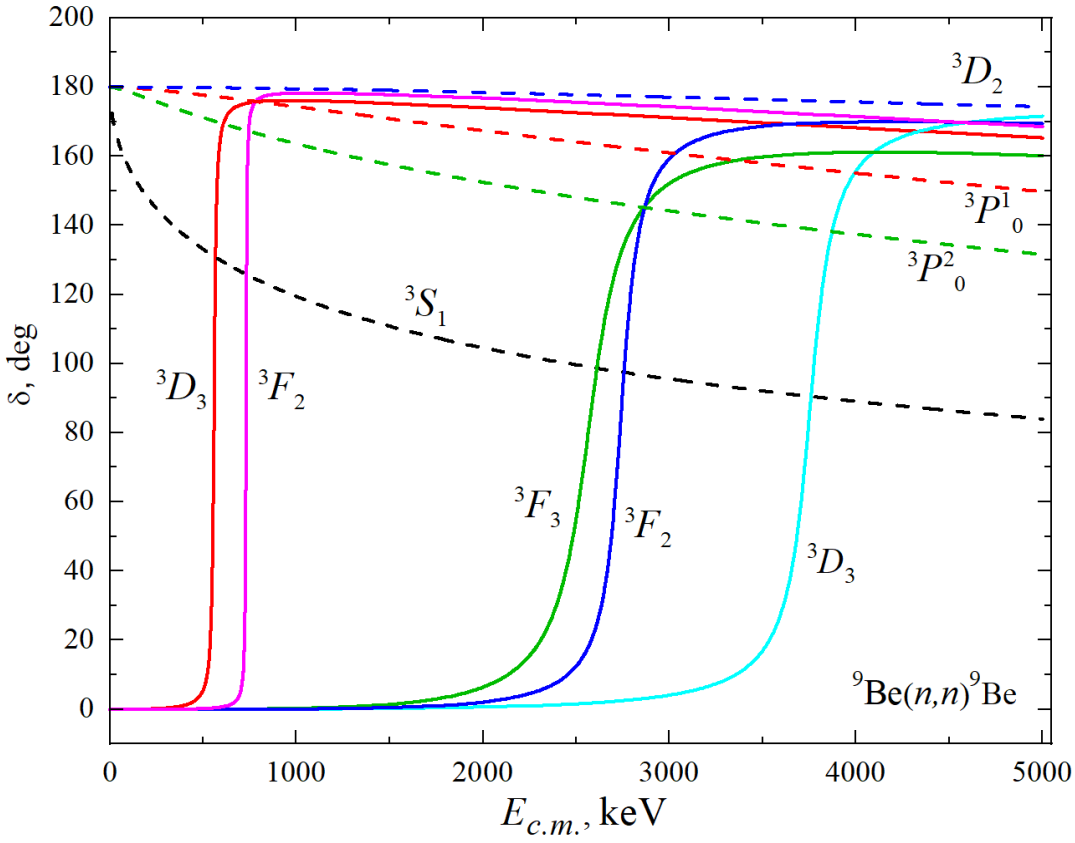


Curves are the calculations with the Gauss potential and parameters from Tables 3.3 and 3.5.

Figure 3.3. Phase shifts of elastic $n^9$Be scattering up to 5 MeV in c.m.

The next $J^{\pi} = 2^{+}$ resonance at an excitation energy of 7.542(1) MeV relates to the resonance at 0.730 MeV c.m. and width of $\Gamma_{c.m.}$ = 6.3(8) keV. We failed to find the potential parameters correctly conveying the characteristics of such a resonance in the *P* wave. We found the potential with FS for the $^3F_2$ wave, which allows to reproduce the $J^{\pi} = 2^{+}$ resonance characteristics. The elastic scattering $^3F_2$ phase shift is shown in Figure 3.3 by a solid magenta curve and illuminates a resonance behavior, reaching 90(1)° at 730(1) keV. Consider a resonance at an excitation energy of 9.4 MeV $J^{\pi} = 3^{+}$. It relates to the resonance at 2.588 MeV c.m. and a width of 291(20) keV. This state was considered as $^3F_3$ wave. The corresponding potential contains one FS that leads to the resonance at 2.588(1) MeV c.m. and a width of 283(1) keV. The scattering phase shift $\delta_F(2.588) = 90(1)^{\circ}$ (solid green curve in Figure 3.3).

The next resonance is located at an excitation energy of 9.560 (20) MeV $J^{\pi} = 2^{+}$. It relates to the $^3F_2$ wave with a resonance at 2.748(20) MeV c.m. and a width of 141(10) keV. The corresponding potential contains one FS and gives $E_{res}$ = 2.748(1) MeV and $\Gamma_{c.m.}$ = 146(1). The scattering phase shift $\delta_F$(2.748 MeV) = 90(1)° (solid blue curve in Figure 3.3).

The last $J^{\pi} = 3^{-}$ resonance at an excitation energy of 10.570(30) MeV we associate with the $^3D_3^2$ wave with a resonance at 3.758(30) MeV c.m. and width of 200(100) keV. It leads to resonance at 3.758 (1) MeV c.m. and a width $\Gamma_{c.m.}$ = 187 (1) keV. The scattering phase shift $\delta_D(3.758) = 90(1)^{\circ}$ (the solid cyan curve in Figure 3.3). The potential of the $^3D_1$ scattering wave leads to zero scattering phase shifts since no resonances are observed in this state. This potential contains a bound FS corresponding to the {541} diagram, and the state for {422} is not bound.

The parameters of the potentials for the nonresonant $^3P_{0,2}$ waves are the same as for the BSs from Table 3.3, and for the $^3P_1$ wave, they are pointed out in Table 3.5. For the $^3S_1$ scattering wave, the parameters of interaction potential from Table 3.3 are used. We do not consider here the resonances at 9.27 MeV with $J^{\pi} = 4^{-}$ [97], 10.150 MeV, and 11.800(50) MeV with $J^{\pi} = 4^{+}$ [98]. They only lead to the *E*2 transitions, which give a noticeably smaller contribution to the cross-sections, contrary to *E*1 transitions.

For the resonating waves, the relation between the scattering phase shift $\delta$ and the resonance width value $\Gamma_{c.m.}$ follows:

$$\Gamma_{c.m.} = 2(d\delta / dE_{c.m.})^{-1} \tag{3.10}$$

Figure 3.3 illustrates the corresponding phase shifts calculated with the potentials from Tables 3.3 and 3.5.

### 3.6 Total cross section of $^9$Be($n$, $\gamma_{0+1+2+3+4+5}$)$^{10}$Be capture

The partial cross-sections are calculated with relations (3.2) – (3.8) and presented in Figure 3.4a. The selection rules for the allowed transitions are provided by the vector

addition of angular momentums in Clebsch-Gordan coefficients, 6j and 9j-symbols in expressions (3.3) and (3.6). The summary of the multiple *NJ* transitions is presented in Table 3.6. The factor $P_J^2(NJ, J_f, J_i)$ in the final column shows the algebraic weight of the corresponding amplitude in a partial cross-section. Figure 3.4b compares present MPCM calculations with those from [16] discussed below.

Within the constructed partial cross-section, we mark the transitions leading to the resonances as bold. These resonances occur via the strong *E*1 transition to the 1st and 2nd ESs, and they are observed in partial ($n,\gamma_1$) and ($n,\gamma_2$) cross-sections in Figure 3.4a.

The strength of *E*2 transitions is much less compared to *E*1. The value of *E*2 cross-sections does not exceed 0.1 $\mu$b, so the resonance structure does not illuminate within the treating energy range. The partial capture ($n,\gamma_0$) to the GS of $^{10}$Be provides the major background for all other partial cross-sections due to the *E*1 transition from the non-resonance $^3S_1$ scattering wave not damped by the centrifugal barrier. Similar transitions one can see for the capture to the 1st and 2nd ESs (No. 5 and 14 in Table 3.6).

Partial cross-sections ($n,\gamma_0$) and ($n,\gamma_4$) are of the same structure. In work [90], radial matrix elements $I_J(k, J_f, J_i)$ defined in (5) and (8) are integrated only up to 20 fm.

That is not sufficient enough when the radial functions refer to the bound states with $E_b$<1 MeV. These are 2nd – 5th ESs. Therefore, only GS and 1st ES integrals $I_J(k, J_f, J_i)$ are calculated correctly, and all the others (2nd – 5th ESs) led to markedly underestimated values of total cross-sections. Here, we have eliminated this inaccuracy and calculated the overlapping integrals (3.5) and (3.8) up to 100 fm. Note the results for the ($n,\gamma_0$) and ($n,\gamma_1$) cross-sections practically do not differ from those obtained in [90]. Corrections inserted in calculations of ($n,\gamma_2$), ($n,\gamma_3$), and $(n,\gamma_4)$ cross-sections sometimes exceed the results of [90] by order of magnitude.

One more remark concerns the input of the ($n,\gamma_5$) capture to the 5th ES into the total cross-section. It follows from Table 3.6 (No. 30 and 31): despite the *strong E*1 transition, there are no resonances; therefore, the role of this partial cross-section is negligible.

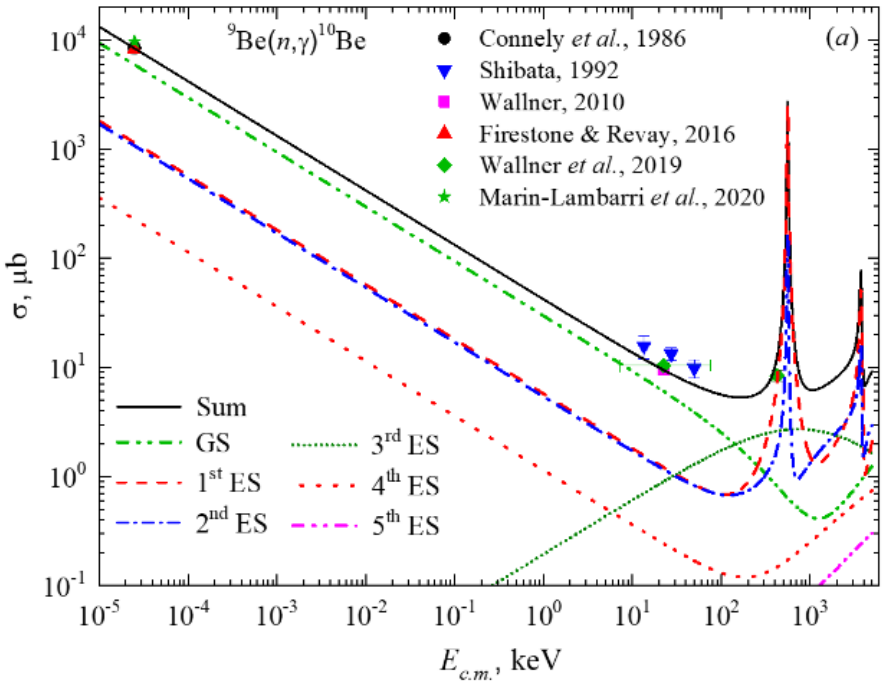


a)

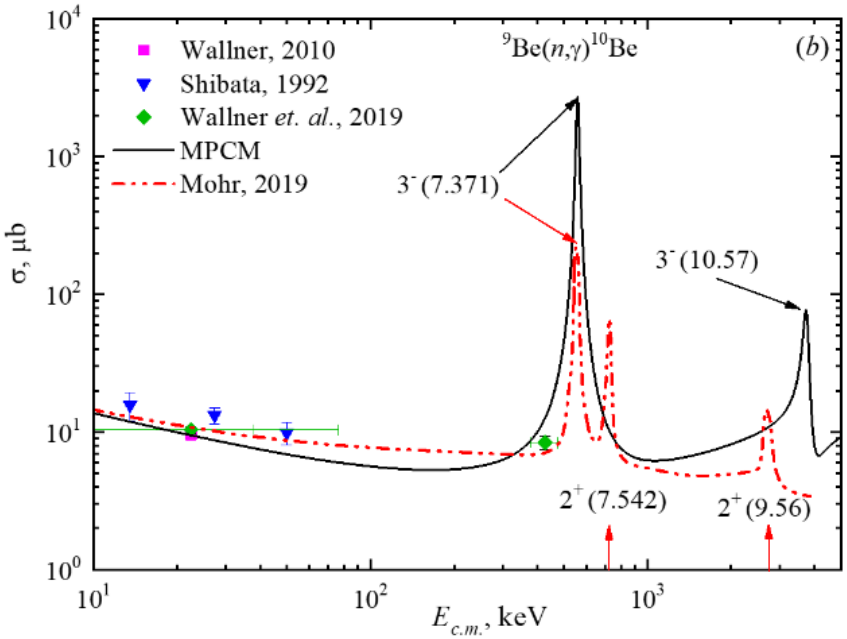


b)

Experimental data: ● – [91], ▲ – [75], ★ – [94] at 25 meV; ■ – [93] at 25 keV, ◆ – [86], ▼ – [119] taken from [86].

a) Present MPCM calculations: the black solid curve is the calculated total cross-section with transitions to all ESs. Partial cross-sections are denoted in the field of the figure and guided in Table 3.6.

b) Comparison of MPCM results and folding model [16]: the black solid curve is the same as in (a), the red double-dotted curve is digitalized cross-section from Figure 1 of [16], arrows show the position of resonances in the initial channel.

Figure 3.4 – Total cross-sections for the reaction of radiative $n^9$Be capture

Table 3.6 – Classification of partial transitions for the $^{9}$Be$(n,\gamma_{0+1+2+3+4+5})^{10}$Be reaction. In column 2, the indicated initial scattering state $[^{2S+1}L_J]_i$ is supplied with the No. of the corresponding potential with parameters given in the pointed table. Resonance transitions are noted as bold. Final state is noted as $[^{2S+1}L_J]_f$. $P_J^2$ are the algebraic factors (1.3) and (1.5)

| No. | $[^{2S+1}L_J]_i$ | $NJ$ transitions | $[^{2S+1}L_J]_f$ | $P_J^2(NJ, J_f, J_i)$ |
|---|---|---|---|---|
| GS (green dot-dotted curve in Figure 3.4a) | | | | |
| 1 | $^3S_1$ (No. 4 Table 3.3) | $E1$ | $^3P_0^1$ | 1 |
| 2 | $^3D_1$ (No. 6 Table 3.5) | $E1$ | $^3P_0^1$ | 2 |
| 3 | $^3P_1$ (No. 7 Table 3.5) | $M1$ | $^3P_0^1$ | 2 |
| 4 | $^3F_2$ (No. 2, No. 4 Table 3.5) | $E2$ | $^3P_0^1$ | 3 |
| 1st ES (red dashed curve in Figure 3.4a) | | | | |
| 5 | $^3S_1$ (No. 4 Table 3.3) | $E1$ | $^3P_2^1$ | 5 |
| 6 | $^3D_1$ (No. 6 Table 3.5) | $E1$ | $^3P_2^1$ | 1/10 |
| 7 | $^3D_2$ (No. 6 Table 3.3) | $E1$ | $^3P_2^1$ | 3/2 |
| 8 | $^3D_3^1$ (No. 1 Table 3.5) | $E1$ | $^3P_2^1$ | 42/5 |
| 9 | $^3D_3^2$ (No. 5 Table 3.5) | $E1$ | $^3P_2^1$ | 42/5 |
| 10 | $^3P_1$ (No. 7 Table 3.5) | $M1$ | $^3P_2^1$ | 5/2 |
| 11 | $^3P_2$ (No. 2 Table 3.3) | $M1$ | $^3P_2^1$ | 15/2 |
| 12 | $^3F_2$ (No. 2, No. 4 Table 3.5) | $E2$ | $^3P_2^1$ | 3/7 |
| 13 | $^3F_3$ (No. 3 Table 3.5) | $E2$ | $^3P_2^1$ | 3 |
| 2nd ES (blue dash-dotted curve from Figure 3.4a) | | | | |
| 14 | $^3S_1$ (No. 4 Table 3.3) | $E1$ | $^3P_2^2$ | 5 |
| 15 | $^3D_1$ (No. 6 Table 3.5) | $E1$ | $^3P_2^2$ | 1/10 |
| 16 | $^3D_2$ (No. 6 Table 3.3) | $E1$ | $^3P_2^2$ | 3/2 |
| 17 | $^3D_3^1$ (No. 1 Table 3.5) | $E1$ | $^3P_2^2$ | 42/5 |
| 18 | $^3D_3^2$ (No. 5 Table 3.5) | $E1$ | $^3P_2^2$ | 42/5 |
| 19 | $^3P_1$ (No. 7 Table 3.5) | $M1$ | $^3P_2^2$ | 5/2 |
| 20 | $^3P_2$ (No. 3 Table 3.3) | $M1$ | $^3P_2^2$ | 15/2 |
| 21 | $^3F_2$ (No. 2, No. 4 Table 3.5) | $E2$ | $^3P_2^2$ | 3/7 |
| 22 | $^3F_3$ (No. 3 Table 3.5) | $E2$ | $^3P_2^2$ | 3 |
| 3rd ES (dark cyan short dotted curve in Figure 3.4a) | | | | |
| 23 | $^3P_0$ (No. 1 Table 3.3) | $E1$ | $^3S_1$ | 1 |
| 24 | $^3P_1$ (No. 7 Table 3.5) | $E1$ | $^3S_1$ | 3 |
| 25 | $^3P_2$ (No. 2 Table 3.3) | $E1$ | $^3S_1$ | 5 |
| 4th ES (red dotted curve in Figure 3.4a) | | | | |

Continue of Table 3.6

| | | | | |
|---|---|---|---|---|
| 26 | ${}^3S_1$ (No. 4 Table 3.3) | $E1$ | ${}^3P_0^2$ | 1 |
| 27 | ${}^3D_1$ (No. 6 Table 3.5) | $E1$ | ${}^3P_0^2$ | 2 |
| 28 | ${}^3P_1$ (No. 7 Table 3.5) | $M1$ | ${}^3P_0^2$ | 2 |
| 29 | ${}^3F_2$ (No. 2, No. 4 Table 3.5) | $E2$ | ${}^3P_0^2$ | 3 |
| 5th ES (magenta dash-dot-dotted curve in Figure 3.4a) | | | | |
| 30 | ${}^3P_1$ (No. 7 Table 3.5) | $E1$ | ${}^3D_2$ | 9/2 |
| 31 | ${}^3P_2$ (No. 2 Table 3.3) | $E1$ | ${}^3D_2$ | 3/2 |

The experimental data for the total $n^9$Be capture cross-sections are presented in [75, 86, 91-94]. In [75], the experimental data for the cross-section at a thermal energy $\sigma_{th} = 8.27(13)$ mb are reported. This value differs a little from the results of [91], where $\sigma_{th} = 8.49(34)$ mb, or [86] where $\sigma_{th} = 8.31(52)$ mb. The most recent measurements of the thermal cross-section give a value of $\sigma_{th} = 9.70(57)$ mb [94] and $\sigma_{th} = 9.70(53)$ mb [120], they differ from the previous results and exceed them by ~15%.

Given certain general assumptions about the interaction potentials of the $n^9$Be channel in the continuous and discrete spectrums, we describe quite well the available experimental data on the total neutron capture cross-section at energies from 25 meV [75, 91] to the lower measured point at 426 keV [86, 92, 93].

However, the early data from [119] at the $E_{c.m.}$ energies ~12–45 keV lie higher than the latest results [86, 91-94]. Figure 3.4a illuminates the smooth increase of the total cross-section with the energy decrease. Low-energy approximation of the neutron radiative capture cross-sections without resonances may be found in [90, 121]. At energies of $10^{-5}$ to 1 keV, the calculated cross-section shown in Figure 3.4a by a solid curve may be approximated as follows:

$$\sigma(\mu\text{b}) = \frac{A}{\sqrt{E_{c.m.}(\text{keV})}} \tag{3.11}$$

Expression (16) refers to the $S$ wave capture cross-section. The value of the constant $A$ = 42.01 μb·keV$^{1/2}$ is determined from one point in total cross-sections at minimum energy equals $10^{-5}$ keV (c.m.). The corrected calculation of $I_J(k, J_f, J_i)$ integrals for the transitions to the 2nd and 4th ESs led to an increase in coefficient $A$ in expression (16) from 40.2 μb·keV$^{1/2}$ [90] to 42.01 μb·keV$^{1/2}$ by 4%.

We consider the modulus of the relative deviation between the theoretical cross-section and its approximation by (3.12):

$$M(E) = \left| [\sigma_{ap}(E) - \sigma_{theor}(E)] / \sigma_{theor}(E) \right|, \tag{3.12}$$

in the energy range from $10^{-5}$ to 1 keV. Below 1 keV, the deviation $M(E)$ does not exceed 0.9%. For example, the application of approximation (16) at 25.3 meV gives the value $\sigma_{th} = 8.35$ mb, which is within the error limits of the results of [75, 91].

Let us comment on the only theoretical calculations of the total cross-sections of $^{9}$Be($n,\gamma_{0+1+2+3+4+5}$)$^{10}$Be reaction performed in the folding cluster model [16, 86]. In Figure 3.4b are compared total cross-section with calculations in [16], as they are in near the same energy interval. The results from [86] are very close to those of Mohr [16] and done within the same approach. In [16] four low-laying resonances which correspond to the states in $^{10}$Be at $E_x$=7.371 MeV $(J^{\pi}, L_J = 3^-, D_3)$, 7.542 MeV $(2^+, P_2)$, 9.27 MeV $(4^-, D_4)$, and 9.56 MeV $(2^+, P_2)$ are included in consideration.

The 1st, 3rd, and 4th provide the resonance structure of the total cross section in Figure 3.4b (red double-dotted curve). In classification, $2^+$ resonances are associated with *F*-waves but not *P*-waves. This identification issue may be regarded as open. However, these $2^+$ states lead to the *E*2 capture cross-sections in both cases. As mentioned above, in present calculations, the *E*2 resonance capture cross-section does not exceed 0.1 μb; therefore, the results of Mohr [16] are unclear to us. The $4^-$ resonance due to its minor role was not considered.

### 3.7 Reaction rate

The corresponding reaction rates have been calculated based on the partial and summed cross-sections illustrated in Figure 3.4a. Present results are compared with the data on the reaction rate of [16, 45, 86].

The reaction rate for the radiative neutron capture is calculated according to [14] in units cm$^3$mol$^{-1}$s$^{-1}$:

$$N_A\langle\sigma v\rangle = 3.7313\cdot 10^4 \mu^{-1/2} T_9^{-3/2} \int_0^{\infty} \sigma(E) E \exp(-11.605E/T_9) dE. \qquad (3.13)$$

Here the reduced mass μ is in amu, the temperature $T_9$ in $10^9$K, the total cross section σ($E$) in μb, and $E$ in MeV. The integration was implemented over 100 000 points in the energy range $10^{-5}$ to $5\cdot 10^3$ keV.

Figure 3.5 shows the calculated rate of $^{9}$Be($n,\gamma_{0+1+2+3+4+5}$)$^{10}$Be reaction with capture to the GS and all ESs. The partial contributions of transitions to different ESs are denoted in the figure field, and the black solid curve shows the total rate.

The total reaction rate is approximated by the analytical expression from [86]:

$$N_A\langle\sigma v\rangle = a_1(1.0 + a_2 T_9^{1/2} + a_3 T_9 + a_4 T_9^{3/2} + a_5 T_9^2 + a_6 T_9^{5/2}) + \\ + a_7 / T_9^{3/2} \exp(-a_8 / T_9) \qquad (3.14)$$

We provide the approximation parameters $\chi^2 = 0.001$ in Table 3.7. The accuracy of the calculated curve is 5%.

Table 3.7 – Reaction rate approximation parameters

| $i$ | $\alpha_i$ | $i$ | $\alpha_i$ | $i$ | $\alpha_i$ | $i$ | $\alpha_i$ |
|---|---|---|---|---|---|---|---|
| 1 | 1190.438 | 3 | 0.6435 | 5 | 0.00178 | 7 | $1.31549 \cdot 10^{6}$ |
| 2 | –0.15943 | 4 | –0.00344 | 6 | $-1.2853 \cdot 10^{-4}$ | 8 | 6.4213 |

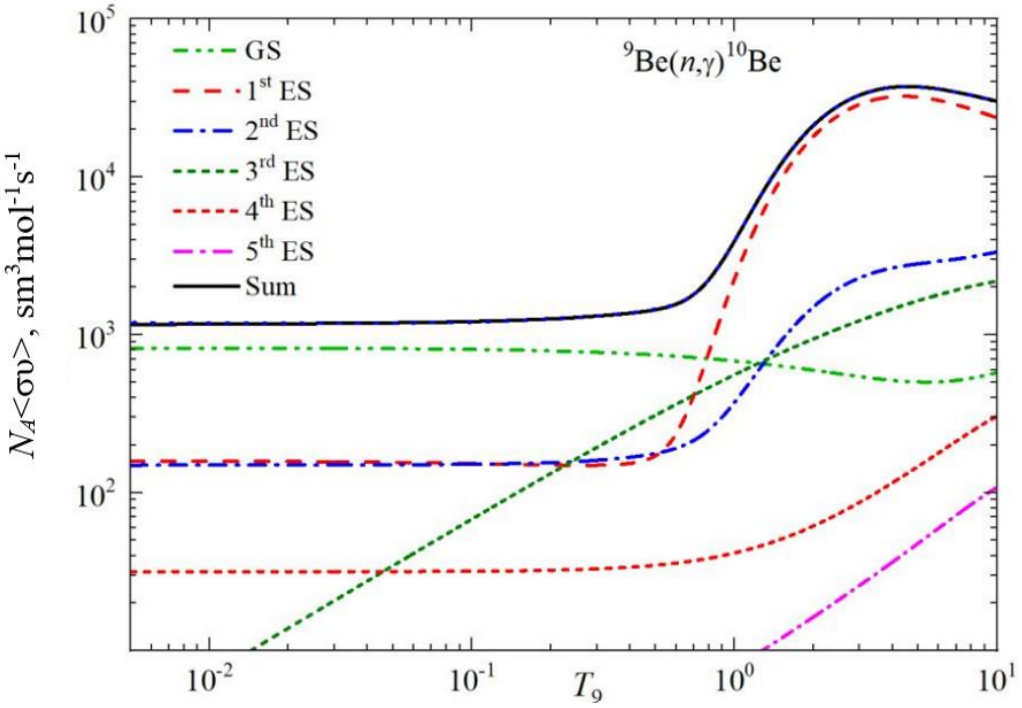


Figure 3.5 – Total and partial reaction rates of neutron capture on $^{9}$Be nucleus

We demonstrate in Figure 3.6 the input of the resonance cross-sections into the total reaction rate. Comparison of $\langle \sigma v \rangle_{res}$ (black solid) and $\langle \sigma v \rangle_{non-res}$ (red dashed) shows the rising of the total reaction rate from the ~ $0.4T_9$.

Their difference reaches the order of magnitude in the maximum at ~ $4T_9$. Note the non-resonance $\langle \sigma v \rangle_{non-res}$ is calculated with switched-off the resonance amplitudes No. 4, 8, 9, 12, 13, 17, 18, 21, 22, and 29 of Table 3.5.

Another comment concerns the present calculations of the $^{9}$Be($n$,$\gamma_{0+1+2+3+4+5}$)$^{10}$Be reaction rate and those from the [16, 86] as well as [45]:

(i) Calculations of the total cross-sections in [16, 86] are performed in a folding cluster model but with subdivision into the direct capture part $\sigma_{DC}$ and resonance one $\sigma_R$, *ad hoc* $\sigma = \sigma_{DC} + \sigma_R \pm 2(\sigma_{DC} \cdot \sigma_R)^{1/2} \cos(\delta_R)$ [122, 123]. Contrary, in the MPCM approach, there is no such subdivision, and consequently, there are no problems with uncertainties coming from the interference term. Both types of energy dependence are well-seen as *continuous* behavior of scattering phase shifts $^{3}D_3$, $^{3}F_2$, and $^{3}F_3$ in Figure 3.3. Within this calculating scheme, the corresponding scattering functions $\chi_i$ are obtained and incorporated into the overlapping integrals (1.3) and (1.5). Calculations in [45] are the modeless ones.

(ii) The most significant input into the cross-section at energies higher than ~ 500 keV is coming from the first $3^-$ (0.559) resonance. In [16, 86], to calculate the $\sigma_R$ according to the Breit-Wigner formula, the experimental data on the first $3^+$ resonance state is exploited (see, for example, Table 2 in [16]). MPCM reproduces the parameters of this resonance also. In [16, 86], the value of $\sigma(0.559\ \text{MeV}) \approx 200\ \mu\text{b}$ is reported. In the present calculations, we obtained the value of $\sigma(0.559\ \text{MeV}) \approx 1200\ \mu\text{b}$. This difference illuminates in corresponding reaction rates in the near same proportion: present calculations exceed the reaction rates of [16, 86] starting from ~ 0.8 $T_9$ and show the near 5 rising factor at ~ $5T_9$.

(iii) We confirm the conclusion of Mohr [16] on the temperature dependence of the reaction rate at the low range $T_9$ contrary to the constant $\langle \sigma v \rangle$ behavior proposed in [45] (see insert in Figure 3.6).

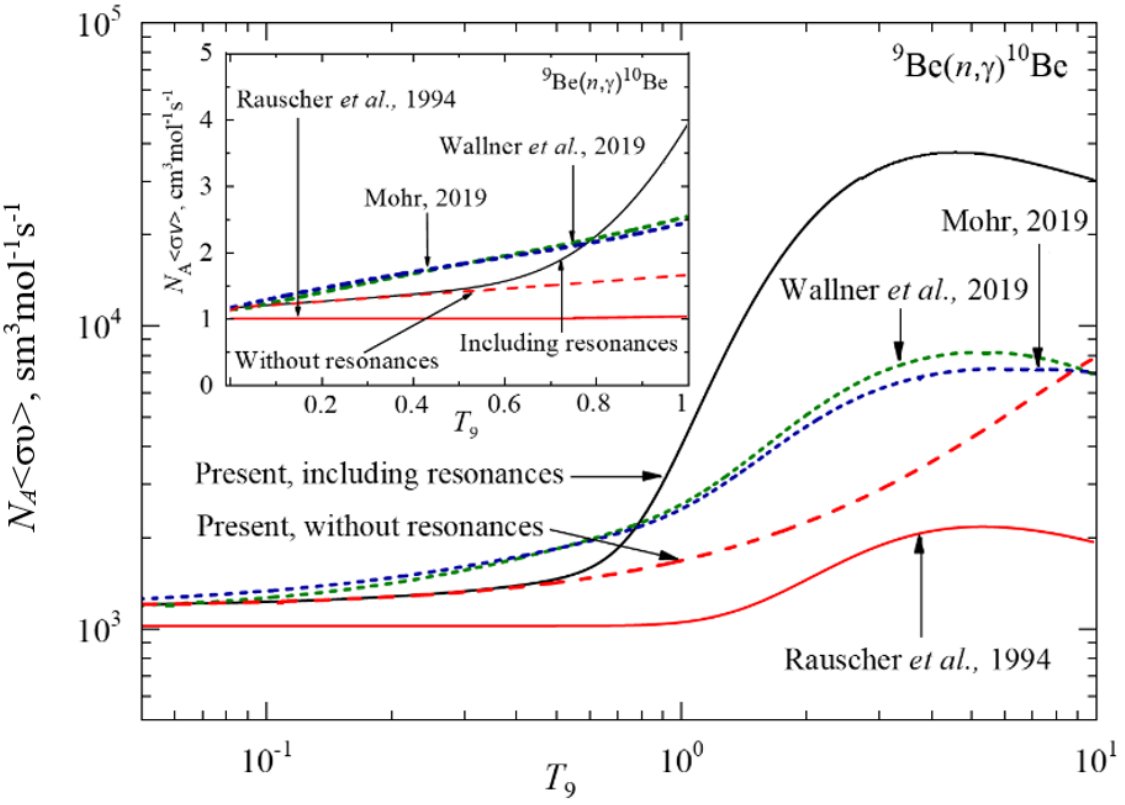


The dark green short, dashed curve is the result of [86], the blue short, dashed curve is the result of [16], and the red solid curve is the result of [45], the black solid curve is the total reaction rate including resonances (same as in Figure 3.5), the red dashed curve is the result of present calculations without resonance amplitudes.

Figure 3.6 – Comparison of the total reaction rates of the radiative neutron capture on

### 3.8 Concluding remarks

The partial and total cross-sections of $^9$Be$(n,\gamma_{0+1+2+3+4+5})^{10}$Be reaction are calculated in the energy range from $10^{-5}$ to 5 MeV in the MPCM. The expansion of the energy range to 5 MeV allows us to consider five $^3D_3^1$, $^3F_2^1$, $^3F_3$, $^3F_2^2$, and $^3D_3^2$ resonances

and estimate their signature in the total cross-section. A narrow resonance of $E_x$ = 0.730 MeV is proposed as $^3F_2^1$ state, but not the $P$ one. Comparing the GS partial cross-section, the transitions to the 1st and 2nd ESs give essential input in the total cross-section. The role of the $(n,\gamma_3)$ process is illuminating with energy increasing. The minor role of the $(n,\gamma_4)$ and $(n,\gamma_5)$ processes is proved numerically.

The calculated thermal cross-section $\sigma_{th}$ = 8.35 mb is in good agreement with experimental data of [45, 91-93], which are ~ 10% lower than the early measurements [94, 120]. That is a reason for discussions addressed to the experimentalists.

The total and partial rates of $^9$Be$(n,\gamma_{0+1+2+3+4+5})^{10}$Be reaction are calculated in the temperature range of 0.001 to 10 $T_9$ and are approximated by the analytical expression. The inclusion of resonances shows their impact on the corresponding reaction rate within the factor 4-5 rising at $T_9$ >1, comparing the results of [16, 86].

The lack of experimental data on the cross-sections higher than 500 keV illuminates the problem of the quantitative reproducing of the first 0.559 MeV resonance, as it makes the most significant contribution to the rate of $^9$Be$(n,\gamma)^{10}$Be reaction. New experimental measurements are in high demand.

Finally, it is worth mentioning that theoretical research of the $^9$Be$(n,\gamma)^{10}$Be reaction can be applied to the isobar-analog process $^9$Be$(p,\gamma)^{10}$B. The comparative study of these processes within the same theoretical approach can provide the beryllium–boron branching under discussion.

## 4 PROPOSAL FOR THE RADIATIVE NEUTRON CAPTURE $^{13}$B($n,\gamma_{0+1}$)$^{14}$B REACTION

### 4.1 Role of $^{13}$B($n,\gamma_{0+1}$)$^{14}$B nuclear reaction in the Boron-Carbon-Nitrogen network

The conventional study of *r*-processes focuses on producing heavy, unstable nuclei. Among the thousands of publications, one may be impressed by recent reviews on this item [11, 124, 125].

The interests of the present work lay in the plane of study of the *r*-processes that occur with light 1*p*-shell nuclei and are motivated by the concepts suggested in [3, 6, 82]. Kajino *et al.* suggested networks for the primordial nucleosynthesis in inhomogeneous Big Bang models in [82] and its further extension to the evolution of the light elements in cosmic rays [3].

More than 20 years ago, Terasawa and co-authors raised the problem concerning the role of light, neutron-rich nuclei ($Z < 10$) during *r*-process nucleosynthesis in supernovae [6]. We are interested in the possible branching of boron and carbon chains leading to the formation of heavier up to the oxygen isotopes as the development of a primordial chain starting from $^{7}$Li (see Figure 6 in [126] and present illustration in Figure 4.1).

Further developments on the sensitivity studies of the ($n,\gamma$) reactions running through the neutron-rich boron $^{11–14}$B and $^{12–19}$C carbon isotopes were implemented in [126], and these reactions have been included in the heavy nuclei network production. Almost all reaction rates for the boron chains used in this model calculations were taken from [45], and their uncertainties were estimated to be at least a factor of two [126]. It turned out that only the $^{13}$B($n,\gamma$)$^{14}$B process on boron isotopes shows zero impact on the heavy elements production.

We suggest the new estimation of the $^{13}$B($n,\gamma$)$^{14}$B reaction rate within the MPCM approach, which significantly differs from the results of [45]. So that the conclusions of [126] on the negligible role of $^{13}$B($n,\gamma$)$^{14}$B reaction in the heavy nuclei network production will get reasons for the revision.

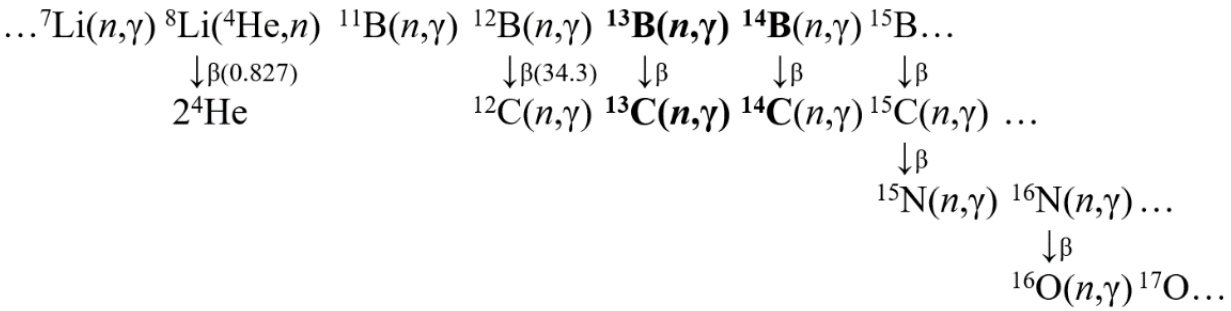


Figure 4.1 – The part of the nuclear reaction network responsible for producing the light elements in primordial nucleosynthesis from [3, 6, 82]

The comparative analysis of the reaction rates of the processes in Figure 4.1 is a way to define the contribution of $^{13}$B($n,\gamma$)$^{14}$B reaction in the Boron-Carbon-Nitrogen

network. The early MPCM research on the neutron radiative capture reactions relevant to those in Figure 4.1 are provided by the following Refs.: $^{10}$B($n,\gamma$)$^{11}$B reaction is examined in [78], the reaction chain $^{11}$B($n,\gamma$)$^{12}$B($n,\gamma$)$^{13}$B we considered in [32, 88, 89]; $^{12}$C($n,\gamma$)$^{13}$C we investigated in [127], $^{13}$C($n,\gamma$)$^{14}$C reaction is published in [128], $^{14}$C($n,\gamma$)$^{15}$C (not published yet), the research of $^{15}$N($n,\gamma$)$^{16}$N process is in [129].

As for reaction $^{16}$O($n,\gamma$)$^{17}$O, the measured cross-section and its rate calculated in the direct reaction capture model are presented in recent work [130]. There are no data on the $^{14}$B($n,\gamma$)$^{15}$B and $^{16}$N($n,\gamma$)$^{17}$N reaction rates today.

Experimental study of $^{13}$B($n,\gamma$)$^{14}$B reaction is presented by the only measurement of the neutron breakup of the $^{14}$B isotope via Coulomb dissociation performed in inverse kinematics [13]. The total cross-section of $^{13}$B($n,\gamma$)$^{14}$B is derived from the Coulomb breakup of $^{15}$B and is very tentative. Therefore, theoretical model calculations are highly demanded to feel the informational gap on $^{13}$B($n,\gamma$)$^{14}$B reaction in boron chains in Figure 4.1.

Another problem concerns the lack of well-defined information on the spectral structure of $^{14}$B required for applying the MPCM. We use current data on the $^{14}$B spectrum [98], as against the previous data from the earlier review [131], to classify the possible multipole structure of the corresponding cross-sections of present and future interest.

Noteworthy, the reactions $^{13}$B($n,\gamma$)$^{14}$B and $^{13}$C($n,\gamma$)$^{14}$C are the isobar-analogous, and the latter one is examined in detail in [128]. Although $^{14}$B and $^{14}$C are not mirror nuclei, the Young diagrams provide some common features of orbital symmetry. We exploited this fact while classifying the allowed and forbidden states in discrete and continuum spectra of $n$ + $^{13}$B channels.

Within the MPCM, the total cross-sections of $^{13}$B($n,\gamma$)$^{14}$B radiative capture onto the ground and first excited states of $^{14}$B are calculated, as well as the reaction rates in the interval of $0.01T_9$ – $10T_9$. Based on the reaction rate's interval, we evaluated the balance between $^{14}$B synthesis via the radiative neutron capture reaction $^{13}$B($n,\gamma$)$^{14}$B and $^{13}$B decay inhibiting this synthesis.

### 4.2 Structure of states for $n^{13}$B system

We preface the calculations of the reaction cross-sections by analyzing and commenting on the data on the $^{14}$B spectrum following work [98]. The spectrum of $^{14}$B nucleus selected levels is shown in Figure 4.2. The structure of the bound ground state $J^\pi$, $T = 2^-$, 2 is assigned as a combination of two main orbital components: $\psi_{GS} = \alpha_S |S\rangle + \alpha_D |D\rangle + ...$, where corresponding weights are $\alpha_S = 0.71(5)$ and $\alpha_D = 0.17(5)$. In the present calculations, we consider the *S*-component only. As for the excited $J^\pi = 1^-$ state, it was found to be the dominant *S*-component with a weight $\alpha_S = 0.94(20)$ .

Now let us turn to the comments on the resonance states in the spectrum of $^{14}$B. The 1$^{st}$ resonance can be associated with the spin-mixed $^{3+5}P_1$ wave at the energy $E_{c.m.}$ = 0.305(20) MeV since $J^\pi = 3/2^-$ for $^{13}$B and $J^\pi = 2^-$ for $^{14}$B. Radiative neutron capture from this state proceeds via $E1$ transition to the ground $^5S_2$ and excited $^3S_1$

states.

The 2nd resonance has $J^{\pi}=3^{-}$ and may be excited at 0.41 MeV as a $^{3+5}D_2$ state so that the $E2$ transition only may occur. Since we are operating within the long-wave approximation for the electromagnetic interaction Hamiltonian here and further, we do not consider the $E2$ or $M2$ transitions if selection rules do not forbid the stronger $E1$ and $M1$ processes.

The 3rd resonance with $J^{\pi}=2^{-}$ may be excited at 0.89(7) MeV in $^{5}S_2$ or $^{3+5}D_2$ scattering waves. From the $^{5}S_2$ scattering wave, the $M1$ transition to GS is allowed, but we assume that due to the large width $\Gamma_{c.m.}=1.0(5)$ MeV, this resonance does practically not affect the total capture cross-section if this resonance is considered as the spin-mixed $^{3+5}D_2$ wave.

The 4th resonance at an excitation energy of 2.08(5) MeV is defined as $J^{\pi}=4^{-}$ state, but its width is unknown. It may be matched to a $^{5}D_3$ scattering wave, leading to the $E2$ transition, and not considered in present calculations.

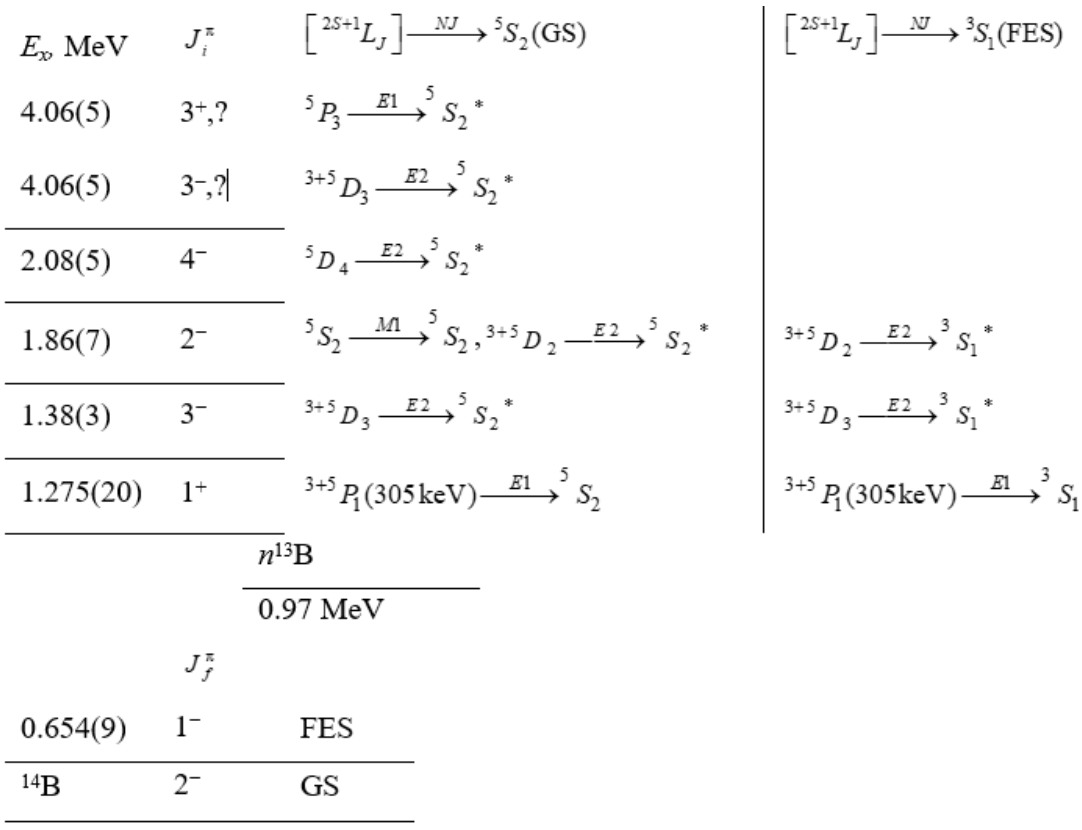


* indicates the transitions we do not consider.

Figure 4.2 – Spectrum of $^{14}$B nucleus in MeV [98]

The position of the 5th resonance in the spectrum is defined at 4.06(5) MeV, with a width of 1.2(5) MeV and total spin $J = 3$, but the parity is unknown [98]. We assume a positive parity for this level and construct a resonance potential for the $^{5}P_3$ scattering wave. $^{5}P_3$ state leads to the $E1$ transition to the $^{5}S_2$ ground state of $^{14}$B. Its effect on the total cross-section is weak due to its large width. If the negative parity is assumed, this

state is the analog of the 2nd resonance state commented above.

We do not denote two more levels in the spectrum at energies of 2.32(4) MeV and 2.97(4) MeV since only their energies are known [98]. Transitions pointed *as not included in consideration* in Figure 4.2 one may assume as perspectives for the future study of $^{13}$B($n,\gamma$)$^{14}$B reaction while the new experimental data on the $^{14}$B spectrum will appear.

### 4.3 Classification of states and interaction potentials

The cross-sections of the $E1$ and $M1$ capture to the GS are provided by the following transition amplitudes:

$$\begin{aligned} &{}^{3+5}P_1(305\text{keV}) \xrightarrow{E1} {}^5S_2,\ {}^5P_3 \xrightarrow{E1} {}^5S_2,\ {}^{3+5}P_2 \xrightarrow{E1} {}^5S_2, \\ &{}^3P_0 \xrightarrow{E1} {}^5S_2,\ {}^5S_2 \xrightarrow{M1} {}^5S_2. \end{aligned} \tag{4.1}$$

For the cross-sections of the $E1$ and $M1$ capture to the ES of $^{14}$B, these transition amplitudes are:

$$\begin{aligned} &{}^3P_1(305\text{keV}) \xrightarrow{E1} {}^3S_1,\ {}^3P_0 \xrightarrow{E1} {}^3S_1,\ {}^3P_2 \xrightarrow{E1} {}^3S_1, \\ &{}^3S_1 \xrightarrow{M1} {}^3S_1. \end{aligned} \tag{4.2}$$

The calculation of the corresponding cross-sections is performed following formalism [19, 27, 118, 132] adapted to the selected $E1$ and $M1$ transitions:

$$\sigma(N1, J_f) = \frac{2\pi e^2}{3\hbar^2}\left(\frac{\mu K}{k}\right)^3 \sum_{L_i, J_i} (2J_i + 1) \cdot B^2(N1) \cdot I^2_{NJ}(k, J_f, J_i), \tag{4.3}$$

$$B^2(E1) = \frac{25}{m^2_{^{13}\text{B}}},\ I_{EJ}(k, J_f, J_i) = \left\langle \chi_f \left| r^J \right| \chi_i \right\rangle \tag{4.4}$$

$$B^2(M1) = 3\left(\frac{\hbar}{m_0 c}\right)^2 \left[\frac{\mu_n}{m_n} - \frac{\mu_{^{13}\text{B}}}{m_{^{13}\text{B}}}\right]^2,\ I_{MJ}(k, J_f, J_i) = \left\langle \chi_f \left| r^{J-1} \right| \chi_i \right\rangle \tag{4.5}$$

Notations in Eqs. (4.3)–(4.5): $N1$ = $E1$ or $M1$, $\mu$ is reduced mass in $n$ + $^{13}$B channel, $K$ is $\gamma$-quantum wave number, $K = E_\gamma / \text{h}c$ . $k$ is the relative motion wave number related to the non-relativistic kinetic energy as $E_{c.m.} = \hbar^2 k^2 / 2\mu$, $J_i$ and $J_f$ are the total angular momentums, multipolarity is fixed as dipole $J$ = 1, $I_{NJ}(k, J_f, J_i)$ are the radial matrix elements over the relative distance $r$. We use masses of the $m_n = 1.00866491597$ amu and $m_{^{13}B} = 13.0177802$ amu , the constant $\hbar^2 / m_0 = 41.4686$

MeV·fm$^2$, where $m_0$ is the atomic mass unit (amu). Magnetic moments in (4.5) are given in nuclear magneton $\mu_N$: $\mu_N = -1.9130\mu_N$ and $\mu_{^{13}B} = 3.1778\mu_N$ [98, 131].

Radial functions $\chi_i$ and $\chi_f$ are the numerical solutions of the Schrodinger equation with central interaction potential of Gaussian type for a fixed combination of angular momentums *JLS*:

$$V\left({}^{2S+1}L_J, r\right) = -V_0\left({}^{2S+1}L_J\right)\exp\left\{-\alpha\left({}^{2S+1}L_J\right)r^2\right\}, \tag{4.6}$$

where the potential parameters $V_0$ and $\alpha$ depend on the momentums $[{}^{2S+1}L_J]_{i,f}$ of the partial wave.

Following (4.1) and (4.2), *S* and *P* waves provide the transition amplitudes in the initial continuum channel. The classification of orbital states by Young diagrams for the 14-nucleon system in the channel $A = 13 + 1$ proved that *S* waves are allowed only, and *P* waves have a FS also [128]. Since there are no complete tables of products of Young diagrams for a system with $A > 8$, we complemented the symmetry analysis with the formalism of the Translationally invariant shell model (TISM) [133, 134]. Therefore, we treated the option of the interaction potential with FS for *S* waves.

The classification of orbital states by Young diagrams defines the optimization range of the potential depth $V_0$, i.e., if FS exists in the given channel, the potential should be deep enough to include this state. Otherwise, it may be shallow. Shallow potentials are appropriate for the description of scattering states without resonances and should give the phase shifts close to zero.

Deep non-resonance potentials should also provide the moderate energy dependence of phase shifts, which might be normalized according to the Levinson theorem (see details in [25]). In the case of the resonance scattering states, the potential (4.6) should fit the additional conditions – the reproducing of the resonance position $E_{c.m.}$ and its width $\Gamma_{c.m.}$ within the experimental uncertainties.

Parameters of ${}^{3+5}P_1$ wave potential are matched with the experimental values of the resonance position $E_{c.m.}$ = 305(20) keV and width $\Gamma_{c.m.}$ = 100(20) keV [98]. Calculations with potential No. 1 in Table 4.1 lead to $E_{c.m.}$ = 305(1) keV and $\Gamma_{c.m.} = 106(1)$ keV. The corresponding ${}^{3+5}P_1$ phase shift shown in Figure 4.3 (red solid curve) reveals the resonant behavior and equals 270(1)° at 305 keV.

We provide the potential parameters of the neutron scattering on the $^{13}$B in Table 4.1. Non-resonance ${}^{3+5}P_2$, ${}^5P_3$, and ${}^3P_0$ waves are provided by potential No. 2 with FS from Table 4.1. Their phase shifts are normalized to 180(1)° according to the generalized Levinson theorem (green dashed curve in Figure 4.3).

Table 4.1 – Parameters of interaction potentials of $n$ + $^{13}$B continuum

| No. | $\left[{}^{2S+1}L_j\right]_i$ | $V_0$, MeV | $\alpha$, fm$^{-2}$ |
|---|---|---|---|
| 1 | ${}^{3+5}P_1$ – resonance at 305 keV | 618.035 | 0.8 |
| 2 | ${}^{3+5}P_2$, ${}^5P_3$, ${}^3P_0$ – non-resonance | 1220.0 | 1.0 |

Continue of Table 4.1

| | | | |
|---|---|---|---|
| 3 | ${}^5S_2$, ${}^5S_1$ – non-resonance | 0.0 | 0.0 |
| 4 | ${}^5S_2$ – non-resonance | 315.0 | 1.0 |

As for the non-resonance *S*-waves, we consider two variants of the interaction potentials. No. 3 from Table 4.1 refers to the case without the FS and leads to zero scattering *S*-phase shift. The inclusion of FS in consideration leads to 180(1)° phase shift with parameters No. 4 from Table 4.1. The construction of the BS potentials is based on the demands to reproduce the channel binding energy $E_b$ and match the corresponding asymptotic constant [135].

We use the well-known relation for the asymptotic normalizing coefficient $A_{NC}$ and dimensionless asymptotic constant $C_w$ :

$$C_w = \frac{A_{NC}}{\sqrt{2k_0}} \cdot \frac{1}{\sqrt{S_F}} \tag{4.7}$$

where relative wave number $k_0$ is related to binding energy $E_b = \hbar^2 k_0^2 / 2\mu$ and $S_f$ is the spectroscopic factor. Note that experimental data on the $A_{NC}$ usually found from the peripherical reactions alone with the spectroscopic factor $S_f$ are the input information for the calculations of the theoretical values $C_w$. in [136] reported the values $A_{NC} = 0.73(10)$ fm$^{-1/2}$ obtained from the measurements of the breakup cross-sections for the reaction ${}^9$Be(${}^{14}$B,${}^{13}$B+$\gamma$)X at NSCL (National Superconducting Cyclotron Laboratory, Michigan State University).

Data on the spectroscopic factors $S_F$ = 0.71(19) [137] and $S_F$ = 0.66 [138] lead to the interval $0.52 \leq S_F \leq 0.9$. Consequently, the range for the dimensionless constant is $C_w$ = 1.40(38). There is a number of phase shift equivalent potentials, which reproduce the channel binding energy exactly but lead to different radial wave functions. We exploited the $C_w$ constant to constrain the choice of corresponding potential parameters. The asymptotic constant $C_w$ is not single defined but has a range coming from experimental $A_{NC}$ and $S_F$ values.

There is also a variety of $V_0$ and α parameters which provide the binding energy $E_b$ in the $n$ + ${}^{13}$B channel within the $C_w$ range. This is illuminated in the band for corresponding cross-sections. For example, the details of the computing methods we use may be found in [139].

Parameters of the GS potentials of ${}^{14}$B in the $n{}^{13}$B channel given in Table 4.2 reproduce the binding energy of $E_b$ = -0.9700 MeV. The potentials of the GS Nos. 1,2 and 3,4 have nearly the same $C_w$ in pairs and allow to illuminate the effects of the FS. The charge $R_{ch}$ and matter $R_m$ radii are calculated with these parameter sets according to the [34] procedure.

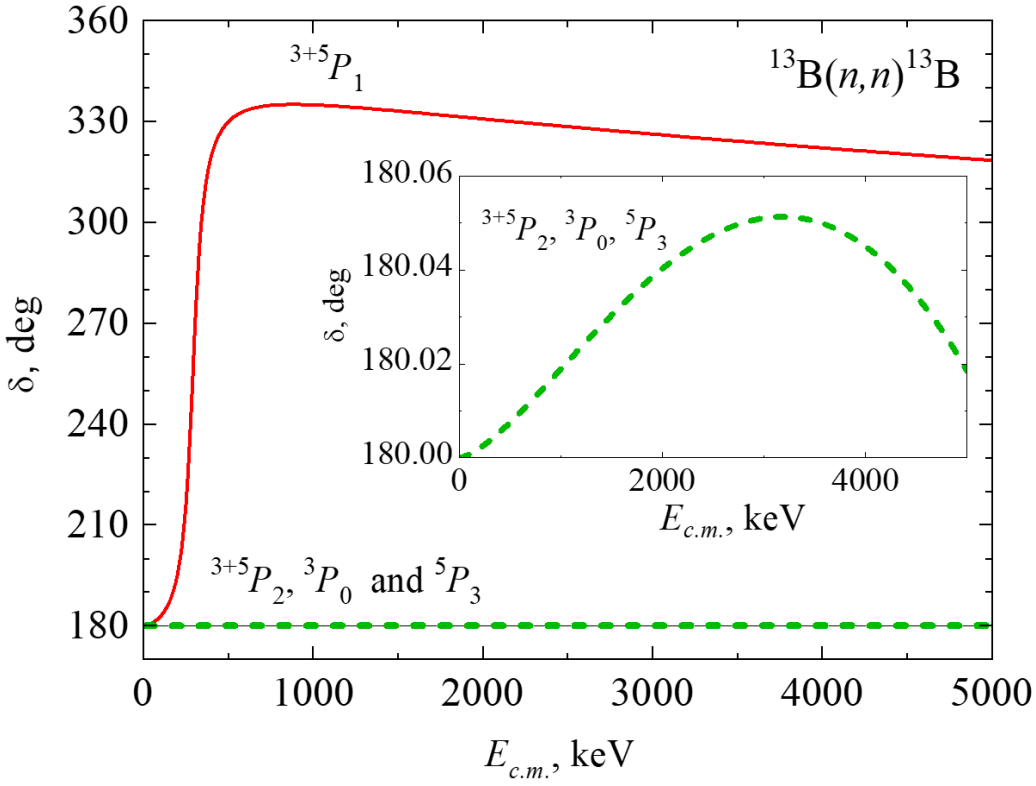


Red solid curve – resonance $^{3+5}P_1$ wave, green dashed curve – non-resonance $^{3+5}P_2$, $^3P_0$, and $^5P_3$ waves.

Figure 4.3 – *P* wave phase shifts calculated in MPCM with parameters of Table 4.1.

To calculate the $^{14}$B radii, we use the following input information: for $^{13}$B the known values are $R_{ch}(^{13}B)$ = 2.48(3) fm and $R_m(^{13}B)$ = 2.41(5) fm [140]; the neutron matter radius is equal to the proton one $R_m(n) = R_m(p)$ = 0.8414(19) fm , and the neutron charge radius $R_{ch}(n)$ = 0. The obtained results for $^{14}$B listed in Table 4.2 are in good agreement with the experimental values $R_{ch}(^{14}B)$ = 2.50(2) fm and $R_m(^{14}B)$ = 2.52(9) fm of [140].

Table 4.2 – Parameters of the GS potentials of the $^{14}$B in $n^{13}$B channel and calculated asymptotic constant $C_w$, $R_{ch}$, and $R_m$ radii

| No. | $\left[{}^{2S+1}L_j\right]_i$ | $V_0$, MeV | $\alpha_2$, fm$^{-2}$ | $C_w$ | $R_{ch}$, fm | $R_m$, fm |
|---|---|---|---|---|---|---|
| 1 | $^5S_2$ without FS | 19.0756 | 0.2 | 1.40(1) | 2.50 | 2.62 |
| 2 | $^5S_2$ with FS | 217.486 | 0.5 | 1.42(1) | 2.50 | 2.63 |
| 3 | $^5S_2$ without FS | 6.1237 | 0.04 | 2.10(1) | 2.52 | 2.81 |
| 4 | $^5S_2$ with FS | 49.262 | 0.1 | 2.15(1) | 2.52 | 2.84 |

The ES potentials of $^{14}$B in the $n^{13}$B channel with parameters given in Table 4.3 reproduce the binding energy $E_b$ = 0.3160 MeV [34]. There is no data on the $A_{NC}$ of the

excited $1^-$ state, so the corresponding $C_w$ constants in Table 4.3 well as $R_{ch}$ and $R_m$ radii may be recommended for future measurements. Along with Table 4.2, the potentials of the ES No. 1,2 and 3,4 are grouped in pairs for the same purpose to monitor the FS effects.

Table 4.3 – Parameters of the ES potentials of the $^{14}$B in $n^{13}$B channel and calculated asymptotic constant $C_w$, $R_{ch}$, and $R_m$ radii

| No. | $\left[{}^{2S+1}L_j\right]_i$ | $V_0$, MeV | $\alpha$, fm$^{-2}$ | $C_w$ | $R_{ch}$, fm | $R_m$, fm |
|---|---|---|---|---|---|---|
| 1 | ${}^3S_1$ without FS | 15.75681 | 0.2 | 1.21(1) | 2.53 | 2.97 |
| 2 | ${}^3S_1$ with FS | 208.3937 | 0.5 | 1.22(1) | 2.53 | 2.98 |
| 3 | ${}^3S_1$ without FS | 4.27985 | 0.04 | 1.53(1) | 2.56 | 3.23 |
| 4 | ${}^3S_1$ with FS | 44.71865 | 0.1 | 1.56(1) | 2.56 | 3.27 |

Note the interaction potentials may depend on different diagrams for the same orbital $L$-waves of continuous and discrete spectrums [24]. $S$-wave potentials in Table 4.1 for the continuum and Tables 4.2 and 4.3 for the bound states are different. This is an important remark in the case of $M1$ transitions. Otherwise, the radial matrix elements in (4.5) at $J = 1$ is equal to zero due to the orthogonality of the bound and scattering radial functions calculated in the same potential.

### 4.4 The total cross-sections of the $^{13}$B($n,\gamma$)$^{14}$B reaction

The effect of the asymptotic constant $C_w$ on the total cross-sections for $^{13}$B($n,\gamma_0$)$^{14}$B capture to the GS of $^{14}$B is illustrated in Figure 4.4a. The results of calculations of $E1$ and $M1$ partial cross-sections for the potentials No. 1 ($C_w$ = 1.40), and 3 ($C_w$ = 2.10) from Table 4.2 and the scattering potentials from Table 4.1 are shown in comparison with the experimental data of [13]. Figure 4.4a shows the total cross-sections in the linear energy scale up to 2.5 MeV to display the ${}^{3+5}P_1$ resonance at 305 keV.

Figure 4.4b shows a wider range from $10^{-5}$ keV to 5 MeV relevant to the reaction rate calculation (see Sec. IV). The purpose of the results presented in Figure 4.4b is to solve the question of the role of FSs in the GS potentials from Table 4.2 arranged in pairs, i.e., with or without FS at close $C_w$. The results of calculating the total cross-sections for the GS potentials with the FS No. 2 ($C_w$ = 1.42) and 4 ($C_w$ = 2.15) are shown in Figure 4.4b by the green and magenta dotted curves, respectively.

One can see their good pairwise agreement with the results for potentials without the FS. The slight variation is associated with a small difference in the values of $C_w$ and in the scattering phase shifts of the $S$ potential with the FS (No. 4 in Table 4.1) from the exact zero within 1 degree.

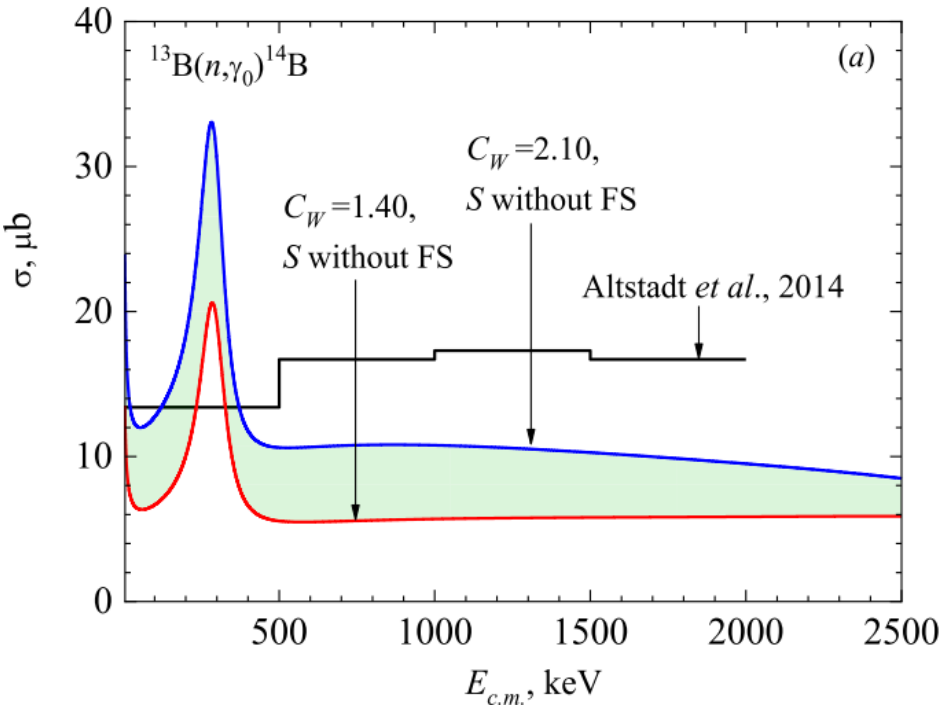


a)

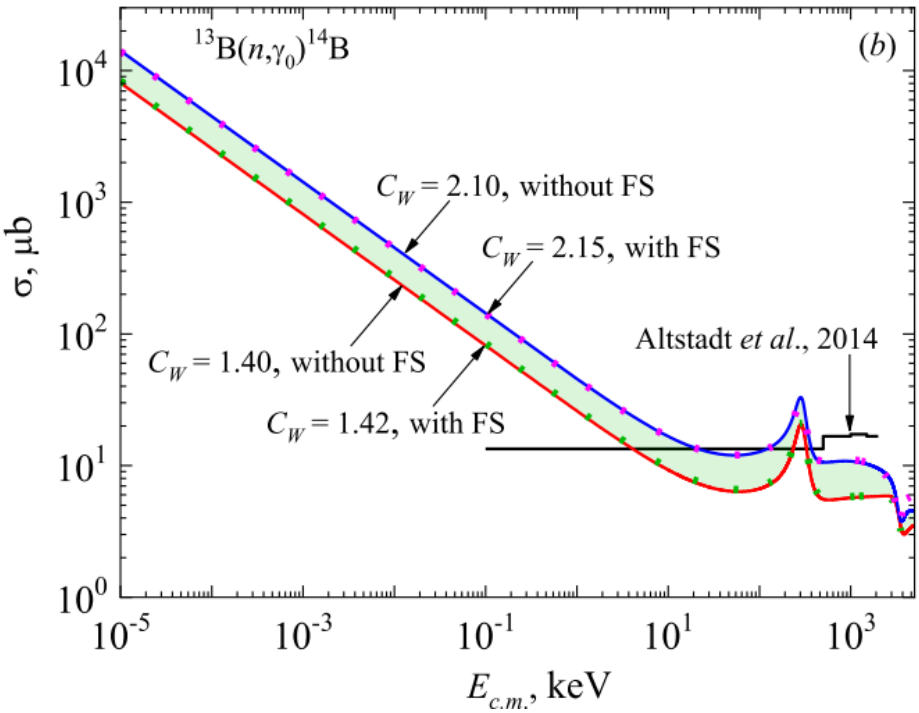


b)

The histogram is the experiment [13].
a) Total cross-sections calculated without FS: red solid curve – potential No. 1 in Table 4.2($C_w$ = 1.40), blue solid curve – potential No. 3 in Table 4.2 ($C_w$= 2.10).
b) Comparison of the total cross-sections calculated without and with FS: solid curves are the same as in Figure 4.4a, green dotted curve – potential No. 2 in Table 4.2 ($C_w$ = 1.42), magenta dotted curve – potential No. 4 in Table 4.2 ($C_w$ = 2.15).

Figure 4.4 – Total cross-sections of the $^{13}$B($n$,$\gamma_0$)$^{14}$B radiative capture to the GS of $^{14}$B with potentials from Tables 4.1 and 4.2

At an energy of $10^{-5}$ keV, the cross-section value for the GS potential without FS No. 1 is equal to 8.05 mb, and for the GS with FS No. 2 it is equal to 8.36 mb. Similar results are obtained for the second potential with an FS. Therefore, we conclude that the presence or absence of FS does not affect the calculated total cross-section. The same consistent pattern is revealed in the $(n,\gamma_1)$ capture calculations to the excited state of $^{14}$B. Further results are presented only for the potentials without FS.

To evaluate the thermal cross-sections, we use the standard approximation holds at energies from 10 meV to 1 keV

$$\sigma_{ap}(\mu\text{b}) = \frac{A}{\sqrt{E_{c.m.}(\text{keV})}}. \tag{4.8}$$

The value of the calculated cross-section $\sigma_{theor}(E)$ at $E_{\min}$ = 10 meV provides the constant $A$ = 25.46 μb·keV$^{1/2}$ for the red solid curve in Figure 4.4b ($C_w$ =1.40). Consequently, at a thermal energy of 25.3 meV, the cross-section $\sigma_{therm} = 5.1$ mb. For the blue solid curve in Figure 4.4b ($C_w$ = 2.10), the value of $A$ = 44.70 μb·keV$^{1/2}$ and $\sigma_{therm} = 8.9$ mb.

The accuracy of the approximation (4.8) is defined by the relative difference between the cross-sections $\sigma_{theor}(E)$ and $\sigma_{ap}(E)$:

$$M(E) = \left| \left[ \sigma_{ap}(E) - \sigma_{theor}(E) \right] \right| / \sigma_{theor}(E). \tag{4.9}$$

$M$(1 keV) ≈ 0.2% for both cases of $C_w$ decreases with decreasing energy.

Figure 4.5 illustrates the input of partial $E1$ and $M1$ cross-sections related to the set of amplitudes (4.1) of $(n,\gamma_0)$ process.

The $M1$ transition from the $S$ wave determines the low-energy and thermal cross-sections. The $E1$ transition amplitudes define the higher energy region. The $(n,\gamma_1)$ capture process reveals nearly the same partial structure (4.2).

Figure 4.6 illustrates the relative input of the $(n,\gamma_0)$ and $(n,\gamma_1)$ capture processes into the total cross-section. The dominance of $(n,\gamma_0)$ cross-section comparing the $(n,\gamma_1)$ within the factor ~ 1/30. Note, the example in Figure 4.6 refers to the lower $C_w$ values. The tendency is the following: the increase of $C_w$ leads to the cross-section increasing of any cross-section, but the $(n,\gamma_0)$ dominance remains within the above factor.

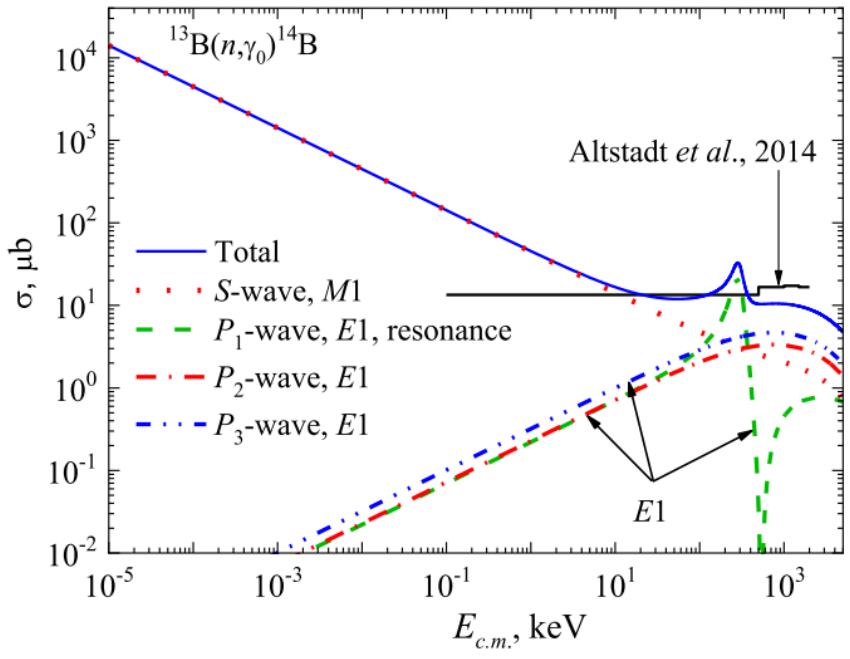


The histogram is the experiment [13].

Figure 4.5 – The partial $E1$ and $M1$ and total cross-sections of the $^{13}$B($n$,$\gamma_0$)$^{14}$B radiative capture to the GS of $^{14}$B ($C_w$ = 2.10 without FS)

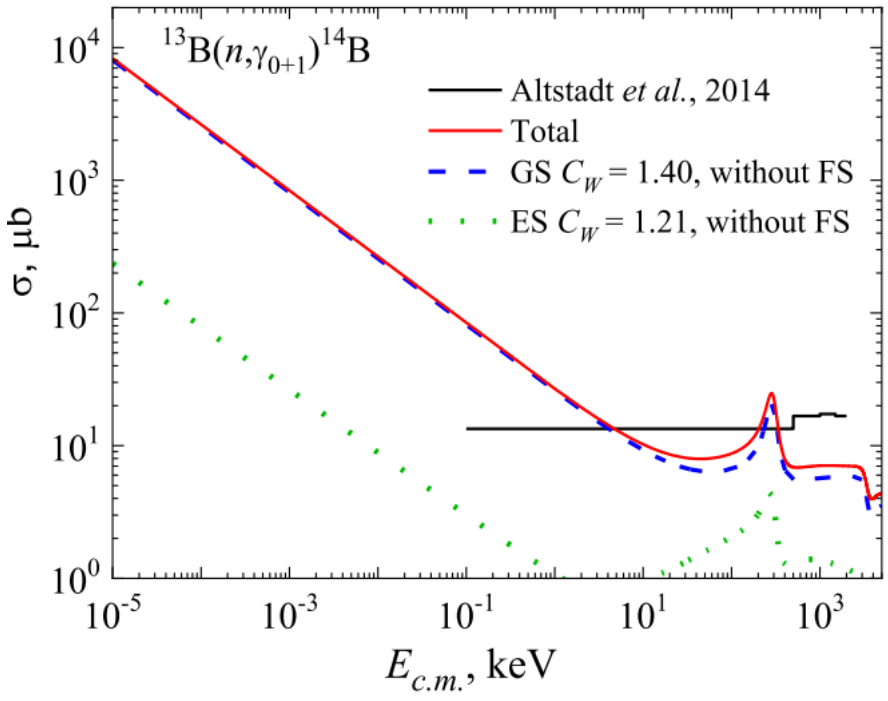


The histogram is the experiment [13].

Figure 4.6– The partial $E1$ and $M1$ and total cross-sections of the $^{13}$B($n$,$\gamma_{0+1}$)$^{14}$B radiative capture to the ground $2^-$ and excited $1^-$ states of $^{14}$B ($C_w$ = 1.40 for the GS and $C_w$ = 1.21 for the ES)

Summarizing the results on the total cross-sections in Figures 4.4–4.6, we may state that starting from $E_{c.m.} \approx 10$ keV and down to thermal energies, the cross-section increases by $10^3$ times from ~ 10 μb to ~ 5–10 mb. We assume this result is a prospective one for future experiments. At the same time, since the data are preliminary and not informative enough, the discussion of the agreement between the experiment and MPCM calculations in Figures 4.4, 4.5 and 4.6 is a little early.

### 4.5 Reaction rates of radiative neutron capture on $^{10\text{-}13}$B and $^{12\text{-}14}$C

We follow [14] while calculating the reaction rate of the radiative neutron capture. For the rate in units of $cm^3mol^{-1}sec^{-1}$, the following expression is used

$$N_A\langle\sigma v\rangle = 3.7313\cdot 10^4\,\mu^{-1/2}T_9^{-3/2}\int_0^\infty \sigma(E)E\exp(-11.605E/T_9)dE, \qquad (4.10)$$

where $N_A$ is Avogadro number, $E$ is given in MeV, the total cross-section $\sigma(E)$ is in $\mu$b, $\mu$ is the reduced mass in amu, and $T_9$ is the temperature in $10^9$ K.

### 4.6 Reaction rate of the neutron capture on $^{13}$B

In Figure 4.7a, the red and blue solid curves show the $(n,\gamma_0)$ capture reaction rates to the GS, which correspond to the results for the total cross-sections presented for the potentials without the FS in Figure 4.4b.

The band in Figure 4.7a corresponds to the band in Figure 4.4 and confines the possible reaction rate values for the range of $C_w$ discussed in previous sections.

The black solid curve in Figure 4.7a shows the reaction rate from [45] obtained by Rauscher *et al*. Figure 4.7a indicates that these results completely disregard the non-resonance part of the reaction, which leads to an increase of the cross-sections at low energies due to the $M1$ transition, as shown in Figure 4.1b or Figure 4.6.

Important remark concerns the structure of bound states: in [45] the $D$ component is assumed for both GS and ES of $^{14}$B in $n + {}^{13}$B channel, contrary to treating these states as $S$-waves. Consequently, there are no $M1$ transitions in the calculations of Rauscher et al. [45], which provide the low-temperature reaction rate. The resonance structure of the black curve in Figure 4.7 is due to the $3^-$ ($E_x$ = 1.38 MeV) resonance, the $1^+$ resonance ($E_x$ = 1.275 MeV) was not taken into account. The signature of the $1^+$ (305 keV) resonance in cross-sections in Figures 4.4–4.6 incorporated in present calculations is seen in reaction rates as a rise at temperatures $T_9 \geq 0.2$ in Figure 4.7.

Figure 4.7b illustrates the input of the $(n,\gamma_1)$ capture to the reaction rate through the example of one $C_w$ set. Since, as shown in Figure 4.6, the $(n,\gamma_1)$ capture contribution of the excited $1^-$ state is relatively small, this results in the values of the reaction rate in Figure 4.7b (red dotted curve). The same tendency is preserved for any other $C_w$ sets.

The signature of the 300 keV resonance in cross-sections in Figures 4.4–4.6 is seen in reaction rates as a rise at temperatures $T_9 \geq 0.2$ in Figure 4.7.

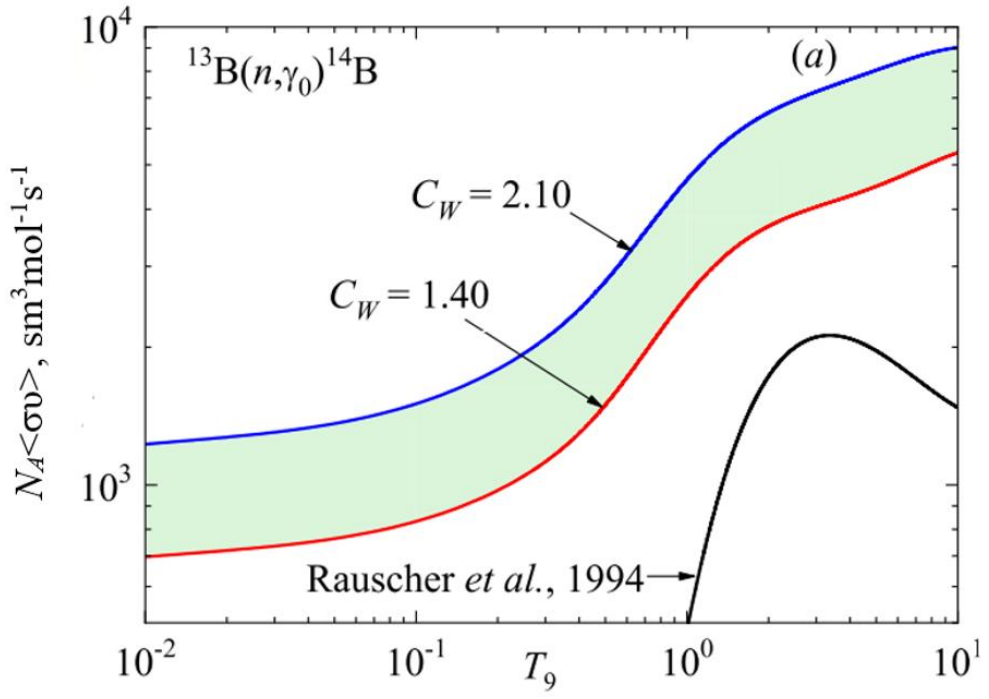


a)

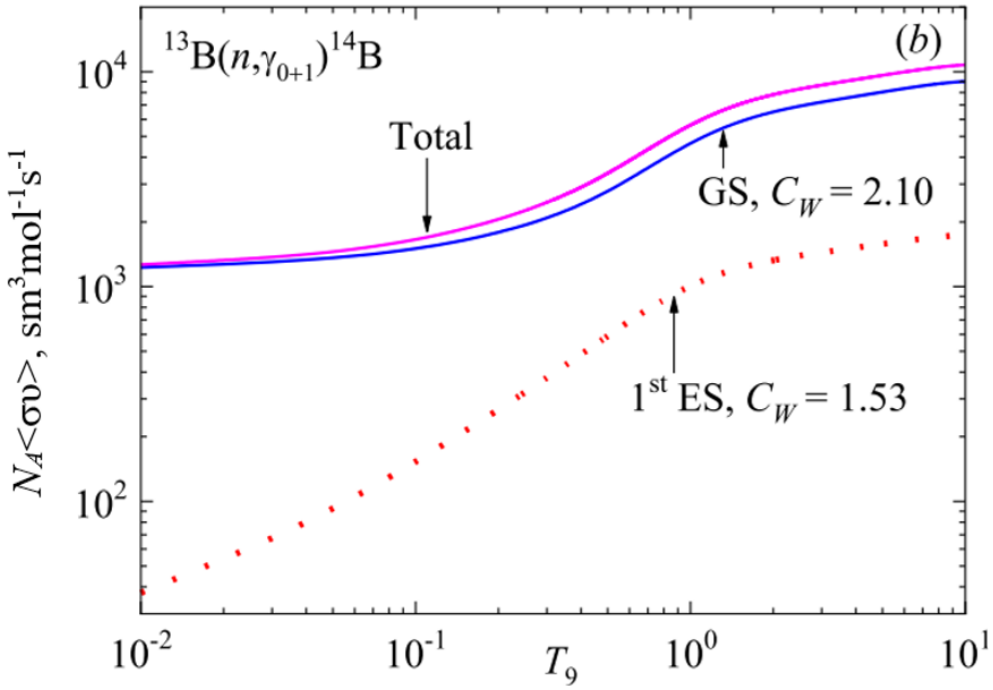


b)

a) Transitions to the GS: potential No. 1 from Table 4.2 ($C_w$ = 1.40) – red solid curve, potential No. 3 from Table 4.2 ($C_w$ = 2.10) – blue solid curve. Black solid curve shows the reaction rate obtained in [45].

b) Transitions to the ground and excited states: GS potential No. 3 from Table 4.2 ($C_w$ = 2.10) – blue solid curve; ES potential No. 3 from Table 4.3 ($C_w$ = 1.50) – red dotted curve. Magenta solid curve is the total capture reaction rate.

Figure 4.7 – Reaction rate of the radiative neutron capture on $^{13}$B calculated with potentials without FS

The reaction rates in Figure 4.7 are parameterized by an expression of the form [80]:

$$N_A\langle\sigma v\rangle = a_1 / T_9^{2/3} \exp(-a_2 / T_9^{1/3}) \times$$
$$\times(1.0 + a_3 T_9^{1/3} + a_4 T_9^{2/3} + a_5 T_9 + a_6 T_9^{4/3} + a_7 T_9^{5/3}) + \frac{a_8}{T_9} \quad (4.11)$$

The parameters $a_i$ given in Table 4.4 correspond to the reaction rates presented in Figure 4.7: the first column refers to the red solid curve in Figure 4.7a; the second column – the blue solid curve in Figure 4.7a; the third column – the red dotted curve in Figure 4.7b; the last column – magenta solid curve in Figure 4.7b.

Table 4.4 – Parameters in (4.11) for the reaction rates in Figure 4.7

| $i$ | $(n,\gamma_0)$, $C_w = 1.40$ | $(n,\gamma_0)$, $C_w = 2.10$ | $(n,\gamma_1)$, $C_w = 1.53$ | $(n,\gamma_{0+1})$, $C_w = 2.10$ and $C_w = 1.53$ |
|---|---|---|---|---|
| | $\alpha_i$ | $\alpha_i$ | $\alpha_i$ | $\alpha_i$ |
| 1 | 14381.77 | 17240.08 | 2413.837 | 19795.34 |
| 2 | 1.41717 | 1.2962 | 1.46568 | 1.31492 |
| 3 | -2.61253 | -2.52512 | -3.81023 | -2.64425 |
| 4 | 1.16178 | 0.93077 | 4.53362 | 1.25477 |
| 5 | 3.19007 | 3.74616 | 2.12766 | 3.6103 |
| 6 | -2.58617 | -2.76411 | -2.80537 | -2.77072 |
| 7 | 0.57029 | 0.57636 | 0.69249 | 0.58652 |
| 8 | 4.74344 | 7.39244 | 0.13587 | 7.62151 |
| | $\chi^2 = 0.13$ | $\chi^2 = 0.09$ | $\chi^2 = 0.12$ | $\chi^2 = 0.09$ |

## 4.7 Comparison of neutron radiative capture rates on $^{10\text{-}13}$B and $^{12\text{-}14}$C isotopes

To define the role of $^{13}$B$(n,\gamma)^{14}$B reaction in the boron chain of sequences in Figure 4.1, we are going to answer the question – either the calculated reaction rates prove the formation of $^{14}$B or $^{13}$B decays before the neutron capture may start. The short-lived isotopes may provide the *r*-processes in an explosive environment and neutron-rich matter at high densities [1]. The conventional density–temperature conditions for the *r*-process are assumed as $\overline{n}_n \sim 10^{22} - 10^{23}$ cm$^{-3}$ and $T_9 \sim 1$ [11, 141]. We examined these conditions for $^{13}$B$(n,\gamma)^{14}$B reaction based on the calculated reaction rates.

One can identify the *r*-process according to the following relation:

$$\tau_\beta \approx N_n \tau(n,\gamma), \quad (4.12)$$

where the mean lifetime of $\beta$-decay $\tau_\beta$ and neutron capture time $\tau(n,\gamma)$ are

interrelated by the number of neutrons $N_n$ must be captured before $\beta$-decay occurs [121]. The neutron capture time $\tau(n,\gamma)$ depends on the reaction rate and neutron number density $\bar{n}_n$ [76]:

$$\tau(n,\gamma) = \frac{1}{\bar{n}_n \langle \sigma_{n,\gamma} v \rangle}. \tag{4.13}$$

Note, the recommended half-live values $t_{1/2}$ [98, 142, 143] cover the range 17.10 – 17.52 ms, and following the Sargent formula $t_{1/2} = \tau_\beta \ln(2)$, the mean lifetime range is 0.0243 s < $\tau_\beta$ < 0.0253 s. Further calculations reveal minor variations within $\tau_\beta$ interval.

The $\tau(n,\gamma)$ calculation results for the $^{13}$B$(n,\gamma_{0+1})^{14}$B reaction is shown in Figure 4.8a as the insert. The dashed line corresponds to the $^{13}$B mean lifetime $\tau_\beta$ = 0.0248 s and $\bar{n}_n = 10^{23}$ cm$^{-3}$.

Arrows indicate the equality $\tau_\beta = \tau(n,\gamma)$ and reflect the equilibrium of the decay and capture processes, $N_n$ = 1. The area under the dashed line holds $\tau_\beta = \tau(n,\gamma)$, which means that the number of neutrons that interacted with $^{13}$B is $N_n$ > 1, as seen in the main field of Figure 4.8a. One may conclude that at temperatures $T_9$ on the right of the arrows, the process $(n,\gamma)$ is faster comparing the $\beta$-decay. Therefore, the ignition of $^{13}$B$(n,\gamma_{0+1})^{14}$B reaction occurs at $T_9 \geq 0.4$ in the case of the reaction rate shown by the upper curve ($C_w$ = 2.10) in Figure 4.7a, and at the $T_9 \geq 0.9$ in the case of the low red curve ($C_w$= 1.40).

Figure 4.8b illustrates the correlation between the variation of the neutron density and ignition temperature $T_9$, i.e. the higher $\bar{n}_n$ the lower $T_9$ is needed to provide the number of $(n,\gamma_0)$ capture acts $N_n$ > 1.

Figure 4.8c illustrates the same regularities, but we found a very specific feature. The point is, that Figure 4.7b shows no essential input of the $(n,\gamma_1)$ process and plays the role of reaction rate correction, but its inclusion in consideration of neutron capture time $\tau(n,\gamma_{0+1})$ leads to the noticeable shift of ignition points to the lower edge of the $T_9$ scale: $0.15T_9 \to 0.1T_9$ ($\bar{n}_n = 1.5\cdot10^{22}$ cm$^{-3}$); $0.4T_9 \to 0.3T_9$ ($\bar{n}_n = 1\cdot10^{22}$ cm$^{-3}$); $1.1T_9 \to 0.8T_9$ ($\bar{n}_n = 0.5\cdot10^{22}$) cm$^{-3}$. Therefore even a slight increase in reaction rate gives feedback to the occurrence of $^{13}$B$(n,\gamma_{0+1})^{14}$B reaction. There are no temperature constraints at a rather high neutron density $\bar{n}_n > 2\cdot10^{22}$.

The $T_9$ interval relevant for the start of *r*-production of $^{14}$B may be defined at the present stage as 0.1 < $T_9$ < 0.8 under neuron density matter conditions $0.5\cdot10^{22}$ cm$^{-3}$ < $\bar{n}_n$ < $1.5\cdot10^{22}$ cm$^{-3}$. Based on these results, we compare the reaction rates of radiative neutron capture on $^{10\text{-}13}$B and $^{12\text{-}14}$C isotopes calculated within the same MPCM model formalism and presented in Figure 4.9.

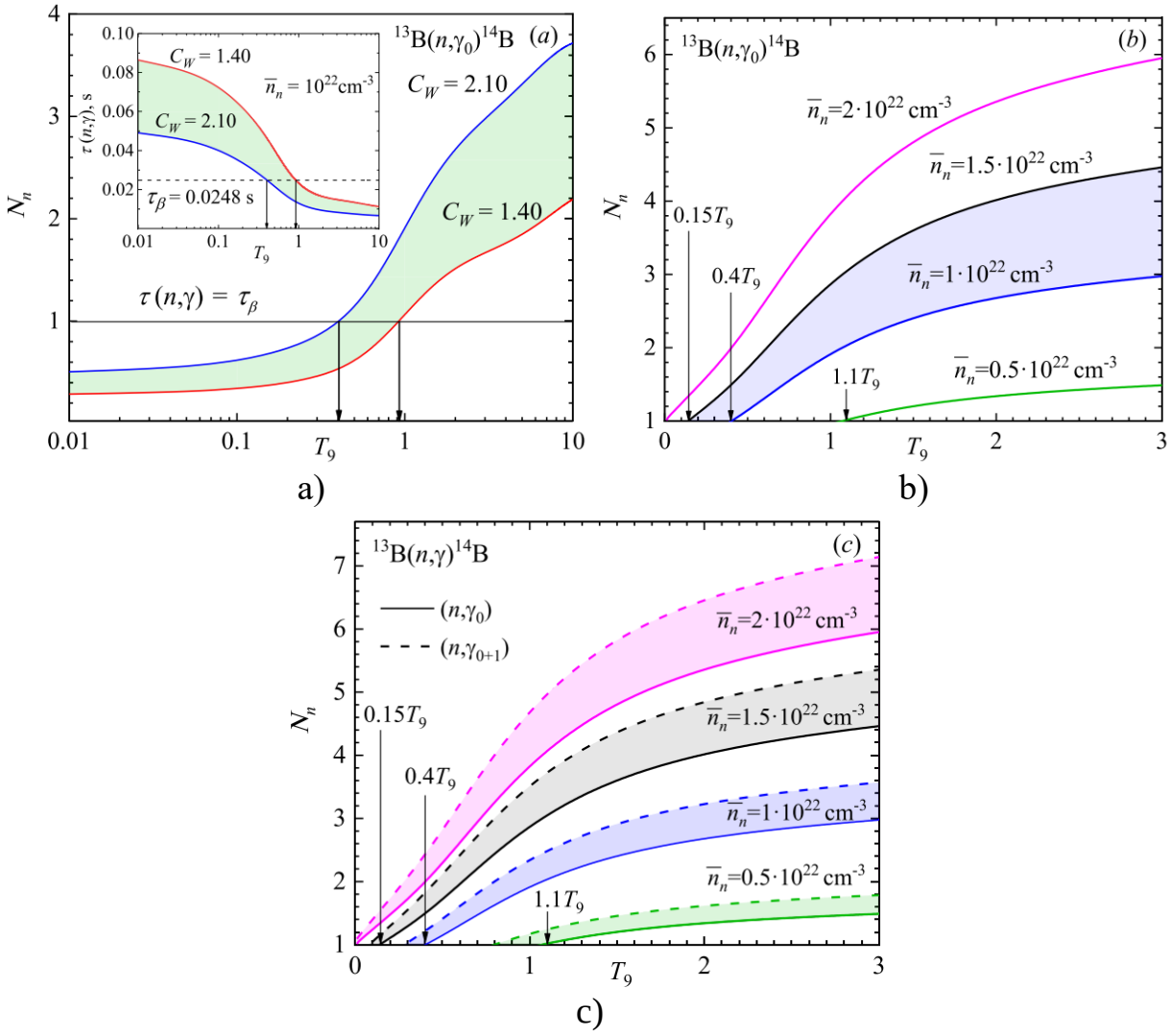


The band corresponds to the reaction rates in Figure 4.7.
a) The insert shows the neutron capture time $\tau(n,\gamma)$.
b) Illustration of the ignition $T_9$ values depending on the neutron number density $\bar{n}_n$
c) The effect of the exited state: solid curves correspond to the ($n$,$\gamma_0$) capture to the GS; dashed curves correspond to the ($n$,$\gamma_{0+1}$) total capture.

Figure 4.8 – The number of captured neutrons $N_n$ dependence on the $T_9$ conditioned by the neutron number density $\bar{n}_n \cdot (a)\bar{n}_n = 10^{22}$ cm$^{-3}$

It is quite natural that the production of isotopes with a mass number $A$ following $A$-1 provides the continuing of the neutron-induced sequence if the previous reaction rate is comparable or prevailed over the next one. This regularity for the $^{10–13}$B isotopes is observed directly at temperatures ~ 0.05 – 0.3$T_9$, which overlaps with the window for the $^{14}$B production. The gaps at low and high $T_9$ in the case of $^{11}$B($n$,$\gamma$)$^{12}$B reaction rate are not the worrying factor, as isotope $^{11}$B is stable and may be accumulated.

Compliment now the comparative boron's chain analysis by information from Table 4.5. Correlation between the threshold energies $E_{th}$ in the boron channels and reaction rates at ultra-low $T_9$ is observed, i.e., the higher $E_{th}$, the higher the reaction rate. Thermal cross-sections for odd-odd $^{10,12}$B isotopes near order larger than $\sigma_{therm}$ of the odd-even $^{11,13}$B.

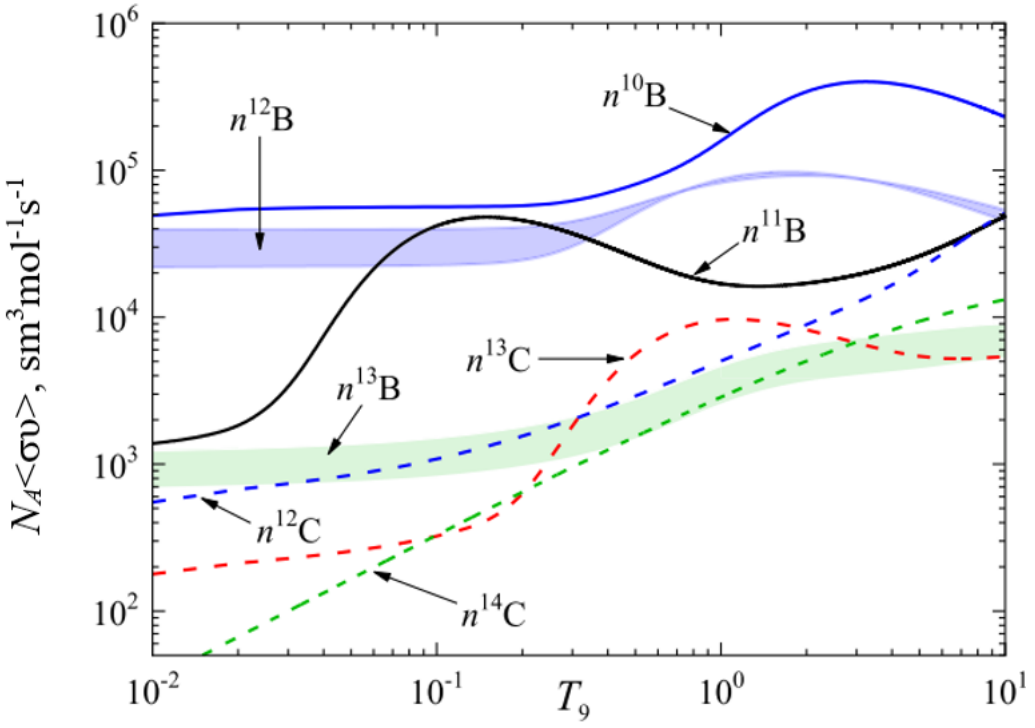


$^{10}$B($n,\gamma$)$^{11}$B – blue solid curve [78], $^{11}$B($n,\gamma$)$^{12}$B – black solid curve [88, 89], $^{12}$B($n,\gamma$)$^{13}$B – pale blue band [32], $^{13}$B($n,\gamma$)$^{14}$B – pale green band (present calculations), $^{12}$C($n,\gamma$)$^{13}$C – blue dashed curve [127], $^{13}$C($n,\gamma$)$^{14}$C – red dashed curve [128], $^{14}$C($n,\gamma$)$^{15}$C – green dashed curve (unpublished). Additional details are in Table 4.5.

Figure 4.9 – Comparison of the neutron capture reaction rates on $^{10–13}$B and $^{12–14}$C isotopes calculated in MPCM

One can observe these relationships for the reaction rates in Figure 4.9, except the temperature interval ~ 0.02 – 1$T_9$ for the $^{11}$B($n,\gamma_{0+1+2+3+4}$)$^{12}$B reaction, where the rate essentially increases due to a large number of resonances in this channel. Besides, the calculated $\sigma_{therm}$ for $^{11}$B($n,\gamma$)$^{12}$B shows excellent agreement with the measured value (see details in [88, 89]), and we interpret this result as the substantiation of obtained in the present work $\sigma_{therm}$ for $^{13}$B($n,\gamma$)$^{14}$B.

The isobar-analogue channels $^{13}$B($n,\gamma$)$^{14}$B and $^{13}$C($n,\gamma$)$^{14}$C lead to the formation of $^{14}$C either via $^{14}$B β-decay or the direct radiative neutron capture on $^{13}$C. Figure 4.9 shows that at temperatures below 0.3$T_9$ the boron channel rate exceeds the carbon one, and turns lower in the range ~ 0.3 – 3$T_9$, at $T_9$ > 3 the reaction rates in both channels become close.

Consequently, one may conclude that both processes of the $^{14}$C production show comparable efficiency.

Table 4.5 – The overview of radiative neutron capture reactions on $^{10–13}$B and $^{12–14}$C isotopes calculated in MPCM

| Reaction | Threshold energy $E_{th}$, MeV | Included bound states | Included resonances | $\sigma_{therm}$, mb | Ref. |
|---|---|---|---|---|---|
| $^{10}B(n,\gamma)^{11}B$ | 11.4541 | $(n,\gamma_{0+2+3+4+9})$ | $^{6+8}P_{5/2}$, $^{6+8}D_{5/2}$, $^{6+8}D_{7/2}$ | 405 | [78] |
| $^{11}B(n,\gamma)^{12}B$ | 3.3700 | $(n,\gamma_{0+1+2+3+4})$ | $^{3+5}P_2$, $^{3+5}D_1(\mathrm{I})$, $^{3+5}D_2$, $^{3+5}D_3$, $^{3+5}D_1(\mathrm{II})$, $^{5}F_1(\mathrm{I})$, $^{3+5}F_3(\mathrm{I})$, $^{5}F_1(\mathrm{II})$ | 10.6 | [88, 89] |
| $^{12}B(n,\gamma)^{13}B$ | 4.8780 | $(n,\gamma_0)$ | $^{4}D_{1/2}$, $^{4}D_{5/2}$, $^{4}P_{5/2}$ | 176 and 285 | [32] |
| $^{13}B(n,\gamma)^{14}B$ | 0.9700 | $(n,\gamma_{0+1})$ | $^{3+5}P_1$ | 5.1 – 8.9 | present |
| $^{12}C(n,\gamma)^{13}C$ | 4.9464 | $(n,\gamma_{0+1+2+3})$ | $^{2}D_{3/2}$ | 3.4 – 3.9 | [127] |
| $^{13}C(n,\gamma)^{14}C$ | 8.1765 | $(n,\gamma_{0+1+2})$ | $^{2}P_{1/2}$ | 1.50 | [128] |
| $^{14}C(n,\gamma)^{15}C$ | 1.2181 | $(n,\gamma_{0+1})$ | $^{2}P_{3/2}$ | $5\cdot10^{-6}$ | – |

### 4.8 Concluding remarks

The total cross sections of $^{13}B(n,\gamma_{0+1})^{14}B$ reaction are calculated in MPCM based on $E1$ and $M1$ transitions from $10^{-2}$ eV to 5 MeV. We proved strong sensitivity of the cross sections on the asymptotic constant $C_w$ provided the proper long-range dependence of radial bound $S$ wave functions, ad hoc, the larger $C_w$, the greater the absolute values of cross-sections. The role of the FS in the calculated spectrum turned out to be insignificant.

The $E1$ transitions provided the background of the cross-section due to the capture from the non-resonance $^{3+5}P_2$, $^{5}P_3$, $^{3}P_0$ waves, and the resonant $^{3+5}P_1$ wave in the initial channel reveals the resonance structure of the cross-section at ~ 300 keV. The $M1$ transition occurs via the $S$ scattering wave and contributes predominantly into the thermal cross-sections. Variation of $C_w$ = 1.4 – 2.4 gives the range of $\sigma_{therm}$ = 5.1 – 8.9 mb. These values $\sigma_{therm}$ have not been ever estimated in theory, which seems important for experimentalists.

The reaction rates of $^{13}$B($n,\gamma_{0+1}$)$^{14}$B process show the same dependence on the asymptotic constant $C_w$ and relative contributions of ($n,\gamma_0$) and ($n,\gamma_1$) channels. The results of MPCM calculations differ cardinally from those of Rauscher *et al*. [45] in the whole $T_9$ range. Therefore we conclude that the present data on the reaction rates substantiate the role of $^{13}$B($n,\gamma_{0+1}$)$^{14}$B reaction in the Boron-Carbon-Nitrogen chains, i.e., this is not the break-point of the Boron sequence.

To support the conclusion, we estimated the relationship between the mean lifetime of $^{13}$B β decay $\tau_\beta$ and neutron capture time $\tau(n,\gamma)$. The temperature window for the ignition of $^{14}$B *r*-production 0.1 – 0.8$T_9$ related to the neutron densities $\overline{n}_n$ = 5 $10^{21}$ – 1.5 $10^{22}$ cm$^{-3}$ is determined, while $\overline{n}_n$ > 1.5 $10^{22}$ cm$^{-3}$ there are no temperature limits. We demonstrated that the preferences for $^{13}$B($n,\gamma_{0+1}$)$^{14}$B reaction directly depend on the reaction rate values, the larger $\langle\sigma_{n,\gamma}v\rangle$, the shorter the neutron capture time $\tau(n,\gamma)$.

We foresee the following factors may increase the reaction rate: inclusion of the *D*-component into the bound ground state (its weight is estimated today at ~ 17%) may enhance the input of the $1^+$ resonance to *E*1 capture cross-section at 305 keV. The role of the transitions denoted in Figure 4.2, but not considered in the present study, might be evaluated, as the example of inclusion rather weak ($n,\gamma_1$) process leads to the narrowing of the ignition temperature interval. Another problem concerns the determination of $3^\pi$ level parity at $E_x$ = 4.06 MeV. If $\pi = +1$, the additional *E*1 transition may occur. In case $\pi = -1$, *E*2 transition may reveal interference effects with $3^-$ state at $E_x$ = 1.38 MeV.

The unique experimental results on the Coulomb dissociation of $^{14}$B [13], converted into the cross-section of $^{13}$B($n,\gamma$)$^{14}$B reaction, remain preliminary and not completed with estimated uncertainties.

The results for the reaction rate of $^{13}$B($n,\gamma_{0+1}$)$^{14}$B may change the point of view on its minor impact on the heavy elements production expressed in [126] was assumed. The present calculations are predictive and estimative for substantiation of the performing the new experiments of the neutron capture on $^{13}$B and give the model estimation of the reaction rate of synthesis of $^{14}$B isotope in the $n^{13}$B channel for the first time.

## 5 REVISION OF $^{15}N(p,\gamma)^{16}O$ REACTION IN MPCM

### 5.1 The role of $^{15}N(p,\gamma)^{16}O$ reaction in CNO bi-cycle

Stellar burning depends on the star's initial mass and can proceed either through the *p–p* chain or through the CNO cycle, fusing hydrogen to helium through a chain fusion processes, - sequence of thermonuclear reactions that provides most of the energy radiated by the hot stars [124, 144, 145]. Unlike the *p–p* chain, the CNO cycle is the catalytic one, that converts 4 protons into one helium nucleus but does so via reactions on the pre-existent seed isotopes of carbon, nitrogen, and oxygen nuclei. The carbon, nitrogen, and oxygen isotopes act just as catalysts in the CNO cycle. The CNO bi-cycle involves the following chains of nuclear rections:

$$^{12}C(p,\gamma)^{13}N(\beta^{+}\upsilon)^{13}C(p,\gamma)^{14}N(p,\gamma)^{15}O(\beta^{+}\upsilon)^{15}N \rightarrow {}^{15}N(p,\alpha)^{12}C$$
$$\rightarrow {}^{15}N(p,\gamma)^{16}O(p,\gamma)^{17}F(\beta^{+}\upsilon)^{17}O(p,\alpha)^{14}N \qquad (5.1)$$

Therefore, the CNO bi-cycle produces three electron neutrinos from beta decays of $^{13}N$, $^{15}O$, and $^{17}F$ and is also referred to as the "cold" CNO cycle [146]. The CN cycle contains no stable $^{13}N$ and $^{15}O$ isotopes of nitrogen and oxygen, that decay to the stable isotopes $^{13}C$ and $^{15}N$, respectively. The catalytic nuclei are lost from the process via the leak reaction $^{15}N(p,\gamma)^{16}O$ and the subsequent reactions in (1) restore the catalytic material, generating $^{16}O$ and heavier isotopes leading to the accumulation of the $^{4}He$ and $^{14}N$ nuclei. This second branch produces $^{17}F$, which decays beta with the emission of the 1.74 MeV electron neutrinos. Thus, the $^{15}N(p,\gamma)^{16}O$ process represents a breakout reaction linking the alternative NO channel of the CNO cycle that produces the stable oxygen isotopes [147]. Therefore, in the CNO cycle, the proton capture reaction on $^{15}N$ allows two possible channels: the branch of the cycle $^{15}N(p,^{4}He)^{12}C$ and the branch of the cycle $^{15}N(p,\gamma)^{16}O$, reactions and they intersect at the $^{15}N$ nucleus.

The rate of the CN with respect to the NO cycle depends on the branching ratio of the $^{15}N(p,\gamma)^{16}O$ and $^{15}N(p,\alpha)^{12}C$ reaction cross sections. The probability for the $^{15}N(p,\gamma)^{16}O$ process to occur is about one for every thousand of the second [148], thus the contribution to the overall nuclear energy production is negligible, while the consequences on the nucleosynthesis are critical [149]. Therefore, in the case of an active NO cycle, the correct evaluation of the $^{15}N(p,\gamma)^{16}O$ reaction is crucial to properly predict the abundances of all the stable $^{16}O$, $^{17}O$, and $^{18}O$ isotopes and their relative ratios [80, 150, 151]. The reaction rates ratio determines on how much nucleosynthesis of $^{16}O$, $^{17}O$, and $^{18}O$ takes place during CNO burning [150].

Since the first experimental study of $^{15}N(p,\gamma)^{16}O$ reaction in 1952 [152] experimental data [148, 153-158] for total sections of the radiative $p^{15}N$ capture in the energy region from 80 keV to 2.5 MeV were collected [39, 159]. Analysis of exciting experimental measurements of the low-energy $^{15}N(p,\gamma)^{16}O$ reaction shows that cross-section data differ substantially at lower energies.

In the past, a variety of theoretical approaches from potential cluster models to multilevel *R*−matrix formalisms [147, 157, 160-163] were used to describe the $^{15}N(p,\gamma)^{16}O$ reaction cross-section at the stellar energies and astrophysical *S*-factor that is the main characteristic of this process at low energies. In the framework of the

selective resonant tunneling model [164] $^{15}$N($p$,$\gamma$)$^{16}$O cross-section and $S$-factor have been studied [165]. Most recently, the astrophysical $S$-factor for the radiative proton capture process on the $^{15}$N nucleus at stellar energies are studied within the framework of the cluster effective field theory [166, 167]. The authors perform the single channel calculations where only the first resonance was considered [166] and then reported the results by including two low-energy resonances [167].

In this part we are continuing the study of the reactions of radiative capture of protons on light atomic nuclei [118, 168] and consider the radiative proton capture on $^{15}$N at astrophysical energies in the framework of a MPCM. Within the MPCM over thirty reactions of radiative capture of protons, neutrons and other charged particles on light atomic nuclei were considered. The [118, 168] provide the basic theoretical framework of the MPCM approach for the description of a charged particle induced radiative capture reactions. Calculation methods based on the MPCM of light nuclei with FS are used [24]. The presence of ASs and FS are determined based on the classification of the orbital states of clusters according to Young diagrams [25]. In this approach, the potentials of intercluster interactions for scattering processes are constructed based on the reproduction of elastic scattering phase shifts, taking into account their resonance behavior or the spectra of the levels of the final nucleus. For the bound states or ground state of nuclei in cluster channels, intercluster potentials are built based on a description of the binding energy and some of the basic characteristics of such states, e.g. asymptotic constant and mean square radius [118, 168].

In this work a radiative $p^{15}$N capture on the ground state of $^{16}$O within the framework the MPCM was considered. The model has no fitting parameters and allows to describe experimental data. We analytically and explicitly show the origin of the interference for $E1$ transitions.

The first time the contribution of $^3P_1$ scattering wave in $p$+$^{15}$N channel due to $^3P_1 \to {}^3P_0$ $M1$ transition is considered. The approach allows to analyze the explicit contribution of each transition into the $S$-factor. Within the same model, we calculate and compare rates for radiative proton capture reactions for the CNO cycle on nitrogen isotopes and present a stellar temperature dependence on the Gamow energy.

### 5.2 Interaction potentials and structure of resonance states

The $E1$ transitions from resonant $^3S_1-$scattering states are the main contributions to the total cross-section of the radiative proton capture on $^{15}$N to the ground state of $^{16}$O [147]. In the channel of $p$+$^{15}$N in continuum there are two $^3S_1$ resonances:

1. The first resonance is at an energy of 335(4) keV with a width of 110(4) keV in the laboratory frame and has a quantum numbers $J^\pi, T = 1^-, 0$ (see Table 16.22 in [169]). The latter can be due to the triplet $^3S_1$ scattering state and leads to $E1$ transition to the GS. This resonance is at an energy of 312(2) keV with a width of 91(6) keV in the center-of-mass (c.m.) frame and corresponds to the resonant state of the $^{16}$O at an excitation energy of $E_x$=12.440(2) MeV (see Table 16.13 in [169]). However, in the new database [98], for this resonance, the excitation energy of $E_x$=12.445(2) MeV and the width of $\Gamma$=101(10) keV in the c.m. are reported.

2. The second resonance is at an energy of 1028(10) keV with a width of 140(10) keV in laboratory frame and has a quantum numbers $J^{\pi}=1^{+}$ and $T = 1$ [169]. This is also due to the triplet $^3S_1$ scattering and leads to $E1$ transition to the GS of $^{16}$O. The resonance emerges at an energy of 962(2) keV with a width of Γ=139(2) keV in the c.m. and corresponds to the excitation energy of $E_x$=13.090(2) MeV of $^{16}$O in a new database [98]. In the database [169] for this resonance, the excitation energy of $E_x$=13.090(8) MeV and width of Γ=130(5) keV in the c.m. are reported. The compilation of experimental data on the $^3S_1$ resonances is presented in Table 5.1.

Table 5.1 – Data on the $^3S_1$ resonance states in $p$+$^{15}$N channel. $E_x$ is the excitation energy, $E_{res}$ and $\Gamma_{res}$ are the experimental resonance energy and the width, respectively. $E_{th}$ and $\Gamma_{th}$ are the resonance energy and the width, respectively, obtained in the present calculations

| $^{2S+1}L_J$ | $E_x$, MeV | $E_{res}$, keV | $\Gamma_{res}$, keV | $E_{th}$, keV | $\Gamma_{th}$, keV |
|---|---|---|---|---|---|
| $^3S_1$ (312) | 12.440(2) [169]<br>12.445(2) [98] | 312(2) [169]<br>317(2) [98] | 91(6) [169]<br>101.5(10) [98] | 312 | 125-141 |
| $^3S_1$ (962) | 13.090(8) [169]<br>13.090(2) [98] | 962(8) [169]<br>962(2) [98] | 130(5) [169]<br>139(2) [98] | 962 | 131 |

In databases [98, 169] are reported the other resonances as well. The third resonance has an energy of 1640(3) keV with a width of 68(3) keV in the laboratory frame and quantum numbers $J^{\pi},T=1^{+},0$. This resonance can be due to the triplet $^3P_1$ scattering and leads to $M1$ transition to the GS. The resonance is at an energy of 1536(3) keV with a width of 64(3) keV in the c.m. that corresponds to the excitation energy 13.664(3) MeV of the $^{16}$O [169] and in [98] reported the excitation energy of 13.665(3) MeV and the width of 72(6) keV in the c.m. However, this resonance was observed only in measurements [154], and in the later measurements [157, 158] the resonance is absent. Therefore, it is not considered it in present calculations. The next resonance is excited at the energy of 16.20(90) MeV ($J^{\pi},T=1^{-},0$) has a larger width of 580(60) keV in the c.m. and its contribution to the reaction rate will be small. In addition, in the spectra of $^{16}$O [169], another resonance is observed at an excitation energy of 16.209(2) MeV $(J^{\pi},T=1^{+},1)$ with a width of 19(3) keV in the c.m. However, the resonance energy is too large and its width too small to make a noticeable contribution to the reaction rates.

The cascade transitions via two very narrow $2^-$ resonances as well as the $0^-$ and $3^-$ resonances in the $0.40 \lesssim E_R \lesssim 1.14$ MeV range [170, 171] are considered for the reaction rate calculations. These cascading transitions are included in the NACRE II [159] reaction rate calculations and appear at high $T_9$. There are two $2^-$ resonances [158], at the excitation energies of 12.53 and 12.9686 MeV with the widths of 97(10) eV and 1.34(4) keV respectively. When one considers transitions only to the ground state with $0^+$, only $M2$ transitions are possible here, which have a very small cross-section, and we do not consider them.

In addition, due to such small widths, their contribution to the reaction rate will be very small. The new measurement of the excitation functions of the three dominant

cascade transitions allows for estimates of the contributions from these transitions. In [147] capture processes to the GS and three excited states $E_x$ = 6.049 MeV, 6.130 and 7.117 MeV are considered, that gives $S(0)$ = 41(3) keV·b in total while 40(3) keV·b for the GS. It is shown that the $1^-$ and two $2^+$ resonances do not affect the value of the $S$-factor, two $3^-$ resonances at $E_x$ =13.142 and 13.265 MeV decay into the GS due to the $E3$ transition and their contribution is negligible [147].

On the background of strong $E1$ transitions the next one in the long-wave expansion of the electromagnetic Hamiltonian is magnetic dipole $M1$ transition. In the case of $^{15}$N($p$,$\gamma$)$^{16}$O, $M1$ transition is allowed by selection rules. It occurs as a direct capture as a direct capture from the non-resonance scattering wave $^3P_1$ to the $^{16}$O $^3P_0$ state. The intensity of the $M1$partial transition depends on the distorted $^3P_1$ wave only and is related to the corresponding interaction potential. The estimations of the $M1$ partial cross section in plane-wave approximation shows near order of magnitude suppression.

The inclusion of the $p$ – wave interaction in $p$+$^{15}$N channel enhances the $M1$ transition. The interaction potential could be constructed based on an elastic $^{15}$N($p$, $p$)$^{15}$N scattering to describe the $^3P_1$ phase shift. The phase shifts should satisfy the following conditions:

i. at $E$ = 0 the $\sigma$ according to the generalized Levinson theorem [24];

ii. fit the existing $p$-wave $^{15}$N($p$,$p$)$^{15}$N scattering data.

iii. have a non-resonance behaviour. Below we found potential parameters that provides a reasonable phase shifts. Therefore, in calculations we are considering only the above two $^3S_1$ resonance transitions and non-resonance $^3P_1$ scattering for the $M1$ transition to the $^{16}$O GS.

We should distinguish $M1$ capture from the non-resonance $^3P_1$ scattering wave to the $^{16}$O $^3P_0$ state and $M1$ de-excitation of $1^+$ level at 13.665 MeVto the ground state. As pointed by deBoer *et al.* [147]: “The $1^+$ level at $E_x$=13.66 MeV could decay by $M1$ de-excitation to the ground state but no evidence for this is observed (contrary to [154])”. As mentioned above we are not considering the contribution of $M1$ de-excitation ($1^+$ level at 13.665 MeV) to the $S(E)$.

Construction of the potentials that give the energies and widths of $^3S_1$(312) and $^3S_1$(962) resonances reported in the literature is a challenging task. One has to find the optimal parameters of the potentials for the description of $E1$ transitions that lead to the fitting of the experimental resonance energies and the widths of both interfering resonances. For the $^3S_1$(312) resonance the found optimal parameters of the interaction

Potential that allows to reproduce the resonance energy $E_{res}$=961(1) keV and width Γ=131 keV are reported in Table 5.2. The situation is more complicated with the $^3S_1$(312) resonance. While it is possible to reproduce rather accurately the position and width of the $^3S_1$(312) resonance, the consideration of the interference of $^3S_1$ resonances gives different sets of optimal parameters for the potential. We found three sets I-III of the optimal values for $V_0$ and $\alpha$ parameters reproducing exactly the energy of the first resonance $E_{theory}$=312(1) keV, but the width $\Gamma_{theory}$ varies in the range of 125-141 keV.

Table 5.2 – Parameters of interaction potentials $V_0$ in MeV and $\alpha$ in fm$^{-2}$ for the GS and continuum states. The $C_w$ is a dimensionless constant. The theoretical widths, $\Gamma_{th}$ in keV, for the resonance $^3S_1(312)$ and $^3S_1(962)$ are calculated using the corresponding parameters of the potentials

| | $^3P_0$, GS | | | $^3S_1$ (312), $E1$ | | | $^3S_1$ (962), $E1$ | | | $^3P_1$, $M1$ | |
|---|---|---|---|---|---|---|---|---|---|---|---|
| Set | $V_0$ | $\alpha$ | $C_w$ | $V_0$ | $\alpha$ | $\Gamma_{th}$ | $V_0$ | $\alpha$ | $\Gamma_{th}$ | $V_0$ | $\alpha$ |
| I | 976.85193 | 1.1 | 2.05 | 1.0193 | 0.0028 | 141 | | | | | |
| II | 1057.9947 | 1.2 | 1.94 | 1.0552 | 0.0029 | 131 | 105.0675 | 1.0 | 131 | 14.4 | 0.025 |
| III | 1179.3299 | 1.3 | 1.8 | 1.0902 | 0.003 | 125 | | | | | |

Therefore, in calculations we are considering only the above two $^3S_1$ resonance transitions and non-resonance $^3P_1$ scattering for the $M1$ transition to the $^{16}$O GS. Let us notice that the multiple channel analysis of ground-state-cascade transitions for the $^{15}$N($p$,$\gamma$)$^{16}$O reaction demonstrated that the contribution of the transition to the ground state dominates in the astrophysical $S(0)$ factor.

For calculations of the total radiative capture cross-sections, the nuclear part of the $p^{15}$N interaction potential is contracted using Gaussian form in Eq. 2.2 [118, 168]. For description of the $^3S_1$ scattering states we use the corresponding experimental energies and widths from Table 5.1. Construction of the potentials that give the energies and widths of $^3S_1(312)$ and $^3S_1(962)$ resonances reported in the literature is a challenging task. One has to find the optimal parameters of the potentials for the description of $E1$ transitions that lead to the fitting of the experimental resonance energies and the widths of both interfering resonances.

For the second $^3S_1$ (962) resonance the found optimal parameters of the interaction potential that allow to reproduce the resonance energy $E_{res}$ = 962(1) keV and width $\Gamma_{res}$ = 131 keV are reported in Table 5.2. The situation is more complicated with the first $^3S_1$ (312) resonance. While it is possible to reproduce rather accurately the position and the width of the $^3S_1$ (312) resonance, the consideration of the interference of $^3S_1$ resonances give different sets of optimal parameters for the potential. We found three sets I − III of the optimal values for $V_0$ and $\alpha$ parameters reproducing exactly the energy of the first resonance $E_{theory}$ = 312(1) keV, but the width $\Gamma_{theory}$ is varying in the range 125-141 keV.

The dependence of the elastic $p^{15}$N scattering phases shifts for the $E1$ transitions on the energy is shown in Figure 5.1a. The result of the calculation of the $^3S_1$ phase shift with the parameters for the $S$ scattering potential without FS from Table 5.2 leads to the value of 90(1) at the energies 312(1) and 962(1) keV, respectively. In the case of the $^3S_1$ phase shift providing the first resonance, the calculations with sets I − III show very close energy dependence in the whole energy range up to 5 MeV at a fixed resonance position.

In elastic $p^{15}$N scattering spectra at energies up to 5 MeV, there are no resonance levels with $J^\pi, T = 0^+, 1^+, 2$ except for the mentioned above, and widths greater than 10 keV [169]. Therefore, for potentials of non-resonance $^3P$–waves with one bound FS parameters can be determined based on the assumption that in the energy region under consideration their phase shifts are practically zero or have a gradually declining character [118]. For such potential the optimal parameters are: $V_p$=14.4 MeV, $\alpha_p$=0.025

fm$^{-2}$. The result of calculation of $P$-phase shift with such a potential at an energy of up to 5 MeV is shown in Figure 5.1a. To determine the values of phase shifts at zero energy, we use the generalized Levinson theorem, so the phase shifts of the potential with one bound FS should begin from 180°. In the energy region $E_{c.m.} < 5$ MeV the $^3P_1$ phase shift has very weak energy dependence and it is almost constant up to $E_{c.m.} < 2.2$ MeV.

It is interesting to compare experimentally determined phase shifts with the calculations. While in [172] the elastic scattering of protons from $^{15}$N was studied and authors measured the excitation functions of $^{15}$N($p,p$)$^{15}$N over the proton energy range from 0.6 to 1.8 MeV at some laboratory angles, there been no phase shifts reported. There has been no systematic experimentally determined phase shifts at the energies of the astrophysical interest.

Absolute differential cross sections were measured for the reactions $^{15}$N($p,p$)$^{15}$N [173] and spins and parities are discussed where resonances suggest the existence of excited states in $^{16}$O. In [174] authors carried out a phase-shift analysis of cross-section for the energy interval 8−15 MeV. Angular distributions of cross section and analyzing power for elastic scattering of protons from $^{15}$N have been measured for the energy interval 2.7−7 MeV [175], and the authors gave a phase-shift analysis of data. Results of calculations for the $^3P_1$ phase shift along with the experimental data [175] are presented in Figure 5.1a.

The main assumption in all previous studies of the reaction $^{15}$N($p,\gamma$)$^{16}$O was that a direct and resonant radiative capture cross sections and their interferences contribute to the total cross-section. The direct radiative capture process is considered assuming a potential peripheral radiative capture for a hard sphere scattering [154, 176-179]. However, in general, phase shifts are extracted from experimental data analysis without the separation on the potential and resonant terms [14]. We follow this Ansatz.

Consequently, the $E1$ transition amplitudes are constructed based on a single radial scattering wave function resembling continuous, both smooth and resonance energy dependence. Both $^3S_1$ phase shifts obtained with these scattering wave functions depend on the energy as shown in Figure 5.1a. Therefore, we have only the interference between two partial $E1$ matrix elements in contrast to all previous considerations.

The resonant phase is given by the usual expression [14, 154]:

$$\delta_R = arg\tan\frac{\Gamma}{2(E - E_{res})} \tag{5.3}$$

where Γ is the width of a resonance. In Figure 5.1b is presented the energy dependence of the resonant phases $\delta_{R1}$ and $\delta_{R2}$ for the resonance width 312 keV and 962 keV, respectively.

The comparison of the phase shifts for the $E1$ transitions via the $^3S_1(312)$ and $^3S_1(962)$ resonances with the resonant phase shifts $\delta_{R1}$ and $\delta_{R2}$ shows their different energy dependence.

We construct the potential for $^{16}$O in GS with $J^{\pi},T=0^{+},0$ in $p^{15}$N-channel based on the following characteristics: the binding energy of 12.1276 MeV, the experimental values of 2.710(15) fm and 2.612(9) fm [169] for the root mean square radii of $^{16}$O and $^{15}$N of [131], respectively, and a charge and matter radius of a proton 0.8414 fm [180]. The potential also should reproduce the AC. The corresponding potential includes the FS and refers to the $^3P_0$ state.

Usually for a proton radiative capture reaction of astrophysical interest one assumes that it is peripheral, occurring at the surface of the nucleus. If the nuclear process is purely peripheral, then the final bound-state wave function can be replaced by its asymptotic form, so the capture occurs through the tail of the nuclear overlap function in the corresponding two-body channel.

The shape of this tail is determined by the Coulomb interaction and is proportional to the asymptotic normalization coefficient. The role of the ANC in nuclear astrophysics was first discussed in [67] and in [181]. These works paved the way for using the ANC approach as an indirect technique in nuclear astrophysics. See [178, 182-188] and citation herein and the most recent review [131].

We construct a potential with the FS $^3P_0$ state using the experimental ANC given in [161] that relates to the asymptotic of radial wave function as $\chi_L(R)=CW_{-\eta L+1/2}(2k_0R)$.The dimensional constant $C$ is linked with the ANC via the spectroscopic factor $S_F$. In calculations the dimensionless constant $C_w$ was exploited [189], which is defined in [118] as, $C_w=C/\sqrt{2k_0}$ where $k_0$ is wave number related to the binding energy. In [161] the values 192(26) fm$^{-1}$ and 2.1 were reported for the ANC and spectroscopic factor, respectively. In [163] the dimensional ANC includes the antisymmetrization factor $N$ into the radial overlap function as it was clarified by authors in [187].

The factor $N$ is defined $N=\left(\frac{A}{x}\right)^{1/2}=\sqrt{\frac{A!}{(A-x)!x!}}$, where $x$ and $A$ are the atomic numbers of the constituent nucleus from $x$ and $A-x$ nucleons, respectively. If $x$=1, then $N=\sqrt{A}$ and for the reaction $^{15}$N($p,\gamma_0$)$^{16}$O $N$=4. Thus, using the experimental square of the ANC 192 ± 26 fm$^{-1}$ [161, 163], we obtained the interval for the dimensionless AC used in calculations: $C_w$ =1.82 - 2.09 that corresponds to the ANC of 12.88 – 14.76 fm$^{-1/2}$. In the present calculations, we use for the proton mass $m_p$= 1.00727646677 amu [180], $^{15}$N mass = 15.000108 amu [190].

The $^{15}$N($p,\gamma$)$^{16}$O is the astrophysical radiative capture process, in which the role of ANC is elucidated [179]. In Table 5.2 three sets of parameters for the $^3P_0$ GS potential and AC $C_w$ are listed. The asymptotic constant $C_w$ is calculated over averaging at the interval 5-10 fm. Each set leads to the binding energy of 12. 12760 MeV, the root mean square charge radius of 2.54 fm and the matter radius of 2.58 fm, but the sets of $C_w$ lead to the different widths of the $^3S_1$(312) resonance.

Note, that there is one important benchmark for the choice of optimal sets for the parameters of interaction potentials for the first $E1$(312) resonance. There are the experimental values of the total cross section $\sigma_{exp}$(312)=6.0 ± 0.6 $\mu$b [148] and 6.5±

0.6 $\mu$b [157], which are in excellent agreement with earlier data 6.3 $\mu$b [155] and 6.5± 0.7 $\mu$b [153]. Simultaneous variation of $C_w$ for the GS and parameters $V_0$ and $\alpha$ for the $^3S_1(312)$ was implemented to keep the value of the cross section.

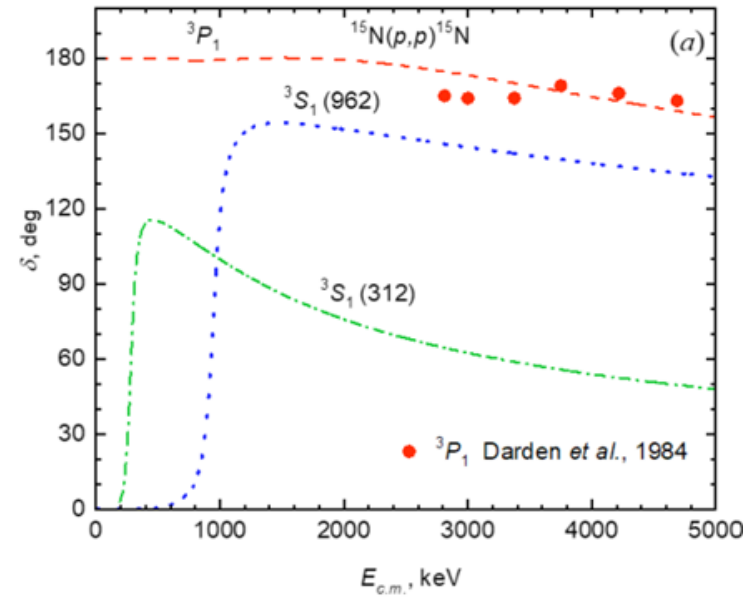


a)

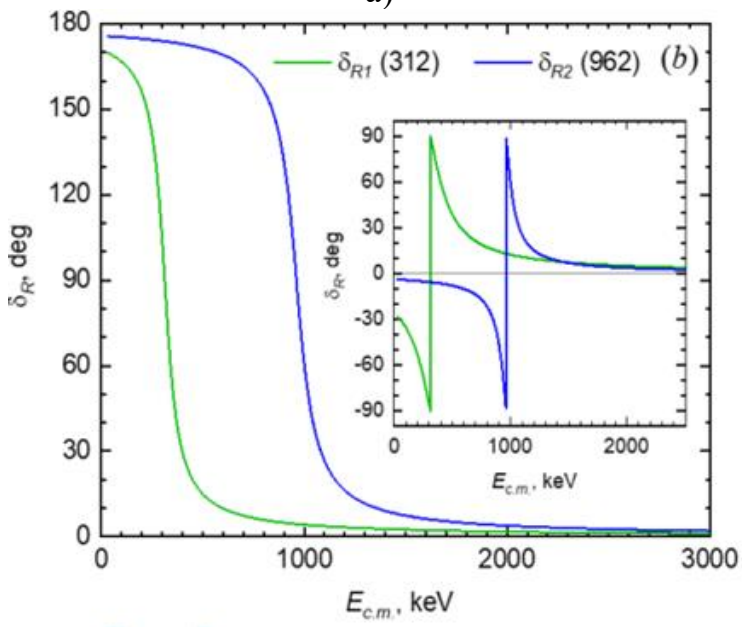


b)

a) The phase shift for $^3S_1(312)$ resonance is calculated using the set I and is shown by the dash-dotted curve. The phase shifts for $^3S_1(962)$ resonance and $^3P_1$ are presented by the dotted and dashed curves, respectively. The experimental data from [175].
b) The energy dependence of the resonant phase shifts $\delta_{R1}$ and $\delta_{R2}$ calculated using the experimental resonance widths 91 keV and 130 keV, respectively. Reconstructed scattering resonant phase shifts $\delta_{R1}$ and $\delta_{R2}$ are calculated using Eq. (5.3) and considering the tangent function periodicity.

Figure 5.1 – The dependence of the elastic $p^{15}N$ scattering phase shifts on the energy

Table 5.2 summarizes the potential parameters used in the case where the MPCM works reasonably well for a radiative proton capture in the $^{15}$N($p$,$\gamma$)$^{16}$O reaction. We sum up the procedure and choice of potential parameters as:

1. we construct the nucleon-nuclei potentials that give the channel binding energy with the requested accuracy $10^{-5}$ MeV. There are a few such potentials;

2. the experimental ANC is used as a criterion for the choice of the potential that provides the required asymptotic behavior of the radial wave function at the fixed binding energy. Thus, the variety of wave function is constrained within the upper and lower limits for the ANC: 12.88 - 14.76 fm$^{-1/2}$ for $^{15}$N($p$,$\gamma$)$^{16}$O;

3. an additional test of the wave functions is a reproduction of the matter and charge radii with a precision of ~ 5% and the $\sigma_{exp}$(312) cross section within experimental uncertainties;

4. for the continuous spectrum the parameters of the potential are fixed by the resonance energy and width above threshold. An additional source of the *S*-factor uncertainty relates to uncertainties of the resonance energy and width;

5. this procedure gives the model's uncertainty bands for the *S*-factor.

### 5.3 Astrophysical *S*−factor

The astrophysical *S*-factor is the main characteristic of any thermonuclear reaction at low energies. The present analysis focuses primarily on extrapolating the low-energy *S*-factor of the reaction $^{15}$N($p$,$\gamma$)$^{16}$O into the stellar energy range. Since the first experimental study of $^{15}$N($p$,$\gamma$)$^{16}$O reaction in 1960 [153], experimental data [148, 154, 157-159] for total sections of the radiative $p^{15}$N capture in the energy region from 80 keV to 2.5 MeV have been collected. These experimental studies verified and confirmed that the radiative $p^{15}$N capture is dominated by the first two interfering resonances at 312 keV and 962 keV with the quantum numbers $J^{\pi},T=1^{-},0$ and $J^{\pi},T=1^{-},1$, respectively.

### 5.4 *E*1 transitions

The *E*1 transitions are the main input parts of the radiative capture amplitude for $^{15}$N($p$,$\gamma_0$)$^{16}$O reaction. Therefore, it is required to determine the resonance capture cross-sections for these transitions accurately to avoid one of the main sources of uncertainty. The radiative capture resonance to the bound states is reviewed in [179]. Following [118] after algebraic calculations using quantum numbers related to the $^{15}$N($p$,$\gamma$)$^{16}$O reaction, one can write the cross-section for the radiative capture $p^{15}$N to the ground state of $^{16}$O as:

$$\sigma_{E1}(E_{c.m.})=\frac{4\pi e^2}{9\hbar^2}\left(\frac{K}{k}\right)\left(\frac{1}{m_p}-\frac{7}{m_N}\right)\left|I(k;E1)\right| \tag{5.4}$$

In Eq. (5.4) $\mu$ is the reduced mass of the proton and $^{15}$N nucleus, $K=E\gamma/\hbar c$ is the wave number of the emitted photon with energy $E\gamma$, $k$ is relative motion wave

number and where the overlapping integral between the initial $\chi_i$ and final $\chi_f$ states radial wave functions is $I = \langle \chi_i | r | \chi_f \rangle$.

$$\begin{aligned} |I(k;E1|^2 &= \left| e^{-i\delta_{^3S_1(312)}} I_1 + e^{-i\delta_{^3S_1(962)}} I_2 \right|^2 = \\ &= |I_1|^2 + |I_2|^2 + 2\cos(\delta_{^3S_1(312)} - \delta_{^3S_1(962)}) I_1 I_2. \end{aligned} \tag{5.5}$$

While constructing the radial matrix element in Eq. (5.4), squared by the modulus, we explicity point out in Eq. (5.5) the importance of scattering-matrix for analyzing the interference effects. Note that, for non-interfering amplitudes, the phase-shift factor $\exp(-\delta_{LJ})$ convert to the unit in the final general expression for the total cross sections. Below, we demonstrate that $2\cos(\delta_{^3S_1(312)} - \delta_{^3S_1(962)}) I_1 I_2$ of the interference term plays an important role in the whole treted energy region, especially for the reaction rate at low temperatures.

In Eq. (5.5), the overlapping integral between the initial $\chi_i$ and $\chi_f$ state radial functions $I(k) = \int_0^\infty \chi_i^* r \chi_f \mathrm{d}r$ includes the interior and asymptotic regions via the continuous functions. The specific behaviour of the proton relative motion in the field of the $^{15}$N nucleus is considered via the nuclear interaction potentials $V(r)$. That is according to the declared above ansatz. Note that in the cluster model's single-channel approach, the actual asymptotic behaviour of the radial wave function is necessary for their proper normalizing.

As it is follows from Eq. (5.5) in the $E1$ resonance→ground state transitions the interference of $^3S_1(312)$ and $^3S_1(962)$ resonances give the contribution into the cross-section. The interference is determined by the difference of the $\delta_{^3S_1(312)}$ and $\delta_{^3S_1(962)}$ phase shifts via the factor $\cos(\delta_{^3S_1(312)} - \delta_{^3S_1(962)})$. We depict the behavior of this factor as a function of energy in Figure 5.2 using the phase shifts shown in Figure 5.1.

One can conclude that the contribution of the interfering term into the $E1$ transitions cross-section is very significant at the energies up to 2.5 MeV. For the comparison, we calculate the energy dependence of the factor $\cos(\delta_{R1} - \delta_{R2)})$ when the resonant $\delta_{R1}$ and $\delta_{R2}$ phase shifts are obtained using Eq. (5.4) by varying the width of the resonances from the experimental values $\Gamma_{R1}$= 91 keV and $\Gamma_{R2}$ = 130 keV [168] up to $\Gamma_{R1}$ = 120 keV and $\Gamma_{R2}$ = 250 keV (the upper and lower curves in Figure 5.2, respectively). The results of the calculations are shown in Figure 5.2 as a shaded area bounded by the upper and lower curves.

We can conclude that the factor $\cos(\delta_{R1} - \delta_{R2)})$ is sensitive to the width of the resonances at the energy interval about 400-800 keV and significantly increases the destructive interference.

### 5.5 Analysis of *S*-factor

Results of calculations for the astrophysical *S*-factor based on the potential parameters given in Table 5.2 along with the compilation of experimental data [148, 154, 157-159] are presented in Figure 5.3a. Notice that in [147] using *R* matrix approach was considered the contribution of $2^+$ level at the excitation energy 12.97 MeV. The contribution of this transition to the GS is much smaller than non-resonance $M1\ ^3P_1 \rightarrow {}^3P_0$ transition. The interference of two resonant contributions is dominant and gives the total capture cross-section for the $^{15}\mathrm{N}(p,\gamma_0)^{16}\mathrm{O}$ process. The interference of $^3S_1(312)$ and $^3S_1(962)$ resonances lead to the significant increase of *S*-factor at the energies up to 300 keV. Consideration of all transitions leads to increase of the *S*-factor at energies less than 300 keV and larger than 1500 keV. Moreover, one can see the discrepancies between the experimental data and theoretical calculation at energies where the minimum of the *S*-factor is observed. This is related to the destructive interference of $^3S_1(312)$ and $^3S_1(962)$ resonances at this energy due to the factor $\cos(\delta_{^3S_1(312)} - \delta_{^3S_1(962)})$. This factor has a minimum at about 500 keV as it is depicted in Figure 5.2. The similar results are obtained within the *R* matrix approach [147] when the authors are considering the different reaction components' contributions in the fitting of the $^{15}\mathrm{N}(p,\gamma)^{16}\mathrm{O}$ reaction data (see Figure 49, [147]).

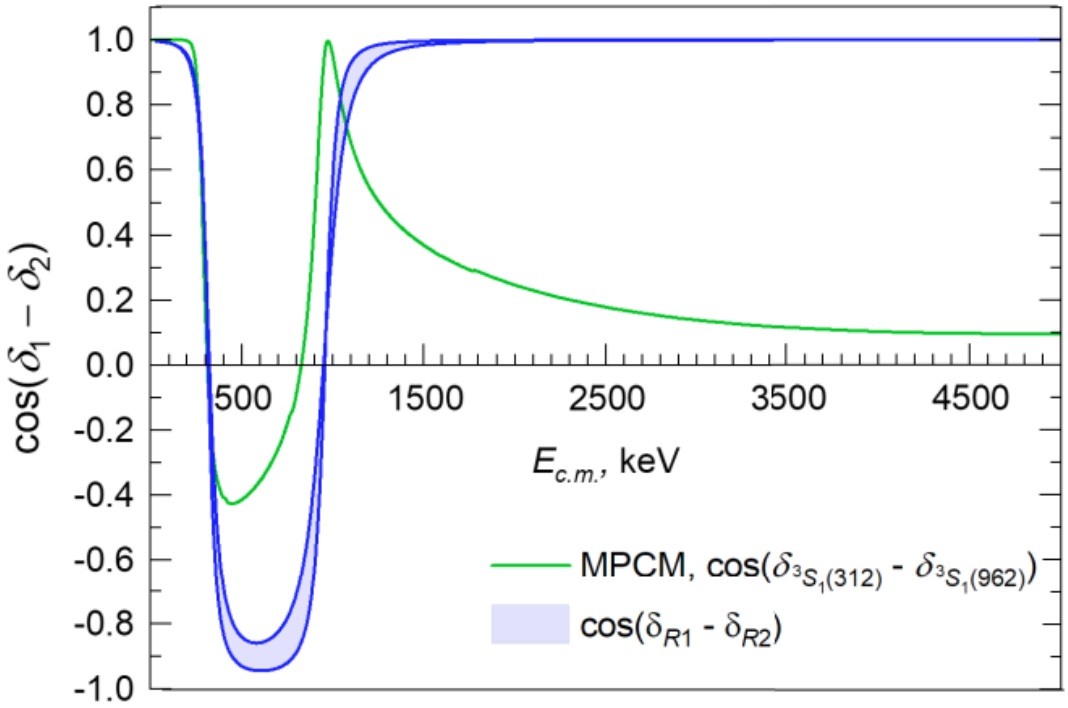


The upper and lower curves of the shaded area are obtained with the $\delta_{R1}$ and $\delta_{R2}$ resonant phase shifts that are calculated for the widths $\Gamma_{R1} = 91$ keV, $\Gamma_{R2} = 130$ keV and $\Gamma_{R1} = 120$ keV, $\Gamma_{R2} = 250$ keV, respectively.

Figure 5.2 – The energy dependence of the factors $\cos(\delta_{^3S_1(312)} - \delta_{^3S_1(962)})$ (green curve) and $\cos(\delta_{R1} - \delta_{R2})$ (shaded area)

Only by using the set of fitting parameters can be described the region of 0.5 MeV between resonances for the *S*-factor [147]. Let us mention that in the MPCM one has only the input parameters that are asymptotic constants and binding energies for the construction of BSs potentials, and spectra of the final nucleus or the scattering phase shifts of the particles of the entry channel for the construction of potentials of the scattering processes. The results of the contributions off all transitions of the S(E) is shown by shaded area in Figure 5.3b.

The contribution of the *M*1 non-resonant transition to the GS *S*-factor comes out of the MPCM model through the $^3P_1$ scattering state and has significance at the energies $E_{c.m.}$<500 keV. This contribution increases with the energy decrease. Consideration of the *M*1 transition requires the experimental (*p*,*p*) phase shift. Today experimental data for the elastic $^{15}$N(*p*,*p*)$^{15}$N cross-section are known only at energies higher than 2.7 MeV. The low energy elastic scattering experimental data are desirable to evaluate the intensity of the $^3P_1 \rightarrow {}^3P_0$ *M*1 transition.

What is the contribution of each transition to the *S*(0)? *E*1(312 keV) provides 15.5 keV·b (41%), *E*1(962 keV) gives 3.9 keV·b (10%), *M*1 does 2.6 keV·b (7%), and the interference term gives 15.7 keV·b (42%).

*R* matrix calculations reproduce the interference minimum more closely than the MPCM does. The consideration of the destructive interference of $^3S_1$(312) and $^3S_1$(962) resonances did not reproduce the minimum of the *S*-factor precisely. The consideration of another state is justified if it has the same quantum numbers $J^\pi = 1^-$ as the resonances we already considered. Such a state will interfere with the first two $1^-$ resonances. As was already mentioned in Sec II there is such a resonance in the $^{16}$O spectrum that lies at a very high excitation energy $E_x$=16.20(90) MeV. It is higher than the $^3S_1$(312) resonance by 3.76 MeV and by 3.11 MeV higher than the $^3S_1$(962).

In Table 5.3 the experimental data for the GS astrophysical S-factor in the measured energy ranges are given. The experimental range of energy is dramatically different which leads to the different values of $S(E_{min})$.

Table 5.3 – Experimental data on the astrophysical *S*-factor of the $^{15}$N(*p*,*γ*)$^{16}$O reaction. The values of $S(E_{\min})$ listed in rows 1 and 2 are taken from Figure 8 in [157]. $S(E_{\min})$ are given with the precision of one tenth of keV·b

| Reference | | $E_{c.m.}$, keV Experimental range | $E_{min}$, keV | $S(E_{min})$, keV·b |
|---|---|---|---|---|
| 1 | Hebbard *et al.*, 1960 [153] | 206-656 | 230 | 138.6±15.2 |
| 2 | Brochard *et al.*, 1973 [155] | 234-1219 | 256 | 215.1±27.3 |
| 3 | Rolfs & Rodney 1974 [154] | 139-2344 | 139 | 124.2±52.6 |
| 4 | Bemmerer *et al.*, 2009 [156] | 90-230 | 90 | 38.4±5.4 |
| 5 | LeBlanc *et al.*, 2010 [157] | 123-1687 | 123 | 53±7.1 |
| 6 | Caciolli *et al.*, 2011 [148] | 70-370 | 70 | 52±4 |
| 7 | Imbriani *et al.*, 2012 [158] | 131-1687 | 131 | 48.4±4.8 |

The numerical calculations have shown that the effect of this third in the spectrum of $1^-$ resonances is negligible, and its interference does not influence the value or position of the *S*-factor minimum.

In [154] the cross-section is measured for the highest energy, while in [4] are reported the cross-section for the lowest energy $E_{c.m}$ = 70 keV, which is near of the Gamow range [148]. It is obvious that extrapolation of the *S*(*E*) to the *S*(0) using each listed experimental energy range will give the different values of the *S*(0), sometimes dramatically different.

The determination of *S*(0) relies on the dual approach of experimental measurement of the cross section complemented by theoretical interpretation and extrapolation from the experimental range of energy to the zero energy. In Table 5.4 are listed the estimates of the astrophysical *S*-factor at zero energy *S*(0) obtained using the *R*-matrix fits of the different sets of experimental data, different model calculations, and extrapolation of the experimental data. By varying the fitting method, authors obtained different values of *S*(0), see for example [163]. Depending on the data used for the fit, the values of *S*(0) are scattered from 21 keV·b to 75 keV·b, as it is seen in Table 5.3. Theoretical evaluation of astrophysical *S*(*E*) and its extrapolation to *S*(0) are also model dependent, consequently, the uncertainties in the computed *S*-factor can be significant. The extrapolation is of insufficient accuracy because of the difficulties in taking full account of the complexities of the reaction mechanisms.

Table 5.4 – Values of the astrophysical *S*(0) factor of the $^{15}N(p,\gamma)^{16}O$ reaction. The estimations for values of the *S*(0) are obtained based of experimental data from references listed in the parentheses

| Reference | *S*(0), keV·b |
|---|---|
| Rolfs &Rodney, 1974 [154] | 32 ([170]) |
| | 64±6 ([171]) |
| Barker, 2008 [160] | 50-55 ([170]) |
| | 35 ([170]) |
| Mukhamedzhanov *et al*., 2008 [161] | 36.0±6 |
| LeBlanc *et al*., 2010 [157] | 39.6±2.6 |
| Huang *et al*., 2010 [68] | 21.1 |
| Mukhamedzhanov *et al*., 2011 [163] | 33.1-40.1 |
| Xu *et al*., 2013 [159] | 45 |
| DeBoer *et al.*, 2013 [147] | 40±3 |
| Dubovichenko *et al*., 2014 [162] | 39.4-43.35 |
| Son *et al.*, 2022 [166] | 30.4 ([172]) |
| | 75.3±12.1 ([172]) |
| Son *et al.*, 2022 [167] | 34.1±0.9 ([175]) |
| | 29.8±1.1 ([176]) |
| Present work | 34.7-40.4 |

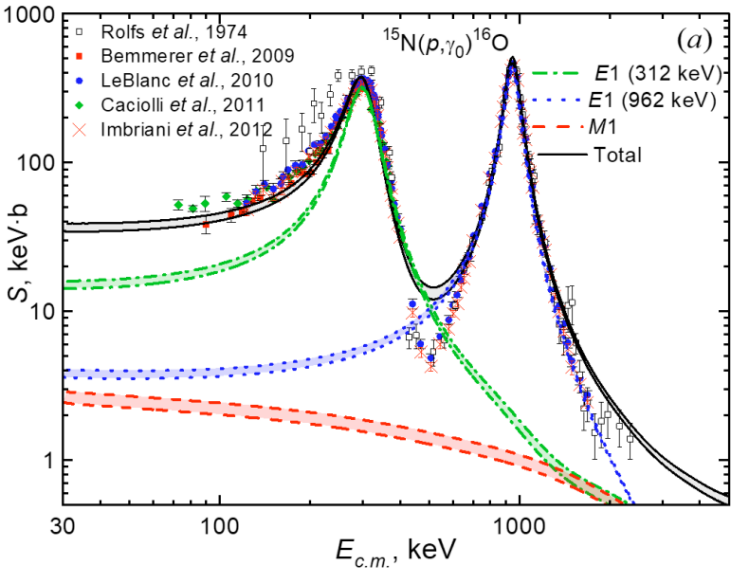


a)

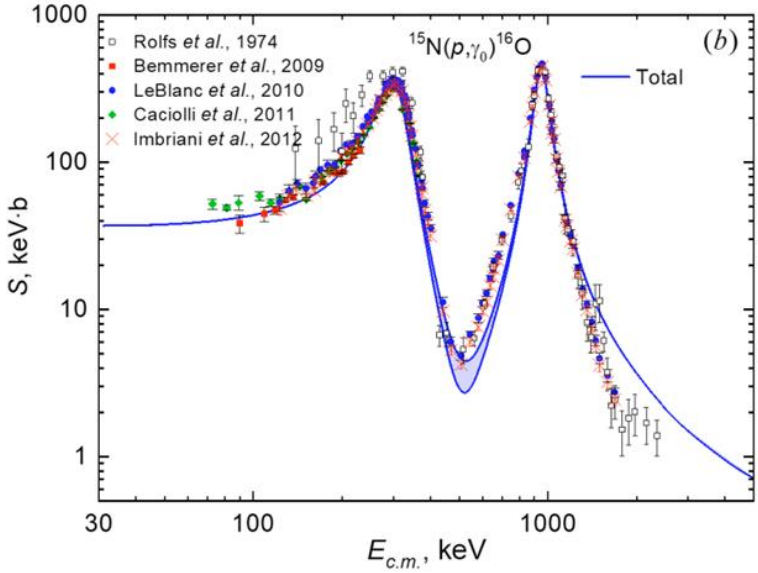


b)

a) The $E1$ transition $^3S_1 \rightarrow {}^3P_0$ for the resonance at 312(2) keV. The $E1$ transition $^3S_1 \rightarrow {}^3P_0$ for the resonance at 962(8) keV (the shaded area bounded by two curves) and $M1$ transition $^3P_1 \rightarrow {}^3P_0$ (the shaded area bounded by two dashed curves). The lower and upper bounded curves for $E1(962)$ resonance and $M1$ transitions are obtained for $C_w$=1.8 and $C_w$=2.05, respectively. The contribution of all transitions to the astrophysical $S$-factor is shown by the shaded area bounded by two solid curves. b) The $E1$ transitions $^3S_1 \rightarrow {}^3P_0$ for the resonances at 312(2) keV and 962 keV and the $M1$ transition $^3P_1 \rightarrow {}^3P_0$. Notations are the same as in (*a*). Calculations are performed using parameters set II. The contribution of all transitions to the astrophysical $S$-factor is calculated using the factor $\cos(\delta_{R1} - \delta_{R2})$ for the interference term is shown by the shaded area. The shaded area corresponds to the shaded area in Figure 5.2.

Figure 5.3 – The astrophysical $S$-factor of radiative $p^{15}$N capture on the ground state of $^{16}$O

### 5.6 Reaction rate

The reaction rates for nuclear fusion are the critical component for stellar-burning processes and the study of stellar evolution. In stellar interiors, where the interacting particles follow a Maxwell-Boltzmann distribution, the reaction rate describes the probability of nuclear interaction between two particles with an energy-dependent reaction cross section $\sigma(E)$. The reaction rate of proton capture processes can be written as:

$$N_A\langle\sigma v\rangle = N_A\left(\frac{8}{\pi\mu}\right)^{1/2}(k_BT)^{-3/2}\int\sigma(E)E_{\exp}\left(-\frac{E}{k_BT}\right)dE = N_A\left(\frac{8}{\pi v}\right)^{1/2}(k_BT)^{-3/2}\int S(E)e^{-2\pi\eta}\exp\left(-\frac{E}{k_BT}\right)dE. \quad (5.5)$$

In Eq. 5.5 $N_A$ is the Avogadro number, $\mu$ is the reduced mass of two interacting particles, $k_B$ is the Boltzmann constant, $T$ is the temperature of the stellar environment and the factor $e^{-\pi\eta}$ approximates the permeability of the Coulomb barrier between two point -like charged particles.

### 5.7 $^{15}$N($p$,$\gamma$)$^{16}$O reaction rate

The reaction rate can be numerically obtained in the framework of the standard formalism outline in [39] based on the *S*-factor that includes the contributions of all transitions shown in Figure 5.3 as well as fractional contributions of $E1$ transitions and $^3P_1\rightarrow{}^3P_0$ $M1$ transition to the $^{15}$N($p,\gamma_0$)$^{16}$O reaction rate. In Figure 5.4 are presented the reaction rate and fractional contributions of each transition to the reaction rate. The insert in Figure 5.4 shows the contribution of each resonance and $^3P_1\rightarrow{}^3P_0$ transition with respect to the total reaction rate as a function of astrophysical temperature. Such a presentation is useful to quickly understand the relevance of each transition at a given temperature.

At $T_9$=0.01 the fractional contribution from the 312 keV resonance is 71%, while the fractional contributions of the 962 keV resonance and non-resonance transition $^3P_1\rightarrow{}^3P_0$ are 16% and 13%, respectively. However, in contrast, at temperature $T_9$=10 the fractional contribution from the 962 keV resonance is 89% and contributions of 312 keV resonance and $^3P_1\rightarrow{}^3P_0$ transition are commensurate: 6% and 5%, respectively. The $E1$ transitions from 312 keV and 962 keV resonances have maximal fractional contributions 95% and 93% at $T_9$=0.4 and $T_9$=4.1, respectively. The fractional contribution from non-resonance transition $^3P_1\rightarrow{}^3P_0$ increases with the decrease of the energy. Thus, at the temperatures range between $T_9$=0.01-10 the $^{15}$N($p,\gamma_0$)$^{16}$O reaction rate is dominated by the tails of the resonances at energy 312 keV and 962 keV in the c.m.

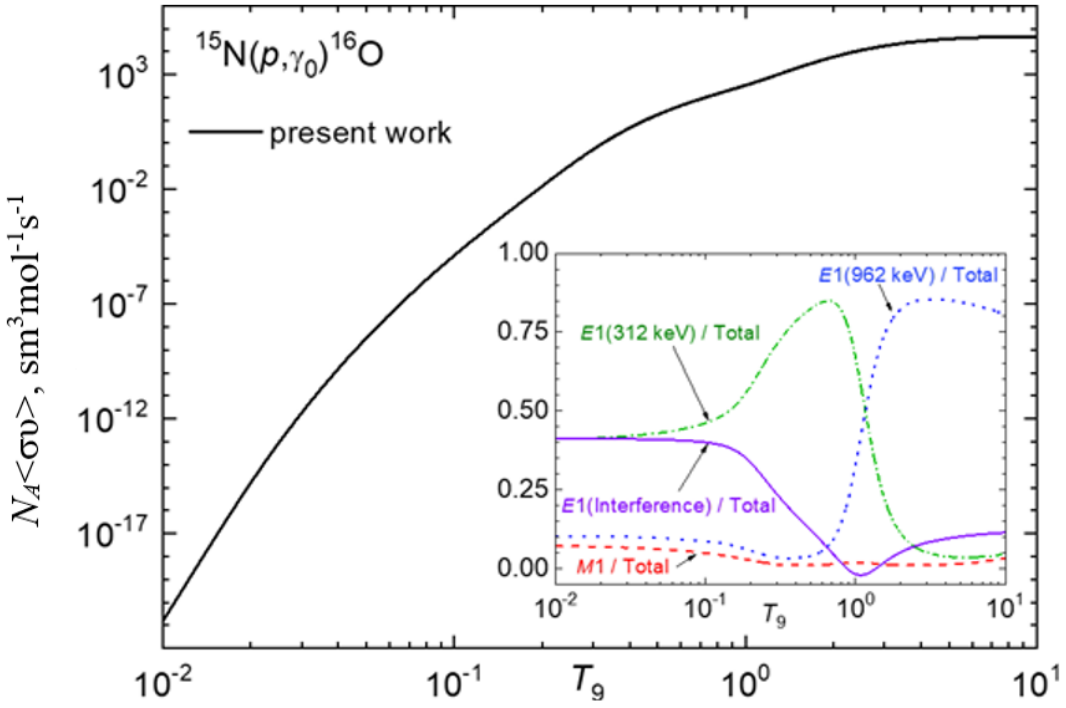


The solid curve presents the calculations for the sum of $E1$ and $M1$ transitions performed for the potentials with the sets of parameters from Table 5.2. The inset shows the fractional contributions of the reaction rates from the $^3S_1$ resonances at 312 keV and 962 keV, respectively, and non-resonance transition $^3P_1 \rightarrow {}^3P_0$ with respect to the reaction rate of $^{15}$N($p$,$\gamma$)$^{16}$O, as a function of astrophysical temperature. The resonances are identified with the c.m. energy in keV.

Figure 5.4 – The dependence of the reaction rate of the $^{15}$N($p$, $\gamma_0$)$^{16}$O radiative capture on astrophysical temperature

The interference of the $^3S_1$(312) and $^3S_1$(962) resonances requires special consideration. The solid line in the insert in Figure 5.4 shows the fractional contribution of the interference term between the $^3S_1$(312) and $^3S_1$(962) resonances to the total reaction rate. In the Gamow CNO window $T_9$=0.01 – 0.03, which is shown in Figure 5.8, the contribution of the interference term into the total reaction rate is 41% up to $T_9$=0.1.

In the temperature interval $T_9$=0.01 – 0.1 the contribution of the interference term to the total reaction rate is 40%, while at $T_9$=3 – 10, the contribution of this term does not exceed 11%. For the stellar CNO temperature range $T_9$=0.1 – 0.5 , the contribution of the interference term is dropping from 40% to 12.5 %.

The destructive interference is observed in the range from $T_9$ = 0.89 to $T_9$ = 1.36, but its role is on the level of 2%. Starting from the end of this interval up to $T_9$ = 10 a moderate increasing of a constructive interference is observed from zero up to 11%.

The reaction rates reported in [159] include cascade transitions via two resonances, and $0^-$ and $3^-$ of $^{16}$O resonances in the $0.40 \leq E_R \leq 1.14$ MeV range [61, 68, 158, 170]. It is stated in [159] the enhancement of the ratio around $T_9$ =1 seen in

Figure 5.5 is owing to the contribution of the cascade transitions, which are not included in NACRE [41].

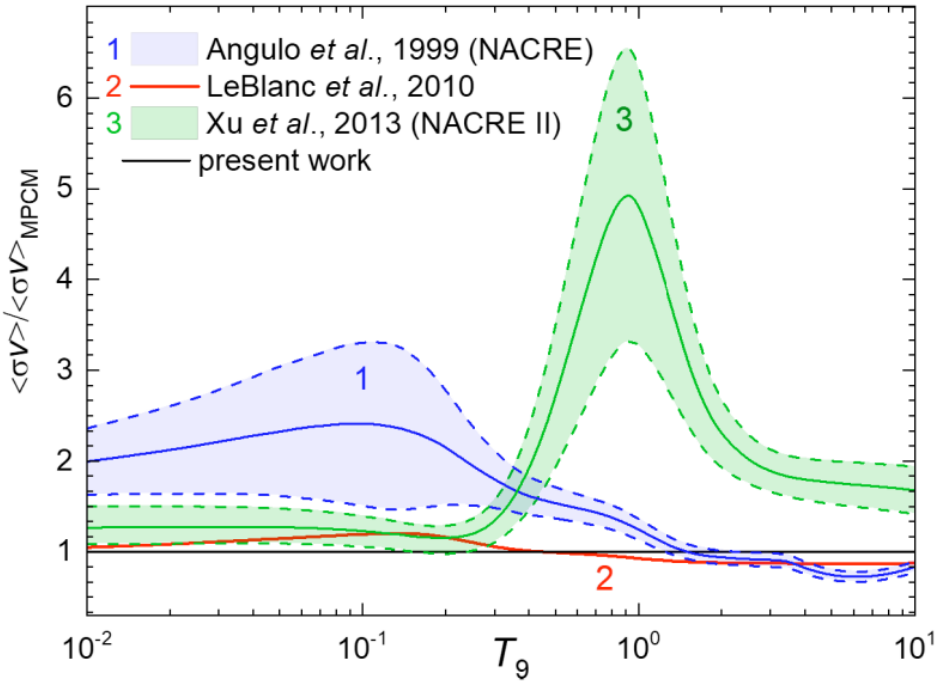


The shaded areas within the dashed curves represent the uncertainties from NACRE and NACRE II.The calculations from NACRE [39], LeBlanc et al. [157], and present calculations are given for the GS transition and NACRE II parametrization includes the GS transition and transitions via two $2^-$ resonances, and $0^-$ and $3^-$ resonances [159].

Figure 5.5 – The dependence of the ratio of the proton radiative capture on $^{15}$N reaction rate from NACRE [39] (curve 1), [157] (curve 2), NACRE II [159] (curve 3) and the present calculation on astrophysical temperature in the range of $T_9$ = 0.01-10

In [158, 171] partial cross sections of the radiative proton capture to the GS, 1$^{st}$ ($0^+$), 2$^{nd}$ ($3^-$) and 4$^{th}$ ($1^-$) excited states are measured, and converted to the astrophysical *S*-factors of the $^{15}$N$(p,\gamma_0)^{16}$O, $^{15}$N$(p,\gamma_{(6.050)})^{16}$O, $^{15}$N$(p,\gamma_{(6.130)})^{16}$O, and $^{15}$N$(p,\gamma_{(7.717)})^{16}$O reactions. The experimental data on $(p,\gamma_1)$, $(p,\gamma_2)$, $(p,\gamma_4)$ were reported by Imbriani *et al.* [171] as cascade transitions. We estimate the contribution of these transitions in the framework of the MPCM based on Imbriani's et al. [171] experimental data, because exact calculations of these transitions are out of the scope of the present paper.

One can estimate the contribution of the cascade transitions. Thus $[N_A\langle\sigma v\rangle]_m$ is modified GS reaction rate, which effectively includes the cascade transitions to the excited states of $^{16}$O: $^{15}$N$(p,\gamma_{(6.050)})^6$O, $^{15}$N$(p,\gamma_{(6.130)})^6$O and $^{15}$N$(p,\gamma_{(7.117)})^6$O.

The dependence of the reaction rate of the $^{15}$N$(p,\gamma_0)^{16}$O radiative capture as a function of temperature for astrophysical temperature between $T_9$ = 0.01-10 is shown in Figure 5.4. Results of the reaction rate calculations using the parameters' sets I - III for the potentials from Table 5.2 show that the differences of reaction rates are

negligible. Thus, while the astrophysical factor is sensitive to parameters of the potential, the latter do not affect the reaction rate. Results for the reaction rates for sets I - III are coincident and are shown by a single solid curve in Figure 5.5. The reaction rates of $^{15}$N($p,\gamma$)$^{16}$O were reported earlier in [39, 157, 159]. We normalized the reaction rate obtained within the *R* matrix approach NACRE [157], and NACRE II [159] reaction rates by dividing the corresponding data on the reaction rate obtained in the present calculation.

The dependence of these ratios as the function of astrophysical temperature is shown in Figure 5.6. One can see the agreement between the reaction rate [157] obtained for the GS transition and present calculation. It should be noted the agreement is also observed for the astrophysical factor: the range of results for $S(0)$ $34.7 \le S(0) \le 40.4$ keV b and from $37 \le S(0) \le 42.2$ keV b from [157] are overlapping. In calculations of $S(0)$ in [157] the used ANC 23 ± 3 fm$^{-1/2}$ about 3 times larger than the experimental value [161]. One can conclude that the reaction rate is weakly responsive to the value of $S(0)$.

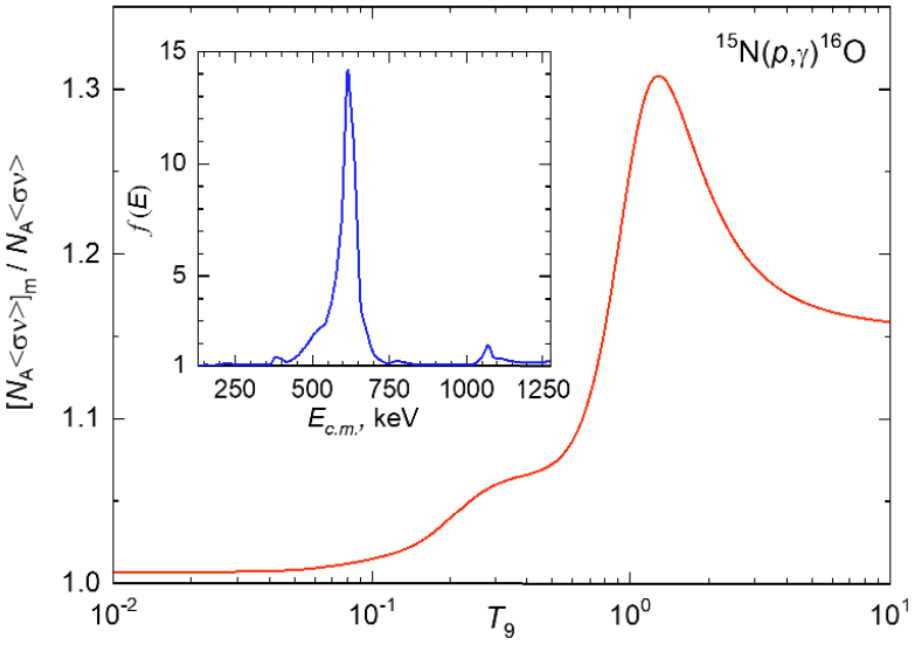


In calculations are used the experimental data reported in [158]. The inset shows the dependence of the factor $f(E)$ on the proton energy in the c.m.

Figure 5.6 – The dependence of the ratio of the total reaction rate which is the sum of contributions from the GS $^{15}$N($p,\gamma_0$)$^{16}$O and cascade transitions $^{15}$N($p,\gamma_{(6.050)}$)$^{16}$O, $^{15}$N($p,\gamma_{(6.130)}$)$^{16}$O, $^{15}$N($p,\gamma_{(7.717)}$)$^{16}$O and the reaction rate for the GS transition on temperature

The experimental data [158, 171] for *S*-factors are listed in the EXFOR database were used and interpolated with the Origin Pro 2018 software. The interpolation allows

to construct the energy-dependent factor $f(E) = \dfrac{\text{Total } S-\text{factor}}{\text{GS } S-\text{factor}}$, where "Total *S*-factor" corresponds to the sum of the $^{15}$N($p,\gamma_0$)$^{16}$O and the cascade transitions $^{15}$N($p,\gamma_{(6.050)}$)$^{16}$O, $^{15}$N($p,\gamma_{(6.130)}$)$^{16}$O, $^{15}$N($p,\gamma_{(7.717)}$)$^{16}$O, and "GS *S*-factor" refers to the $^{15}$N($p,\gamma_0$)$^{16}$O. Introducing this factor into Eq. (5.6):

$$[N_A\langle\sigma v\rangle_m = N_A\left(\frac{8}{\pi\mu}\right)^{1/2}(k_BT)^{-3/2}\int S(E)\times f(E)e^{-2\pi\eta}\exp\left(-\frac{E}{k_BT}\right)dE, \qquad (5.7)$$

One can estimate the contribution of the cascade transitions. Thus, $[N_A\langle\sigma v\rangle]_m$ is a modified GS reaction rae which effectively includes the cascade transitions to the excited states of $^{16}$O: $^{15}$N($p,\gamma_{(6.050)}$)$^{16}$O, $^{15}$N($p,\gamma_{(6.130)}$)$^{16}$O, $^{15}$N($p,\gamma_{(7.717)}$)$^{16}$O.

### 5.8 Comparison of rates for proton capture reactions on nitrogen isotopes

There are two stable nitrogen isotopes, $^{14}$N and $^{15}$N exist, and all other radioisotopes are short-lived. Among short-lived isotopes, the longest-lived are $^{12}$N and $^{13}$N with a half-life of about 11 ms and 9.965 min, respectively, and they are of nuclear astrophysics interest. A radiative proton capture on nitrogen isotopes in the reactions $^{12}$N($p,\gamma$)$^{13}$O, $^{13}$N($p,\gamma$)$^{14}$O, $^{14}$N($p,\gamma$)$^{15}$O, and $^{15}$N($p,\gamma$)$^{16}$O produces the short-lived $^{13}$O, $^{14}$O, $^{15}$O isotope with a half-life of 6 ms, 71 s and 122 s, respectively, and a stable $^{16}$O nucleus.

These radiative capture reactions caused by the electromagnetic interaction are significantly slower than reactions induced by the strong interactions. Therefore, these slow reactions control the rate and time of cycles of oxygen isotopes nucleosynthesis at astrophysical temperatures.

The authors in [191] suggested and discussed three alternative paths of rapid processes of the CNO cycle leading to the formation of $^{14}$O through the breakout reactions $^{9}$C($\alpha,p$)$^{12}$N and $^{11}$C($p,\gamma$)$^{12}$N. These three branches of reaction sequences involve $^{12}$N($p,\gamma$)$^{13}$O, $^{13}$N($p,\gamma$)$^{14}$O processes. Thus, these processes are of particular interest for nuclear astrophysics. In the framework of the MPCM the radiative proton capture on nitrogen isotopes $^{12}$N, $^{13}$N, and $^{14}$N were investigated [192, 193].

Because the reactions $^{12}$N($p,\gamma$)$^{13}$O, $^{13}$N($p,\gamma$)$^{14}$O, and $^{14}$N($p,\gamma$)$^{15}$O and the present study of $^{15}$N($p,\gamma$)$^{16}$O are considered on the same footing within the MPCM, it is useful to compare the reaction rates to understand the relevance of each process at a given astrophysical temperature.

The radiative proton $^{12}$N($p,\gamma$)$^{13}$O, $^{13}$N($p,\gamma$)$^{14}$O, $^{14}$N($p,\gamma$)$^{15}$O, $^{15}$N($p,\gamma$)$^{16}$O processes have the same Coulomb barrier and, as follows from Eq. (5.6), the reaction rates will differ only due to the different values of the $S(E)$ and reduced mass $\mu$ of interacting particles in the entrance channel.

Figure 5.7 gives an overview of the reaction rates for typical CNO temperature and explosive hydrogen burning scenarios. The $^{15}$N($p,\gamma$)$^{16}$O reaction is the fastest one with the biggest rate up to $T_9$=0.175 and $p^{14}$N is the slowest process up to $T_9$=0.1 and it controls the rate and time of nucleosynthesis cycles. One should notice that

$^{15}$N($p,\gamma$)$^{16}$O rate becomes the dominant one at temperature explosive hydrogen burning scenarios in stars.

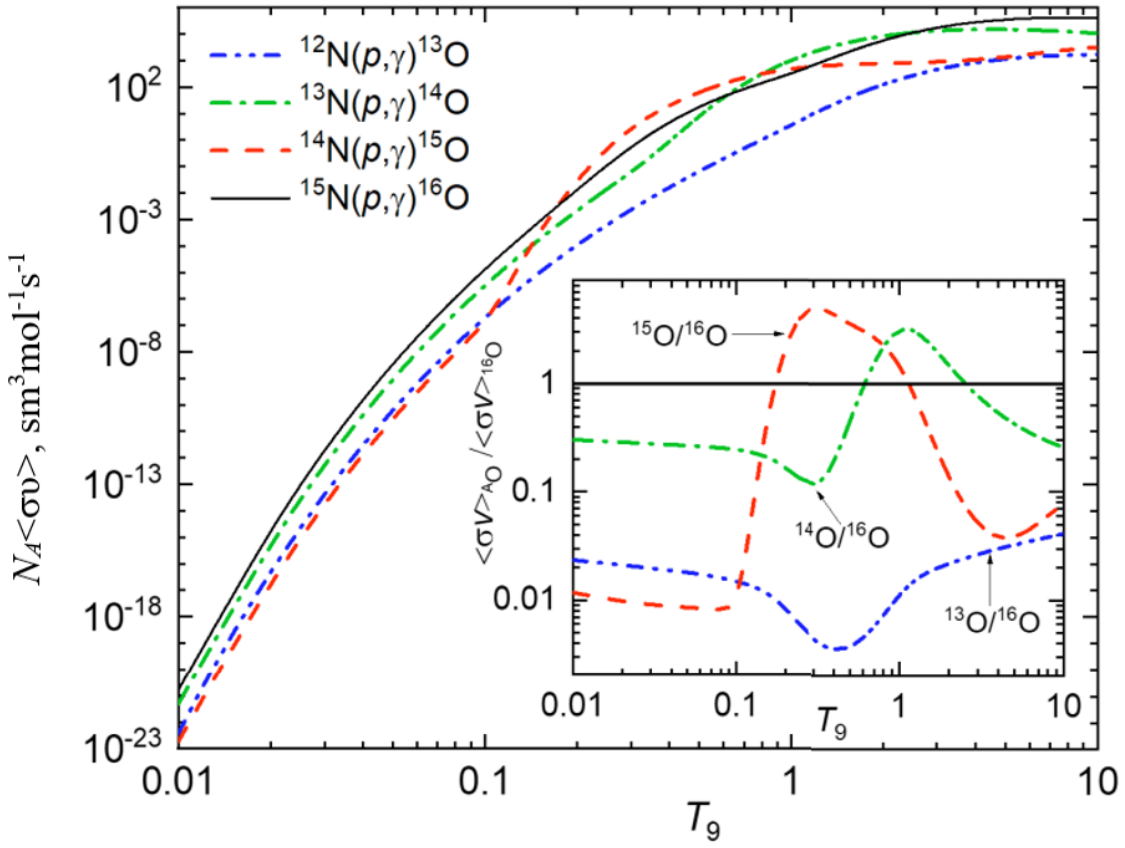


The insert shows the fractional contributions from $^{12}$N($p,\gamma$)$^{13}$O, $^{13}$N($p,\gamma$)$^{14}$O, $^{14}$N($p,\gamma$)$^{15}$O with respect to the $^{15}$N($p,\gamma$)$^{16}$O reaction rate as a function of astrophysical temperature.

Figure 5.7 – The reaction rates of the radiative proton capture on nitrogen isotopes leading to the production of oxygen isotopes as a function of astrophysical temperature

The reduced masses of the pairs $p^{12}$N, $p^{13}$N, $p^{14}$N, and $p^{15}$N are always less than the proton mass and are within the range $0.9294 \le \mu \le 0.9439$ amu. Therefore, the influence of the reduced mass on the reaction rates of the proton capture on nitrogen isotopes is negligible and can be omitted. Therefore, the rates of these processes completely depend on the reaction *S*-factor.

The analysis of the result presented in the insert in Figure 5.7 leads to the conclusion that only in the temperature windows $0.18 \le T_9 \le 1.14$ and $0.66 \le T_9 \le 3$ the reaction $^{15}$N($p,\gamma$)$^{16}$O is slower than $^{13}$N($p,\gamma$)$^{14}$O and $^{14}$N($p,\gamma$)$^{15}$O reactions, respectively. Hence this slow reaction controls the rate and time of cycles of nucleosynthesis.

Thermonuclear reactions occur mainly over the Gamow energy window from

$E_0 - \Delta E_G / 2$ to $E_0 + \Delta E_G / 2$ except in the case of narrow resonances. From Eqs. (5.10) and (5.11) is clear that the Gamow's peak energies and ranges for $^{12}$N($p,\gamma$)$^{13}$O, $^{13}$N($p,\gamma$)$^{14}$O, $^{14}$N($p,\gamma$)$^{15}$O, $^{15}$N($p,\gamma$)$^{16}$O reactions are completely determined by the astrophysical temperature.

The variation of the reduced mass within $0.9294 \leq \mu \leq 0.9439$ amu changes the Gamow's peak energy and the energy range only within 0.5% and 0.3%, respectively. It is useful to present the reaction rate for a particular temperature range along with the Gamow window of CNO reactions for the radiative proton capture on nitrogen isotopes.

The corresponding results of calculations are shown in Figures 5.8 and 5.9. It should be noticed that the main difficulty in determining reliable reaction rates of $^{12}$N($p,\gamma$)$^{13}$O, $^{13}$N($p,\gamma$)$^{14}$O, $^{14}$N($p,\gamma$)$^{15}$O, $^{15}$N($p,\gamma$)$^{16}$O reactions for the CNO cycles is the uncertainty in the very low cross-sections at the Gamow range.Developments within the low-energy underground accelerator facility LUNA in the Gran Sasso laboratory [194] and recent improvements in the detection setup [195] make taking direct measurements of nuclear reactions near the Gamow range feasible. This advantage has been demonstrated in the $^{14}$N($p,\gamma$)$^{15}$O reaction, which was successfully measured down to energies of 70 keV at LUNA [196].

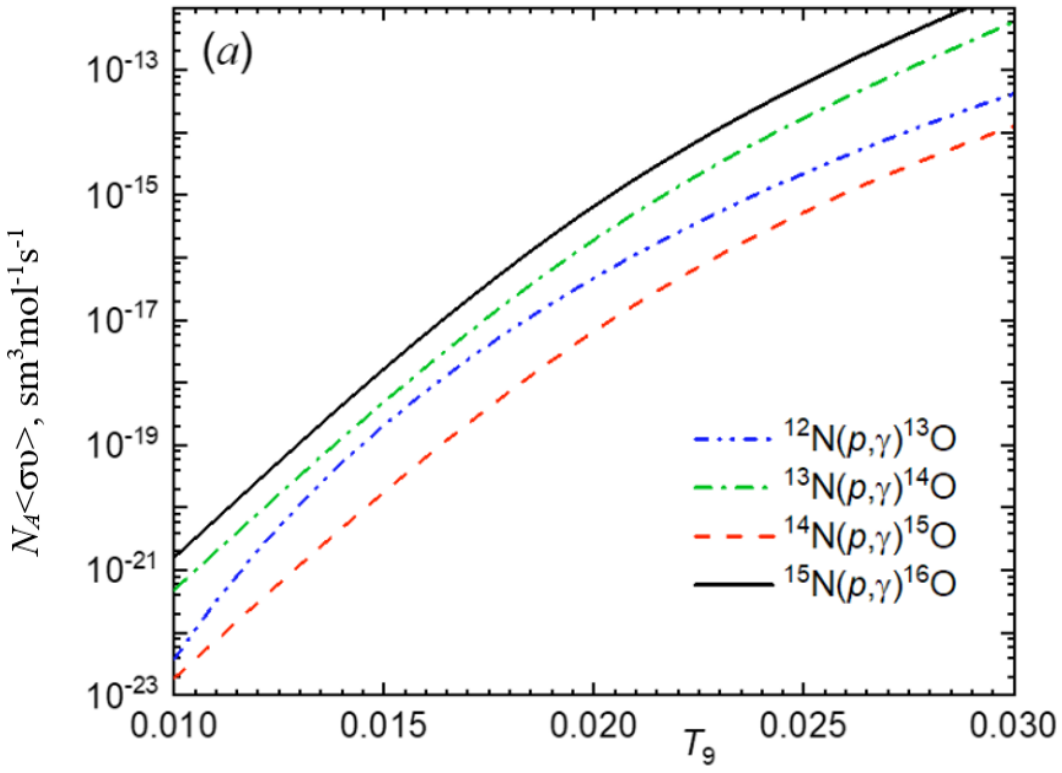


a)

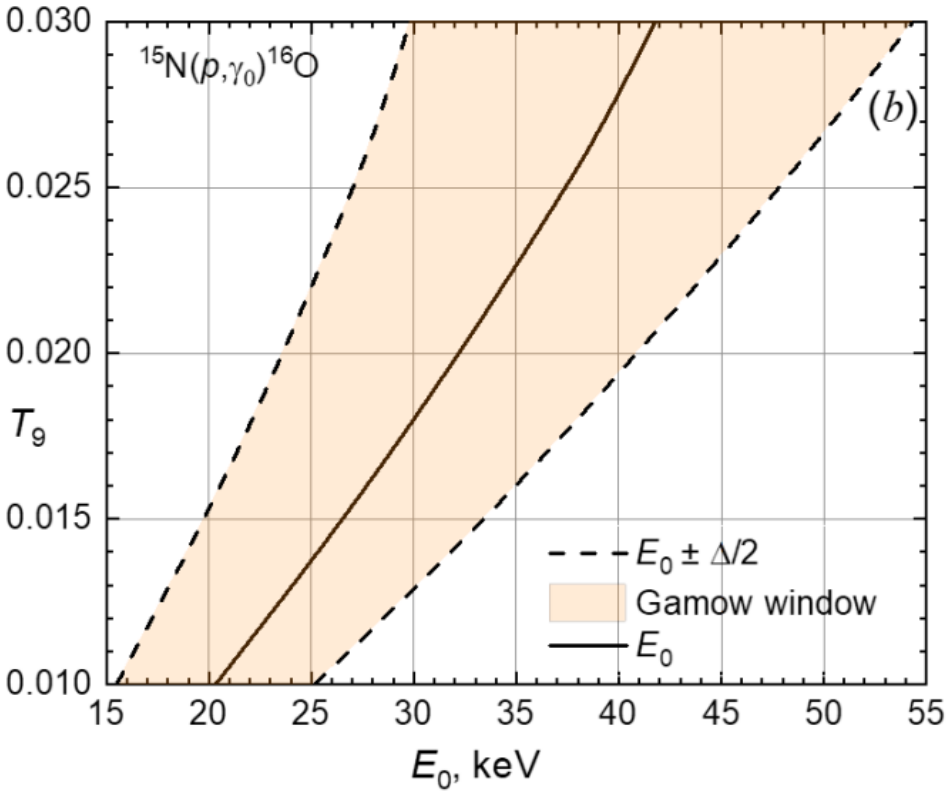


b)

Figure 5.8 – a) Dependencies of reaction rates of the radiative proton capture on nitrogen isotopes on astrophysical temperature in the range of $T_9$=0.01− 0.03 b) The stellar temperatures as a function of the Gamow energy for CNO cycle $^{12}$N($p$,$\gamma$)$^{13}$O, $^{13}$N($p$,$\gamma$)$^{14}$O, $^{14}$N($p$,$\gamma$)$^{15}$O and $^{15}$N($p$,$\gamma$)$^{16}$O reactions

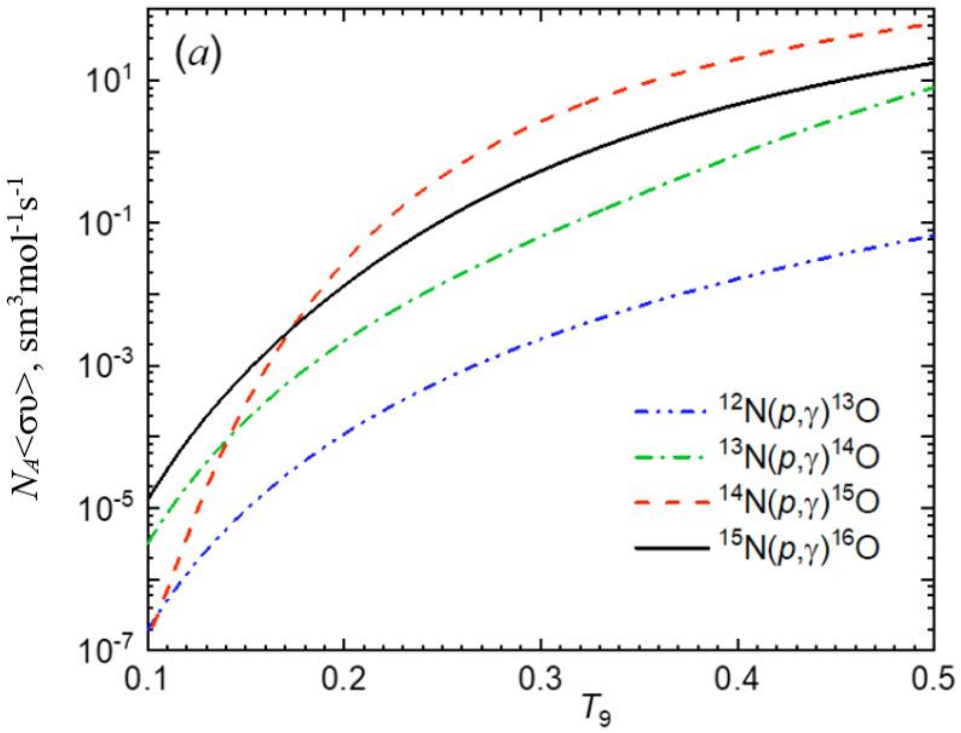


a)

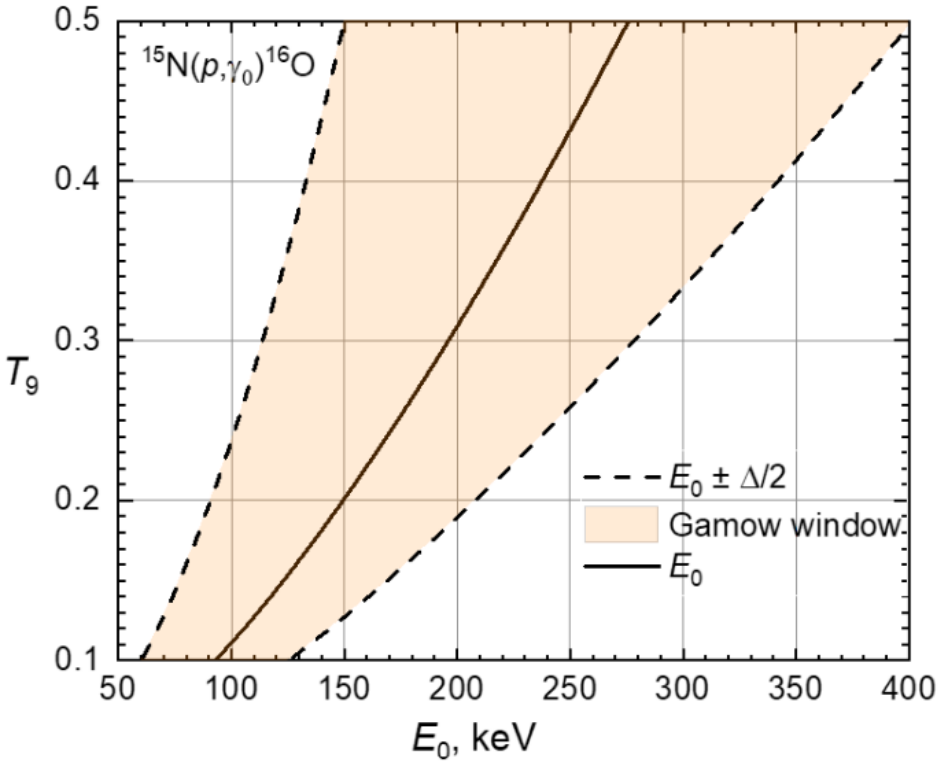


b)

Figure 5.9 – a) Dependencies of reaction rates of the radiative proton capture on nitrogen isotopes on astrophysical temperature in the range of $T_9 = 0.1 - 0.5$ b) The stellar temperatures as a function of the Gamow energy for CNO cycle $^{12}$N($p$,$\gamma$)$^{13}$O, $^{13}$N($p$,$\gamma$)$^{14}$O, $^{14}$N($p$,$\gamma$)$^{15}$O and $^{15}$N($p$,$\gamma$)$^{16}$O reactions

### 5.9 Concluding remarks

We present the results of calculations and analysis of the astrophysical $S$-factor and reaction rate for the $^{15}$N($p,\gamma$)$^{16}$O reaction in the framework of MPCM with FSs, including low-lying $^3S_1$ resonances and $^3P_1 \rightarrow {}^3P_0$ $M1$ transition. The intercluster potentials of the bound state, constructed on the basis of quite obvious requirements for the description of the binding energy and AC in $p^{15}$N channel of the GS and the scattering potentials describing the resonances, make it possible to reproduce the available experimental data for the total cross-section of radiative proton capture on $^{15}$N nucleus at astrophysical energies.

The reaction rate is calculated and parameterized by the analytical expression at temperatures ranging from $T_9$=0.01-10 and compared with the existing rates. The reaction rate has negligible dependence on the variation of AC but shows a strong impact of the interference of $^3S_1$(312) and $^3S_1$(962) resonances, especially at $T_9$ referring to the CNO Gamow windows. The significant discrepancies between the $^{15}$N($p,\gamma$)$^{16}$O reaction rate presented in the NACRE and NACRE II databases and present calculations are found.

We estimated the contribution of the cascade transitions to the reaction rate. The enhancement of the ratio of the sum of GS and cascade transitions and the GS transition at $T_9 > 0.3$ is owing to the contribution of the $^{15}$N($p,\gamma_{(6.050)}$)$^{16}$O, $^{15}$N($p,\gamma_{(6.130)}$)$^{16}$O, and $^{15}$N($p,\gamma_{(7.117)}$)$^{16}$O processes.

We compare the reaction rates for $^{12}$N($p,\gamma$)$^{13}$O, $^{13}$N($p,\gamma$)$^{14}$O, $^{14}$N($p,\gamma$)$^{15}$O, $^{15}$N($p,\gamma$)$^{16}$O reactions involved into different branches of the CNO cycle obtained in the framework of the same model, MPCM, and determine temperature windows, prevalence, and significance of each process. The comparison of the reaction rates indicates which slow reactions control the rate and time of cycles of oxygen isotopes nucleosynthesis at particular astrophysical temperatures. We present the temperature range along with the Gamow window for CNO reactions for the radiative proton capture on nitrogen isotopes. This is useful as a guideline for experimental measurements involving reactions of the radiative proton capture on nitrogen isotopes to obtain a reliable extrapolation of $S(E)$ to the astrophysical $S$-factor.

## CONCLUSION

Based on the phase shifts obtained, the binary interaction potentials within the cluster model approach were constructed and the total cross sections, astrophysical *S*-factor and reaction rates for the radiative capture reactions $n^8$Li, $n^9$Be, $n^{13}$B and $p^{15}$N were calculated.

As a result of the research, the following conclusions were formulated.

1. The total cross sections and reaction rates are calculated for the reaction $^8$Li$(n,\gamma_{0+1})^9$Li, including the corrections inserted for the interaction potentials comparing the early work. The experimentally proved resonance at $E_{c.m.} = 0.232$ MeV in the $^4P_{5/2}$ wave and ab initio-predicted $^4P_{3/2}$ resonance at 1.32 MeV [52] are considered. The intensity of $^4P_{5/2}$ resonance depends strongly on the range of asymptotic constants $C_w$, as well as the cross sections as a whole, which is observed in the temperature $T_9$ dependence of the reaction rates.

The minor role of the $(n,\gamma_1)$ process is proved; therefore, the GS transitions are dominant. The variation in the GS asymptotic constant $C_w = 0.93–1.40$ leads to the values of the reaction rate 5,740–11,000 $cm^3 \cdot mol^{-1} \cdot s^{-1}$ at temperature $T_9 = 1$ relevant for the r-formation of $^9$Li. The upper value nearly coincides with the *ab initio* reaction rate 11,770 $cm^3 \cdot mol^{-1} \cdot s^{-1}$ at $T_9 = 1$ [52], but we acknowledge this agreement as occasional.

Two criteria to narrow down the range of reaction rates in present study were suggested. The first one concerns the values of thermal cross sections. Analysis of $\sigma_{therm}$ values leads us to conclude that the upper set calculations yielding 46.8 mb ($C_w$= 1.40) are more relevant as they conform to estimations carried out in [44] and data on the $^6$Li and $^7$Li isotopes [14]. The second criterion is related to the reaction rates of radiative neutron capture on lithium isotopes $^{6,7,8}$Li. The examined correlation between the energy thresholds and order of reaction rates at low temperatures beyond the possible resonances $T_9 < 0.2$ leads to the conclusion that upper-set calculations are more reasonable (see Figure 2.5). The recent results on the reaction rates obtained in [52, 53] show substantial differences, both qualitative and quantitative. The present calculations do not eliminate this discrepancy. The new measurements proposed in [41] may clarify the situation.

2. The partial and total cross-sections of $^9$Be$(n,\gamma_{0+1+2+3+4+5})^{10}$Be reaction are calculated in the energy range from $10^{-5}$ to 5 MeV in the MPCM. The expansion of the energy range to 5 MeV allows us to consider five $^3D_3^1$, $^3F_2^1$, $^3F_3$, $^3F_2^2$ and $^3D_3^2$ resonances and estimate their signature in the total cross-section. A narrow resonance of $E_x = 0.730$ MeV is proposed as $^3F_2^1$ state, but not the *P*. Comparing the GS partial cross-section, the transitions to the 1st and 2nd ESs give essential input in the total cross-section. The role of the $(n,\gamma_3)$ process is illuminating with energy increasing. The minor role of the $(n,\gamma_4)$ and $(n,\gamma_5)$ processes is proved numerically.

The calculated thermal cross-section $\sigma_{th} = 8.35$ mb is in good agreement with experimental data [45, 91-93], which are ~ 10% lower than the early measurements [94, 120]. That is a reason for discussions addressed to the experimentalists.

The total and partial rates of $^{9}$Be($n,\gamma_{0+1+2+3+4+5}$)$^{10}$Be reaction are calculated in the temperature range of 0.001 to 10 $T_9$ and are approximated by the analytical expression. The inclusion of resonances shows their impact on the corresponding reaction rate within the factor 4-5 rising at $T_9$ >1, comparing the results of [16, 86].

The lack of experimental data on the cross-sections higher than 500 keV illuminates the problem of the quantitative reproducing of the first 0.559 MeV resonance, as it makes the most significant contribution to the rate of $^{9}$Be($n,\gamma$)$^{10}$Be reaction. New experimental measurements are in high demand.

Finally, it is worth mentioning that the theoretical research of the $^{9}$Be($n,\gamma$)$^{10}$Be reaction can be applied to the isobar-analog process $^{9}$Be($p,\gamma$)$^{10}$B. The comparative study of these processes within the same theoretical approach can provide the beryllium–boron branching under discussion.

3. The total cross sections of $^{13}$B($n$, $\gamma_{0+1}$)$^{14}$B reaction are calculated in MPCM based on $E1$ and $M1$ transitions from $10^{-2}$ eV to 5 MeV. We proved strong sensitivity of the cross sections on the asymptotic constant $C_w$ provided the proper long-range dependence of radial bound $S$-wave functions, ad hoc, the larger $C_w$, the greater the absolute values of cross-sections. The role of the FS in the calculated spectrum turned out to be insignificant.

The $E1$ transitions provided the background of the cross-section due to the capture from the non-resonance $^{3+5}P_2$, $^{5}P_3$, $^{3}P_0$ waves, and the resonant $^{3+5}P_1$ wave in the initial channel reveals the resonance structure of the cross-section at ~ 300 keV.

The $M1$ transition occurs via the $S$ scattering wave and contributes predominantly into the thermal cross-sections. Variation of $C_w$=1.4–2.4 gives the range of $\sigma_{therm} = 5.1-8.9$ mb. These values $\sigma_{therm}$ have not been ever estimated in theory, which seems important for experimentalists.

The reaction rates of $^{13}$B($n,\gamma_{0+1}$)$^{14}$B process show the same dependence on the asymptotic constant $C_w$ and relative contributions of ($n,\gamma_0$) and ($n,\gamma_1$) channels. The results of MPCM calculations differ cardinally from those of Rauscher *et al*. [8] in the whole $T_9$ range. Therefore we conclude that the present data on the reaction rates substantiate the role of $^{13}$B($n,\gamma_{0+1}$)$^{14}$B reaction in the Boron-Carbon-Nitrogen chains, i.e., this is not the break-point of the Boron sequence.

To support the conclusion, we estimated the relationship between the mean lifetime of $^{13}$B β decay $\tau_\beta$ and neutron capture time $\tau(n,\gamma)$. The temperature window for the ignition of $^{14}$B $r$-production 0.1 – 0.8$T_9$ related to the neutron densities $\bar{n}_n$ = 5 $10^{21}$ – 1.5 $10^{22}$ cm$^{-3}$ is determined, while $\bar{n}_n$ > 1.5 $10^{22}$ cm$^{-3}$ there are no temperature limits. We demonstrated that the preferences for $^{13}$B($n,\gamma_{0+1}$)$^{14}$B reaction directly depend on the reaction rate values, the larger $\langle\sigma_{n,\gamma}v\rangle$, the shorter the neutron capture time $\tau(n,\gamma)$.

We foresee the following factors may increase the reaction rate: inclusion of the $D$-component into the bound ground state (its weight is estimated today at ~ 17%) may enhance the input of the $1^+$ resonance to $E1$ capture cross-section at 305 keV. The role of the transitions denoted in Figure 4.2, but not considered in the present study, might

be evaluated, as the example of inclusion rather weak $(n,\gamma_1)$ process leads to the narrowing of the ignition temperature interval. Another problem concerns the determination of $3^{\pi}$ level parity at $E_x = 4.06$ MeV. If $\pi = +1$, the additional $E1$ transition may occur. In case $\pi = -1$, $E2$ transition may reveal interference effects with $3^-$ state at $E_x = 1.38$ MeV.

The unique experimental results on the Coulomb dissociation of $^{14}$B [13], converted into the cross-section of $^{13}$B$(n,\gamma)^{14}$B reaction, remain preliminary and not completed with estimated uncertainties.

We assume the results for the reaction rate of $^{13}$B$(n,\gamma_{0+1})^{14}$B may change the point of view on its minor impact on the heavy elements production expressed in [126]. The present calculations are predictive and estimative for substantiation of the performing the new experiments of the neutron capture on $^{13}$B and give the model estimation of the reaction rate of synthesis of $^{14}$B isotope in the $n^{13}$B channel for the first time.

4. The results of calculations and analysis of the astrophysical $S$-factor and reaction rate for the $^{15}$N$(p,\gamma)^{16}$O reaction in the framework of MPCM with forbidden states, including low-lying $^3S_1$ resonances and $^3P_1 \rightarrow {}^3P_0$ $M1$ transition are presented. The intercluster potentials of the bound state, constructed on the basis of quite obvious requirements for the description of the binding energy and AC in $p^{15}$N channel of the GS and the scattering potentials describing the resonances, make it possible to reproduce the available experimental data for the total cross-section of radiative proton capture on $^{15}$N nucleus at astrophysical energies.

The reaction rate is calculated and parameterized by the analytical expression at temperatures ranging from $0.01T_9$ to $10T_9$ and compared with the existing rates. The reaction rate has negligible dependence on the variation of AC, but shows a strong impact of the interference of $^3S_1(312)$ and $^3S_1(962)$ resonances, especially at $T_9$ referring to the CNO Gamow windows. The significant discrepancies between the $^{15}$N$(p,\gamma)^{16}$O reaction rate presented in the NACRE and NACRE II databases and present calculations are found. We estimated the contribution of the cascade transitions to the reaction rate. The enhancement of the ratio of the sum of GS and cascade transitions and the GS transition at $T_9 > 0.3$ is owing to the contribution of the $^{15}$N$(p,\gamma_{(6.050)})^{16}$O, $^{15}$N$(p,\gamma_{(6.130)})^{16}$O, and $^{15}$N$(p,\gamma_{(7.117)})^{16}$O processes. We compare the reaction rates for $^{12}$N$(p,\gamma)^{13}$O, $^{13}$N$(p,\gamma)^{14}$O, $^{14}$N$(p,\gamma)^{15}$O, $^{15}$N$(p,\gamma)^{16}$O reactions involved into different branches of the CNO cycle obtained in the framework of the same model, MPCM, and determine temperature windows, prevalence, and significance of each process. The comparison of the reaction rates indicates which slow reactions control the rate and time of cycles of oxygen isotopes nucleosynthesis at particular astrophysical temperatures. We present the temperature range along with the Gamow window for CNO reactions for the radiative proton capture on nitrogen isotopes. This is useful as a guideline for experimental measurements involving reactions of the radiative proton capture on nitrogen isotopes to obtain a reliable extrapolation of $S(E)$ to the astrophysical $S$ - factor at zero energy.

## REFERENCES


1. Rauscher T. Essentials of Nucleosynthesis and Theoretical Nuclear Astrophysics. – IOP Publishing Ltd, 2020. – 426 p.
2. Iliadis C. Nuclear Physics of Stars. – John Wiley & Sons, 2007. – 680 p.
3. Kajino T. Inhomogeneous big-bang model, revived, and evolution of the light elements in cosmic rays // Nucl. Phys. A. – 1995. – Vol. 588. – P. 339-343.
4. Coc A. Primordial Nucleosynthesis // J. Phys. Conf. Ser. – 2016. – Vol. 665. – 012001.
5. Coc A., Goriely S., Xu Y., Saimpert M., Vangioni E. Standard big bang nucleosynthesis up to CNO with an improved extended nuclear network // Astrophys. Jour. – 2011. – Vol. 744. – P.158-176.
6. Terasawa M., Samiyoshi K., Kajino T., Tanihata I., Mathews G. New Nuclear Reaction Flow during *r* -Process Nucleosynthesis in Supernovae: Critical Role of Light, Neutron-rich Nuclei // Astrophys. J. – 2001. – Vol. 562. – P. 470-479.
7. Wang Y., Guo B., Jin S., Li Z., Binh D., Hashimoto H., Hayakawa S., He J., Iwasa N., Kubono S., Kume N., Li E., Yamaguchi H. Indirect measurements of reactions in hot p-p chain and CNO cycles // AIP Conf. Proc. – 2012. – Vol. 1484. – P. 19-24.
8. Piatti D., Chillery T., Depalo R., Aliotta M., Bemmerer D., Best A., Boeltzig A., Broggini C., Bruno C. Underground experimental study finds no evidence of low-energy resonance in the $Li^6(p,\gamma)Be^7$ reaction // Phys. Rev. C. – 2020. – Vol. 102. – 052802.
9. Ananna C., Barile F., Boeltzig A., Bruno C., Cavanna F., Ciani G., Compagnucci A., Csedreki L., Depalo R., Ferraro F., Masha E., Piatti D., Rapagnani D., Skowronski J. Underground Measurements of Nuclear Reaction Cross-Sections Relevant to AGB Stars // Universe. – 2021. – Vol. 8. – P. 8-22.
10. Ananna C., Barbieri L., Boeltzig A., Campostrini M., Casaburo F., Ciani G., Compagnucci A., Gesue R., Marsh J., Masha E., Mercogliono D., Rapagnani D., Robb D., Sidhu R., Skowronski J. Recent results and future perspectives with solid targets at LUNA // Front. Astr. Space Sci. – 2024. – Vol. 10. – 1325053.
11. Kajino T., Aoki W., Balantekin A., Diehl R., Famiano M., Mathews G. Current status of r-process nucleosynthesis // Prog. Part. Nucl. Phys. – 2019. – Vol. 107. – P. 109-166.
12. Zecher P., Galonsky A., Gaff S., Kruse J., Kunde G., Tryggestad E., Wang J., Warner R., Morrissey D., Ieki K., Iwata Y., Deak F., Horvath A., Seres Z., Kolata J., Schelin H. Measurement of the $^8Li(n,\gamma)^9Li$ cross section at astrophysical energies by reverse kinematics // Phys. Rev. C. – 1998. – Vol. 57. – P. 959-966.
13. Altstadt S., Adachi T, Aksyutina Y., Alcantara J., Alvarez H., Ashwood N., Atar L., Aumann T., Avdeichikov V., Barr M., Beceiro S., Bemmerer D., Benlliure J., Bertulani C., Boretzky K., Borge M., Burgunder G., Caamano M., Caesar C., Casarejos E., Zuber K. $^{13,14}B(n,\gamma)$ via Coulomb Dissociation for Nucleosynthesis towards the r-Process // Nuclear Data Sheets. – 2014. – Vol. 120. – P. 197-200.
14. Iliadis C. Nuclear physics of stars. Second Volume. – Weinheim, Germany: Wiley-VCH Verlag GmbH & Co. KGaA, 2015. – 672 p.

15. Descouvemont P. Nuclear Reactions of Astrophysical Interest // Frontiers in Astronomy and Space Sciences. – 2020. – Vol. 7. – 00009.

16. Mohr P. Direct capture cross section of $^{9}$Be($n,\gamma$)$^{10}$Be // Phys. Rev C. – 2019. – Vol. 99. – 0055807.

17. Dubovichenko S., Yeleusheva B., Burkova N., Tkachenko A. The reaction rate of radiative $n^{8}$Li capture in the range from 0.01 to 10 $T_9$ // Frontiers in Astronomy and Space Sciences. – 2023. – Vol. 10. – 1251743.

18. Tkachenko A., Burkova N., Yeleusheva B., Dubovichenko S. Estimation of radiative capture $^{13}$B($n,\gamma_{0+1}$)$^{14}$B reaction rate in the modified potential cluster model // Chinese Physics C. – 2023. – Vol. 47. – 104103.

19. Dubovichenko S., Yeleusheva B., Burkova N., Tkachenko A. Radiative $^{9}$Be($n,\gamma_{0+1+2+3+4+5}$)$^{10}$Be reaction rate in the potential cluster model // Chinese Physics C. – 2023. – Vol. 47. – 084105.

20. Dubovichenko S., Tkachenko A., Kezerashvili Ya., Burkova N., Yeleusheva B. Astrophysical S-factor and reaction rate for $^{15}$N($p,\gamma$)$^{16}$O within the modified potential cluster model // Chinese Physics C. – 2024. – Vol. 48. – 044104.

21. Burkova N.A., Yeleusheva B.M. Reaction rate of radiative n$^{8}$Li capture in the range 0.01 to 10 $T_9$ // XXVII European Academic Science and Research. – 2022. – P. 46-47.

22. Yeleusheva B.M. Dubovichenko S. B., Burkova N. A. Radiative neutron capture on $^{6-8}$Li isotopes in the cluster model // 25$^{th}$ European Conference on Few-Body Problems in Physics (EFB25). – 2023. – P. 87-88.

23. Wildermut K, Tang Y.C. A unified theory of the nucleus. – Braunschweig: Vieweg, 1977. – 399 p.

24. Neudatchin V., Kukulin V., Pomerantsev V., Sakharuk A. Generalized potential-model description of mutual scattering of the lightest p+d, d+$^{3}$He nuclei and the corresponding photonuclear reactions // Phys. Rev. C. – 1992. – Vol. 45. – P. 1512-1527.

25. Kukulin V., Neudatchin V., Obukhovski I. Clusters as Subsystems in Light Nuclei. – Wiesbaden: Vieweg+Teubner Verlag, 1983. – 155 p.

26. Dubovichenko S.B. Thermonuclear processes in stars and Universe. Second Edition. – Saarbrucken: Scholar's Press., 2015. – 332 p.

27. Dubovichenko S.B. Radiative neutron capture and primordial nucleosynthesis of the Universe. First edition. – Berlin: deGruyter, 2019. – 293 p.

28. Itzykson C., Nauenberg M. Unitary groups: Representations and decompositions // Rev. Mod. Phys. – 1966. – Vol. 38. – P. 95-120.

29. Bohr A., Mottelson B.R. Nuclear structure Vol.I. – USA: World Scientific, 1998. – 471 p.

30. Dubovichenko S.B., Uzikov Y.N. Astrophysical S-factors of reactions with light nuclei // Physics of Particles and Nuclei. – 2011. – Vol. 42. – P. 251-301.

31. Dubovichenko S.B, Dzhazairov-Kakhramanov A.V. Study of the nucleon radiative captures $^{8}$Li($n,\gamma$)$^{9}$Li, $^{9}$Be($p,\gamma$)$^{10}$B, $^{10}$Be ($n,\gamma$)$^{11}$Be, $^{10}$B($p,\gamma$)$^{11}$C, and $^{16}$O($p,\gamma$)$^{17}$F at thermal and astrophysical energies // International Journal of Modern Physics E. – 2017. – Vol. 26. – 1630009.

32. Dubovichenko S.B., Burkova N.A., Dzhazairov-Kakhramanov A.V.,

Yertaiuly A. $^{12}B(n,\gamma)^{13}B$ reaction as an alternative path to astrophysical synthesis of $^{13}C$ isotope // Nucl. Phys. A. – 2021. – Vol. 1011. – P. 178-197.

33. Dubovichenko S.B., Dzhazairov-Kakhramanov A.V. Thermonuclear processes for three body system in the potential cluster model // Nucl. Phys. A. – 2015. – Vol. 941. – P. 335-363.

34. Dubovichenko S.B., Dzhazairov-Kakhramanov A.V. Electromagnetic Effects in Light Nuclei and the Potential Cluster Model. I // Physics of Particles and Nuclei. – 1998. – Vol. 28. – P. 615-641.

35. Dubovichenko S.B. Tensor $^{2}H^{4}He$ Interaction and $^{6}Li$ Properties in the Potential Cluster Model // Physics of Atomic Nuclei. – 1998. – Vol. 61. – P. 162-168.

36. Kukulin V., Pomerantsev V., Cooper S., Dubovichenko S. Improved $d$ + $^{4}He$ potentials by inversion: The tensor force and validity of the double folding model // Phys. Rev. C. – 1998. – Vol. 57. – P. 2462-2473.

37. Dubovichenko S.B. Contribution of the $M1$ process to the astrophysical S-factor of the $p^{2}H$ radiative capture // Russian Physics Journal. – 2011. – Vol. 54. – P. 157-164.

38. Dubovichenko S.B. Radiative $n^{2}H$ capture at low energies // Russian Physics Journal. – 2012. – Vol. 55. – P. 138-145.

39. Angulo C., Arnould M., Rayet M., Descauvemont P., Baye D., Leclereq-Willain C., Coc A., Barhoumi S., Aguer P., Rolfs C., Kunz R., Hammer J. W., Mayer A., Paradellis T., Spyrou K. A compilation of charged particle induced thermonuclear reaction rates // Nucl. Phys. A. – 1999. – Vol. 656. – P. 3-183.

40. Mao Z.Q., Champagne A.E. The $^{8}Li(n,\gamma)^{9}Li$ reaction and primordial nucleosynthesis // Nucl. Phys. A. – 1991. – Vol. 522. – P. 568-577.

41. Gupta D., Kundalia K., Ali S.M., Maity S., Mitra R., Tengblad O., Tavora V.G., Saha S.K., Borge M.J., Martel I., Cederkall J., Chishti M., Park J., Moro A.M. Break up of $^{9}Li$ to study the $^{8}Li(n,\gamma)$ reaction // European organization for nuclear research. – 2022. – Vol. 037. – P. 639-646.

42. Malaney R., Fowler W. Origin and distribution of the elements. – Singapore: World Scientific, 1988. – 780 p.

43. Thielemann F. K. Nuclei in the Cosmos. – Vienna: Springer-Verlag, Heildelberg, 1991. – 147 p.

44. Descouvemont P. The $^{8}Li(n,\gamma)^{9}Li$ and $^{8}B(p,\gamma)^{9}C$ mirror reactions in a microscopic cluster model // Astrophys. J. – 1993. – Vol. 405. – P. 518-521.

45. Rauscher T., Applegate J. H., Cowan J. J., Thielemann F. K., Wiescher M. Production of heavy elements in inhomogeneous cosmologies // Astrophys. J. – 1994. – Vol. 429. – P. 499-530.

46. Bertulani C.A. The astrophysical reaction $^{8}Li(n,\gamma)^{9}Li$ from measurements by reverse kinematics // Journal of Physics G: Nuclear and Particle Physics. – 1999. – Vol. 25. – P. 1959-1963.

47. Kobayashi H., Ieki K., Horvath A., Galonsky A., Carlin N., Deak F., Gomi T., Guimaraes V., Higurashi Y., Iwata Y., Kiss A., Kolata J.J., Rauscher T., Schelin H. Astrophysical reaction rate for the $^{8}Li(n,\gamma)^{9}Li$ reaction // Phys. Rev. C. – 2003. – Vol. 67. – 015806.

48. Li Z.H., Liu W.P., Bai X.X., Guo B., Lian G., Yan S.Q., Wang B.X., Zeng

S., Lu Y., Kajino T. The $^{8}$Li(*d*,*p*)$^{9}$Li reaction and the astrophysical $^{8}$Li(*n*,$\gamma$)$^{9}$Li reaction rate // Phys. Rev. C. – 2005. – Vol. 71. – 052801.

49. Guimaraes V., Lichtenthaler R, Camargo O., Barioni A., Kolata J.J., Amro H., Becchetti F.D., Jiang H., Aguilera E.F., Lizcano D., Martines-Quiroz E., Garcia H. Neutron transfer reactions induced by $^{8}$Li on $^{9}$Be // Phys. Rev. C. – 2007. – Vol. 75. – 054602.

50. Banerjee P., Chatterjee R., Shyam R. Coulomb dissociation of $^{9}$Li and the rate of the $^{8}$Li(*n*,$\gamma$)$^{9}$Li reaction // Phys. Rev. C. – 2008. – Vol. 78. – 035804.

51. Ma H., Dong B., Yan Y., Zhang X. Shell model study on the astrophysical neutron capture of $^{8}$Li // The European Physical Journal A. – 2012. – Vol. 48. – 12125.

52. McCracken C., Navratil P., McCoy A., Quaglioni S., Hupin G. Microscopic investigation of the $^{8}$Li(n,$\gamma$)$^{9}$Li reaction // Phys. Rev. C. – 2021. – Vol. 103. – 035801.

53. Dong G.X., Wang X.B., Michel N., Ploszajczak M. Gamow shell model description of the radiative capture reaction $^{8}$Li(n,$\gamma$)$^{9}$Li // Phys. Rev. C. – 2022. – Vol. 105. – 049902.

54. Paradellis T., Kossionides S., Doukellis G., Aslanoglou X., Assimakopoulos P., Pakou A., Rolfs C., Langanke K. Astrophysical S(E) factor of $^{8}$Li($\alpha$,$n_0$)$^{11}$B and inhomogeneous Big Bang nucleosynthesis // Zeitschrift fur Physik A Atomic Nuclei. – 1990. – Vol. 337. – P. 211-220.

55. Cherubini S., Figuera P., Musumarra A., Agodi C., Alba R., Calabretta L., Cosentino L., Del Zoppo A., Di Pietro A., Lamia L., Pappalardo L., Pizzone R.G. $^{8}$Li($\alpha$,n)$^{11}$B at Big Bang Temperatures: Neutron Counting With a Low Intensity $^{8}$Li Radioactive Beam // AIP Conference Proceedings. – 2004. – Vol. 701 – P. 68-72.

56. Su-Qing H., Kai-Su W., Yong-Shou C., Neng-Chuan S., Zhi-Hong L. The Main Path to C, N, O Elements in Big Bang Nucleosynthesis // Chinese Physics Letters. – 2010. – Vol. 27. – 082601.

57. La Cognata M., Del Zoppo A. The $^{8}$Li($\alpha$,n)$^{11}$B reaction rate at astrophysical temperatures // Astrophys. J. – 2011. – Vol. 736. – P. 148-152.

58. Das S.K., Fukuda T., Mizoi Y., Ishiyama H., Miyatake H., Watanabe Y. X., Hirayama Y., Jeong S.C., Hashimoto T. New measurement of the $^{8}$Li($\alpha$,n)$^{11}$B reaction in a lower-energy region below the Coulomb barrier // Phys. Rev. C. – 2017. – Vol. 95. – 055805.

59. Dubovichenko S.B., Dzhazairov-Kakhramanov A.V. The reaction $^{8}$Li(n,$\gamma$)$^{9}$Li at astrophysical energies and its role in primordial nucleosynthesis // Astrophys. J. – 2016. – Vol. 819. – P. 78-86.

60. Burkova N.A., Dubovichenko S.B., Dzhazairov-Kakhramanov A.V., Nurakhmetova S.Z. Comparative role of the $^{7}$Li(n,$\gamma$)$^{8}$Li reaction in Big Bang nucleosynthesis // Journal of Physics G: Nuclear and Particle Physics. – 2021. – Vol. 48. – 045201.

61. Tilley D.R., Cheves C.M., Hale G.M., Hofmann H.M. Energy levels of light nuclei A = 5, 6, 7 // Nuclear Physics A. – 2002. – Vol. 708. – P. 3-163.

62. Sukhoruchkin S.I., Soroko Z.N. Excited nuclear states. – Berlin: Springer, 2012. – 5235 p.

63. Dubovichenko S.B. Methods for calculating nuclear characteristics.

Nuclear and thermonuclear processes. Second edition. – Saarbrucken: Lambert Acad. Publ. GmbH&Co., 2012. – 425 p.

64. Dubovichenko S.B., Dzhazairov-Kakhramanov A.V, Afanasyeva N.V. New results for reaction rate of the proton radiative capture on $^{3}$H // Nucl. Phys. A. – 2017. – Vol. 963. – P. 52-67.

65. Guimaraes V., Camargo O., Lichtenthaler R., Barioni A., Kolata J.J., Amro H., Becchetti F.D., Jiang H., Aguilera E.F., Lizcano D., Garcia H. Investigation of Nucleosynthesis Capture Reactions by Using $^{8}$Li Radioactive Beam Transfer reactions. // Proceedings of International Symposium on Nuclear Astrophysics - Nuclei in the Cosmos - IX (NIC-IX). – 2010. – Vol. 28. – P. 108-115.

66. Timofeyuk N.K. Spectroscopic factors and asymptotic normalization coefficients for 0p-shell nuclei: Recent updates // Phys. Rev. C. – 2013. – Vol. 88. – 44315.

67. Mukhamedzhanov A.M., Timofeyuk N.K. Microscopic calculation of nucleon separation vertex constant for 1p shell nuclei // Journal of Soviet Nuclear Physics. –1990. – Vol. 51. – P. 431-441.

68. Huang J.T., Bertulani C.A., Guimaraes V. Radiative capture of nucleons at astrophysical energies with single-particle states // At Data Nucl. Data Tables. – 2010. – Vol. 96. – P. 824-847.

69. Sanchez R., Nortershauser W., Dax A., Ewald G., Gotte S., Kirchner R., Wojtaszek A., Zimmermann C. Nuclear charge radius of $^{11}$Li // Laser Conf. – 2007. – Vol. 171 – P. 181-188.

70. Nortershauser W., Bushaw B.A., Dax A., Drake G., Ewald G., Gotte S., Kirchner R., Sanchez R., Zimmermann C. Measurement of the nuclear charge radii of $^{8,9}$Li // The European Physical Journal A. – 2005. – Vol. 25. – P. 199-200.

71. Dubovichenko S., Burkova N., Tkachenko A. Reaction rate of radiative $n^{6}$Li capture in the temperature range from 0.01 to 10 $T_9$ // Nucl. Phys. A. – 2022. – Vol. 1027. – 122520.

72. Wuosmaa A.H., Rehm K.E., Greene J.P., Henderson D.J., Janssens R.V., Jiang C.L., Jisonna L., Moore E.F., Pardo R.C. Neutron Spectroscopic Factors in $^{9}$Li from $^{2}$H($^{8}$Li,p)$^{9}$Li // Phys. Rev. Lett. – 2005. – Vol. 94. – 082502.

73. Wiringa R.B. Spectroscopic Overlaps. URL: http://www.phy.anl.gov/theory/research/overlap (accessed: 30.05.2023).

74. Kanungo R., Andreyev A.N., Buchmann L., Davids B., Hackman G., Howell D., Khalili P., Mills B., Padila Rodal E., Pieper S.C., Pearson J., Ruiz C., Ruprecht G., Shotter A., Tanihata I. Spectroscopic factors for the $^{9}$Li ground state and N=6 shell closure // Physics Letters B. – 2008. – Vol. 660. – P. 26-31.

75. Firestone R.B., Revay Z. Thermal neutron radiative cross sections for $^{6,7}$Li, $^{9}$Be, $^{10,11}$B, $^{12,13}$C, and $^{14,15}$N // Phys. Rev. C. – 2016. – Vol. 93. – P. 054306.

76. Norman E.B., Schramm D.N. On the Conditions Required for the r-Process // Astrophys. Jour. – 1979. – Vol. 228. – P. 881-892.

77. Nuclear Data Evaluation Project. $^{8}$Li β-Decay Evaluated Data. URL: https://nucldata.tunl.duke.edu/nucldata/GroundStatedecays/08Li.shtml#halflife (accessed: 25.04.2023).

78. Dubovichenko S.B., Burkova N.A., Dzhazairov-Kakhramanov A.V.

Influence of low-lying resonances on reaction rates for $^{10}B(n,\gamma)^{11}B$ capture // Nucl. Phys. A. – 2019. – Vol. 992. – 121625.

79. Kubono S., Yamaguchi H., Hayakawa S., Hou S.Q., He J.J. Explosive Nuclear Burning in the pp-Chain Region and the Breakout Processes // EPJ Web Conf. – 2016. – Vol. 109. – 01001.

80. Caughlan G.R., Fowler W.A. Thermonuclear reaction rates V // At. Data Nucl. Data Tables. – 1988. – Vol. 40. – P. 283-334.

81. Malaney R.A., Fowler W.A. On nuclear reactions and $^{9}Be$ production in inhomogeneous cosmologies // Astrophys. J. – 1989. – Vol. 345. – P. 5-8.

82. Kajino T., Mathews G.J., Fuller G.M. Primordial nucleosynthesis of intermediate-mass elements in baryon-number-inhomogeneous big bang models: Observational tests // Astrophys. J. – 1990. – Vol. 364. – P. 7-14.

83. Reeves H. On the origin of the light elements (Z<6) // Rev. Mod. Phys. – 1994. – Vol. 66. – P. 193-216.

84. Fukuda K., Hiyagon H., Fujiya W., Takahata N., Kagoshima T., Sano Y. Origin of the Short-lived Radionuclide $^{10}Be$ and Its Implications for the Astronomical Setting of CAI Formation in the Solar Protoplanetary Disk // Astrophys J. – 2019. – Vol. 886. – P. 34-45.

85. Coc A., Vangioni E. Primordial nucleosynthesis // Int. Jour. Mod. Phys. E. – 2017. – Vol. 26. – P. 12-24.

86. Wallner A., Bichler M., Coquard L., Dillmann I., Forstner O., Golser R., Heil M., Kappeler F., Kutschera W., Lederer-Woods C., Martschini M., Mengoni A., Merchel A., Wiescher M. Stellar and thermal neutron capture cross section of $^{9}Be$ // Phys. Rev. C. – 2019. – Vol. 99. – 015804.

87. Dubovichenko S.B., Dzhazairov-Kakhramanov A.V., Burkova N.A. New theoretical results for radiative $^{3}H(p,\gamma)^{4}He$, $^{3}He(^{2}H,\gamma)^{5}Li$, $^{4}He(^{2}H,\gamma)^{6}Li$, $^{4}He(^{3}H,\gamma)^{7}Li$, and $^{4}He(^{3}He,\gamma)^{7}Be$ captures at astrophysical energies // International Journal of Modern Physics E. – 2019. – Vol. 28. – 1930004.

88. Dubovichenko S.B., Burkova N.A., Dzhazairov-Kakhramanov A.V., Tkachenko A.S. Influence of resonances on the $^{11}B(n,\gamma)^{12}B$ capture reaction rate. Capture to the ground state of $^{12}B$ // Astroparticle Physics. – 2020. – Vol. 123. – 102481.

89. Dubovichenko S.B., Burkova N.A., Dzhazairov-Kakhramanov A.V. Influence of resonances on the $^{11}B(n,\gamma)^{12}B$ reaction rate. Capture to the excited states of $^{12}B$ // International Journal of Modern Physics E. – 2023. – Vol. 32. – 102481.

90. Dubovichenko S.B. Capture of a neutron to excited states of a $^{9}Be$ nucleus taking into account resonance at 622 keV // Journal of Experimental and Theoretical Physics. – 2013. – Vol. 117. – P. 649-655.

91. Conneely C.M., Prestwich W.V., Kennett T.J. The thermal neutron capture cross section of $^{9}Be$ // Nucl. Instrum. Methods Phys. Res. A. – 1986. – Vol. 248. – P. 416-418.

92. Wallner A., Coquard L., Dillmann I., Forstner O., Golser R., Heil M., Kaeppeler F., Kutschera W., Mengoni A., Michlmayr L., Priller A., Steier P., Wiescher M. Measurement of the stellar cross sections for the reactions $^{9}Be(n,\gamma)^{10}Be$ and $^{13}C(n,\gamma)^{14}C$ via AMS // Journal of Physics G: Nuclear and Particle Physics. – 2008. –

Vol. 35. – 014018.

93. Wallner A. Nuclear astrophysics and AMS – Probing nucleosynthesis in the lab // Nucl. Instrum. Methods Phys. Res. B. – 2010. – Vol. 268. – P. 1277-1282.

94. Marin-Lambarri D.J., Garcia-Ramirez J., Sanchez-Zuniga E., Padilla S., Acosta L., Chavez E., Cruz-Galindo H.S., Huerta A., Mendez G. Measurement of the thermal neutron capture cross section by $^{9}$Be using the neutron flux from a nuclear research reactor and the AMS technique // Phys. Rev. C. – 2020. – Vol. 102. – 044601.

95. Elliott J.P. Collective motion in the nuclear shell model I. Classification schemes for states of mixed configurations // Proc. R. Soc. Lond. A. Math. Phys. Sci. – 1958. – Vol. 245. – P. 128-145.

96. Elliott J.P. Collective motion in the nuclear shell model II. The introduction of intrinsic wave-functions // Proc. R. Soc. Lond. A. Math. Phys. Sci. – 1958. – Vol. 245. – P. 562-581.

97. Tilley D.R., Kelley J.H., Godwin J.L., Millener D.J., Purcell J.E., Sheu C.G., Weller H.R. Energy levels of light nuclei A=8, 9, 10 // Nucl. Phys. A. – 2004. – Vol. 745. – P. 155-362.

98. Sukhoruchkin S.I. Supplement to I/25 A-F. – Berlin: Springer Heidelberg, 2016. – 6634 p.

99. Bockelman C.K., Miller D.W., Adair R.K., Barschall H.H. Total Cross Sections of Light Nuclei for p, T-Neutron // Phys. Rev. – 1951. – Vol. 84. – P. 69-75.

100. Lukyanov S.M., Denikin A.S., Voskoboynik E.I., Khlebnikov S.V., Harakeh M.N., Maslov V., Penionzhkevich Y.E., Sobolev Yu.G., Trzaska W.H. Study of internal structures of $^{9,10}$Be and $^{10}$B in scattering of $^{4}$He from $^{9}$Be // Journal of Physics G: Nuclear and Particle Physics. – 2014. – Vol. 41. – 035102.

101. Schmidt-Rohr U., Stock R., Turek P. Die winkelverteilungen der protonen aus den reaktionen $^{9}$Be(d,p)$^{10}$Be, $^{12}$C(d,p)$^{13}$C, $^{16}$O(d,p)$^{17}$O und $^{40}$Ca(d,p)$^{41}$Ca bei 11.8 MeV // Nucl. Phys. – 1964. – Vol. 53. – P. 77-86.

102. Cohen S., Kurath D. Spectroscopic factors for the 1p shell // Nucl. Phys. A. – 1967. – Vol. 101. – P. 1-16.

103. Anderson R.E. A study of the higher excited states of $^{10}$Be from the $^{9}$Be(d,p)$^{10}$Be reaction // Nucl. Phys. A. – 1974. – Vol. 236. – P. 77-89.

104. Mughabghab S.F. Evidence for a Nucleon-Nucleus Spin-Spin Interaction in $^{9}$Be // Phys. Rev. Lett. – 1985. – Vol. 54. – P. 986-988.

105. Ogawa Y., Arai K., Suzuki Y., Varga K. Microscopic four-cluster description of $^{10}$Be and $^{10}$C with the stochastic variational method // Nucl. Phys. A. – 2000. – Vol. 673. – P. 122-142.

106. Lee J., Tsang M.B., Lynch W.G. Neutron spectroscopic factors from transfer reactions // Phys. Rev. C. – 2007. – Vol. 75. – 064320.

107. Darden S.E., Murillo G., Sen S. The $^{9}$Be(d,p)$^{9}$Be, $^{9}$Be(d,p)$^{10}$Be, $^{9}$Be(d,t)$^{8}$Be and $^{9}$Be(d,p)$^{8}$Be reactions at 15 MeV // Nucl. Phys. A. – 1976. – Vol. 266. – P. 29-52.

108. Harakeh M.N., van Popta J., Saha A., Siemssen R.H. Strong coupled-channels effects in the $^{9}$Be(α,t)$^{10}$B reaction // Nucl. Phys A. – 1980. – Vol. 344. – P. 15-40.

109. Grinyer G.F., Bazin D., Gade A., Tostevin J.A., Adrich P., Bowen M.D.,

Brown B.A., Campbell C.M., Cook J.M. Knockout Reactions from p-Shell Nuclei: Tests of Ab Initio Structure Models // Phys. Rev. Lett. – 2011. – Vol. 106. – 162502.

110. Nuclear Wallet Cards. URL: https://www.nndc.bnl.gov/nudat3/indx_sigma.jsp (accessed: 13.12.2024).

111. Fundamental Physical Constants. URL: https://physics.nist.gov/cuu/Constants/index.html (accessed: 01.06.2023).

112. Ozawa A., Suzuki T., Tanihata I. Nuclear size and related topics // Nucl. Phys. A. – 2001. – Vol. 693. – P. 32-62.

113. Nortershauser W., Tiedemann D., Zakova M., Andjelkovic Z., Blaum K., Bissell M.L., Cazan R., Drake G.W., Geppert Ch. Nuclear Charge Radii of $^{7,9,10}$Be and the One-Neutron Halo Nucleus $^{11}$Be // Phys. Rev. Lett. – 2009. – Vol. 102. – 062503.

114. Descouvemont P., Itagaki N.A stochastic microscopic approach to the $^{10}$Be and $^{11}$Be nuclei // Prog. Theor. Exp. Phys. – 2020. – Vol. 2020. – 023D02.

115. Liatard E., Bruandet J.F., Glasser F., Kox S., Chan T.U., Costa G.J., Heitz C., El Masri Y., Hanappe F., Bimbot R., Guillemaud-Mueller D., Mueller A.C. Matter Distribution in Neutron-Rich Light Nuclei and Total Reaction Cross-Section // Europhysics Letters (EPL). – 1990. – Vol. 13. – P. 401-404.

116. Wang J.S., Shen W.Q., Zhu Z.Y., Feng J., Guo Z.Y., Zhan W.L., Xiao G.Q., Cai X.Z., Fang D.Q., Zhang H.Y., Ma Y.G. RMF calculation and phenomenological formulas for the rms radii of light nuclei // Nucl. Phys. A. – 2001. – Vol. 691. – P. 618-630.

117. Ahmad S., Usmani A.A., Khan Z.A. Matter radii of light proton-rich and neutron-rich nuclear isotopes // Phys. Rev. C. – 2017. – Vol. 96. – 064602.

118. Dubovichenko S.B., Tkachenko A.S., Kezerashvili R.Ya., Burkova N.A., Dzhazairov-Kakhramanov A.V. $^{6}$Li(p,γ)$^{7}$Be reaction rate in the light of the new data of the laboratory for Underground Nuclear Astrophysics // Phys. Rev. C. – 2022. – Vol. 105. – 065806.

119. Shibata S. PhD Thesis (in Japanese, unpublished) – 1992. – 106 p.

120. Acosta L., Amador-Valenzuela P., Andrade E., Barron-Palos L., Belmont D., Charon L., Chavez E., Cruz-Galindo H., Garcia-Ramirez J., Huerta A., Marin-Lambarri D.J., Martinez J.N., Mas-Ruiz J., Mendez C.G. The AMS technique as an important tool for the measurement of astrophysical cross sections // EPJ Web Conf. – 2021. – Vol. 252. – 05003.

121. Rauscher T. Stellar neutron capture reactions at low and high temperature // The European Physical Journal A. – 2022. – Vol. 58. – P. 214-224.

122. Herndl H., Hofinger R., Jank J., Oberhummer H., Gorres J., Wiesher M. Reaction rates for neutron capture reactions to C, N, and O isotopes to the neutron rich side of stability // Phys. Rev. C. – 1999. – Vol. 60. – 064614.

123. Mengoni A., Otsuka T., Ishihara M. Direct radiative capture of *p* -wave neutrons // Phys. Rev. C. – 1995. – Vol. 52. – R2334.

124. Arnould M., Goriely S. Astronuclear Physics: A tale of the atomic nuclei in the skies // Prog. Part. Nucl. Phys. – 2020. – Vol. 112. – 103766.

125. Chatterjee R., Dan M. Status of nuclear physics behind nucleosynthesis processes: The role of exotic neutron-rich nuclei // Journal of Astrophysics and Astronomy. –2020. – Vol. 41. – P. 51-57.

126. Sasaqui T., Kajino T., Mathews G.J., Otsuki K., Nakamura T. Sensitivity of *r* -Process Nucleosynthesis to Light-Element Nuclear Reactions // Astrophys. J. – 2005. – Vol. 634. – P. 1173-1189.

127. Dubovichenko S.B., Burkova N.A. Rate of Radiative $n^{12}C$ Decay at Temperatures from 0.01 $T_9$ to 10 $T_9$ // Russian Physics Journal. – 2021. – Vol. 64. – P. 216-227.

128. Dubovichenko S.B. The $n^{13}C$ capture reaction rate // Russian Physics Journal. –2022. – Vol. 65. – P. 208-215.

129. Dubovichenko S.B., Dzhazairov-Kakhramanov A.V., Afanasyeva N.A. Radiative neutron capture on $^{9}$Be, $^{14}$C, $^{14}$N, $^{15}$N and $^{16}$O at thermal and astrophysical energies // International Journal of Modern Physics E. – 2013. – Vol. 22. – 1350075.

130. Nagai Y., Kinoshita M., Igashira M., Nobuhara Y., Makii H., Mishima K., Shima T., Mengoni A. Nonresonant p-wave direct capture and interference effect observed in the $^{16}O(n,\gamma)^{17}O$ // Phys. Rev. C. – 2020. –Vol. 102. – 044616.

131. Ajzenberg-Selove F. Energy levels of light nuclei A = 13–15 // Nucl. Phys. A. –1991. – Vol. 523. – P. 1-196.

132. Dubovichenko S.B. Thermonuclear processes in Stars and Universe. Fourth Russian Edition corrected and enlarged. – Saarbrucken: Lambert Academy Publ. GmbH&Co, 2019. – 495 p.

133. Kurdyumov I.V., Smirnov Yu.F., Shitikova K.V., Samarai S. Translationally invariant shell model // Nucl. Phys. A. – 1970. – Vol. 145. – P. 593-612.

134. Volya A., Tchuvilsky Y.M. Nuclear clustering using a modern shell model approach // Phys. Rev. C. – 2015. – Vol. 91. – 044319.

135. Plattner G.R., Viollier R.D. Coupling constants of commonly used nuclear probes // Nucl. Phys. A. – 1981. – Vol. 365. – P. 8-12.

136. Guimaraes V. Nuclear reaction studies with exotic boron beams // Brazilian Journal of Physics. – 2004. – Vol. 34. – P. 1012-1016.

137. Bedoor S., Wuosmaa A., Lighthall J., Alcorta M., Back B., Bertone P., Brown B., Deibel C., Hoffman C. Structure of $^{14}$B and the evolution of $N$=9 single-neutron isotones // Phys. Rev. C. – 2013. – Vol. 88. – 011304.

138. Guimaraes V., Kolata J., Bazin D., Blank B., Brown B., Glasmacher T., Hansen P., Ibbotson R., Karnes D., Maddalena V., Navin A. Spectroscopy of $^{13,14}$B via the one-neutron knockout reaction // Phys. Rev. C. – 2000. – Vol. 6. – 064609.

139. Assenbaum H.J., Langanke K., Rolfs C. Effects of electron screening on low-energy fusion cross sections // Zeitschrift fur Physik A Atomic Nuclei. – 1987. – Vol. 327. – P. 461-468.

140. Estrade A., Kanungo R., Horiuchi W., Ameil F., Atkinson J., Ayyad Y., Dillmann I., Evdokimov A. Proton Radii of $^{12-17}$B Define a Thick Neutron Surface in $^{17}$B // Phys. Rev. Lett. – 2014. – Vol. 113. – 132501.

141. Bertulani C.A., Kajino T. Frontiers in nuclear astrophysics // Prog. Part. Nucl. Phys. – 2016. – Vol. 89. – P. 56-100.

142. National Nuclear Data Center. URL: https://www.nndc.bnl.gov/nudat3 (accessed: 01.02.2025)

143. TUNL Nuclear Data Project. URL:

https://nucldata.tunl.duke.edu/nucldata/GroundStatedecays/14B.shtml (accessed: 01.01.2025)

144. Barnes C.A., Clayton D.D., Schramm D.N. Essays in Nuclear Astrophysics. – Cambridge University Press, 1982 – 562 p.

145. Adelberger E.G., Garcia A., Robertson H., Snover K. Solar fusion cross sections. II. The pp chain and CNO cycles // Rev. Mod. Phys. – 2011. – Vol. 83. – P. 195-245.

146. Wiescher M., Gorres J., Uberseder E., Imbriani G., Pignatari M. The Cold and Hot CNO Cycles // Annual Review of Nuclear and Particle Science. – 2010. – Vol. 60. – P. 381-404.

147. deBoer R.J., Gorres J., Imbriani G., LeBlanc P.J., Uberseder E., Wiescher M. R-matrix analysis of $^{16}$O compound nucleus reactions // Phys. Rev. C. – 2013. – Vol. 87. – 015802.

148. Caciolli A., Mazzocchi C., Capogrosso V., Bemmerer D., Corvisiero P., Costantini H., Elekes Z., Formicola A., Fulop Zs., Gervino G., Guglielmetti A., Gustavino C., Imbriani G., Junker M., Lemut A., Marta M., Menegazzo R., Palmerini S., Prati P., Roca V., Rolfs C. Revision of the $^{15}$N(p,γ)$^{16}$O reaction rate and oxygen abundance in H-burning zones // Astron. Astrophys. – 2011. – Vol. 533. – P. 66-72.

149. Boeltzig A., Bruno C.G., Cavanna F., Cristallo S., Davinson T., Depalo R., DeBoer R.J., Di Leva A., Ferraro F., Imbriani G., Marigo P., Terrasi F., Wiescher M. Shell and explosive hydrogen burning // The European Physical Journal A. – 2016. – Vol. 52. – P. 75-88.

150. Caughlan G.R., Fowler W.A. The Mean Lifetimes of Carbon, Nitrogen, and Oxygen Nuclei in the CNO Bicycle. // Astrophys. J. – 1962. – Vol. 136. – P. 453-464.

151. Harris M.J., Fowler W., Caughlan R., Zimmerman B. Thermonuclear Reaction Rates, III // Ann. Rev. Astron. Astrophys. – 1983. – Vol. 21. – P. 165-176.

152. Schardt A., Fowler W.A., Lauritsen C.C. The Disintegration of N$^{15}$ by Protons // Phys. Rev. – 1952. – Vol. 86. – P. 527-535.

153. Hebbard D.F. Proton capture by N$^{15}$ // Nuclear Physics. – 1960. – Vol. 15. – P. 289-315.

154. Rolfs C., Rodney W.S. Proton capture by $^{15}$N at stellar energies // Nucl. Phys. A. – 1974. – Vol. 235. – P. 450-459.

155. Brochard F., Chevallier P., Disdier D., Rauch V., Scheibling F. Étude des désexcitations électromagnétiques des niveaux 1- situés à 12,44 et 13,09 MeV dans le noyau $^{16}$O // Journal de Physique. – 1973. – Vol. 34. – P. 363-367.

156. Bemmerer D., Caciolli A., Bonetti R., Broggini C., Confortola F., Corvisiero P., Costantini H., Elekes Z., Formicola A. Direct measurement of the $^{15}$N(p,γ)$^{16}$O total cross section at novae energies // Journal of Physics G: Nuclear and Particle Physics. – 2009. – Vol. 36 – 045202.

157. LeBlanc P.J., Imbriani G., Gorres J., Junker M., Azuma R., Beard M., Bemmerer D., Best A., Broggini C. Constraining the S factor of N$^{15}$ at astrophysical energies // Phys. Rev. C. – 2010. – Vol. 82. – 055804.

158. Imbriani G., deBoer R.J., Best A., Couder M., Gervino G., Gorres J., LeBlanc P.J., Leiste H., Lemut A., Stech E., Strieder F., Uberseder E., Wiescher M.

Measurement of γ $^{15}N(p,\gamma)^{16}O$ cascade and $^{15}N(p,\alpha)^{12}C$ reactions // Phys. Rev. C. – 2012. – Vol. 85. – 065810.

159. Xu Y., Takahashi K., Goriely S., Arnould M., Ohta M., Utsunomiya H. NACRE II: An update of the NACRE compilation of charged-particle-induced thermonuclear reaction rates for nuclei with mass number A < 16 // Nucl. Phys A. – 2013. – Vol. 918. – P. 61-169.

160. Barker F.C. $^{15}N(p,\gamma_0)^{16}O$ S-factor // Phys. Rev. C. – 2008. – Vol. 78. – 044612.

161. Mukhamedzhanov A.M., Bem P., Burjan V., Gagliardi C., Goldberg V. Z., Hons Z., La Cognata M., Mrazek J., Novak J. New astrophysical S factor for the normal $^{15}N(p,\gamma)^{16}O$ reaction via the asymptotic normalization coefficient (ANC) method // Phys. Rev. C. – 2008. – Vol. 78. – 015804.

162. Dubovichenko S.B, Dzhazairov-Kakhramanov A.V. Study of the neutron and proton capture reactions $^{10,11}B(n,\gamma)$, $^{11}B(p,\gamma)$, $^{14}C(p,\gamma)$, and $^{15}N(p,\gamma)$ at thermal and astrophysical energies // International Journal of Modern Physics E. – 2014. – Vol. 23. – 1430012.

163. Mukhamedzhanov A.M., La Cognata M., Kroha V. Astrophysical S factor for the $^{15}N(p,\gamma)^{16}O$ reaction // Phys. Rev. C. – 2011. – Vol. 83. – 044604.

164. Li X.Z., Tian J., Mei M.Y., Li C.X. Sub-barrier fusion and selective resonant tunneling // Phys. Rev. C. – 2000. – Vol. 61. – 024610.

165. Mondal S.H., Khan M.A. Study of fusion cross-section and astrophysical S-factor for $p+^{15}N$ and $\alpha+^{12}C$ at sub-barrier energy // International Journal of Modern Physics E. – 2022. – Vol. 31. – P. 1-10.

166. Son S., Ando S.I., Oh Y. Determination of Astrophysical S-factor for $^{15}N(p,\gamma)^{16}O$ at Low-energies Within Effective Field Theory // New Physics: Sae Mulli. – 2022. – Vol. 72. – P. 291-295.

167. Son S., Ando S.I., Oh Y. Radiative proton capture on $^{15}N$ within effective field theory // Phys. Rev. C. – 2022. – Vol. 106. – 055807.

168. Dubovichenko S.B., Kezerashvili R.Ya., Burkova N.A., Dzhazairov-Kakhramanov A.V. Beisenov B. Reanalysis of the $^{13}N(p,\gamma)^{14}O$ reaction and its role in the stellar CNO cycle // Phys. Rev. C. – 2020. – Vol. 102. – 045805.

169. Tilley D.R., Weller H.R., Cheves C.M. Energy levels of light nuclei A = 16-17 // Nucl. Phys. A. – 1993. – Vol. 564. – P. 1-183.

170. Gorodetzky S., Adloff J., Brochard F., Chevallier P., Disdier D., Gorozdetsky P., Modjtahed-Zadeh R., Scheibling F. Cascades γ-γ de quatre résonances de la réaction $^{15}N(p,\gamma)^{16}O$ // Nucl. Phys. A. – 1968. – Vol. 113. –P. 221-232.

171. Imbriani G., deBoer R., Best A., Couder M., Gervino G., Gorres J., LeBlanc P., Leiste H., Lemut A. Erratum: Measurement of γ rays from $^{15}N(p,\gamma)^{16}O$ cascade and $^{15}N\ (p,\alpha_1\gamma)^{12}C$ reactions // Phys. Rev. C. – 2012. – Vol. 86. – 039902.

172. deBoer R.J., LeBlanc P.J., Falahat S., Imbriani G., Gorres J., O'Brien S., Uberseder E., Wiescher M. Elastic scattering of protons from $^{15}N$ // Phys. Rev. C. – 2012. – Vol. 85. – 038801.

173. Bashkin S., Carlson R.R. Gamma rays from proton bombardment of $^{6}Li$ // Phys. Rev. – 1955. – Vol. 97. – P. 1245-1249.

174. Hanna S., Glavish H., Avida R., Calarco J., Kuhlmann E., LaCanna R.

Evidence for a Giant Quadrupole Resonance in $^{16}$O // Phys. Rev. Lett. – 1974. – Vol. 32. –P. 114-117.

175. Darden S.E. $^{15}$N(p,$p_0$)$^{15}$N and the levels of $^{16}$O for $E_x$ = 14.8–18.6 MeV // Nucl. Phys. A. – 1984. – Vol. 429. – P. 218-258.

176. Rolfs C., Azuma R.E. Interference effects in $^{12}$C(p,γ)$^{13}$N and direct capture to unbound states // Nucl. Phys. A. – 1974. – Vol. 227. – P. 291-308.

177. Rolfs C. Spectroscopic factors from radiative capture reactions // Nucl. Phys. A. –1973. – Vol. 217. – P. 29-70.

178. Mukhamedzhanov A.M., Blokhintsev L.D. Asymptotic normalization coefficients in nuclear reactions and nuclear astrophysics // The European Physical Journal A. – 2022. – Vol. 58. – P. 29-39.

179. Mukhamedzhanov A.M. Resonances in low-energy nuclear processes and nuclear astrophysics and asymptotic normalization coefficients: a review // The European Physical Journal A. – 2023. – Vol. 59. – P. 43-46.

180. Karr J., Marchand D., Voutier E. The proton size // Nature Reviews Physics. – 2020. – Vol. 2. – P. 601-614.

181. Xu H.M., Gagliardi C.A., Tribble R.E., Mukhamedzhanov A.M., Timofeyuk N.K. Overall Normalization of the Astrophysical S-factor and the Nuclear Vertex Constant for $^{7}$Be(p,γ)$^{8}$B Reactions // Phys. Rev. Lett. – 1994. – Vol. 73. – P. 2027-2030.

182. Mukhamedzhanov A.M., Tribble R.E., Timofeyuk N.K. Possibility to determine the astrophysical S-factor for the $^{7}$Be(p,γ)$^{8}$B radiative capture from analysis of the $^{7}$Be($^{3}$He,d)$^{8}$B reaction // Phys. Rev. C. – 1995. – Vol. 51. – P. 3472-3478.

183. Mukhamedzhanov A.M., Gagliardi C.A., Tribble R.E. Asymptotic normalization coefficients, spectroscopic factors, and direct radiative capture rates // Phys. Rev. C. – 2001. – Vol. 63. – 024612.

184. Timofeyuk N.K., Johnson R.C., Mukhamedzhanov A.M. Relation between Proton and Neutron Asymptotic Normalization Coefficients for Light Mirror Nuclei and its Relevance to Nuclear Astrophysics // Phys. Rev. Lett. – 2003. – Vol. 91. – 232501.

185. Mukhamedzhanov A.M., Bem P., Brown B.A., Burjan V., Kroha V., Novak J., Nunes F.M. Asymptotic normalization coefficients for $^{14}$N + p$^{15}$O and the astrophysical S-factor for $^{14}$N(p,γ)$^{15}$O // Phys. Rev. C. – 2003. – Vol. 67. – 065804.

186. Timofeyuk N.K. New Insight into the Observation of Spectroscopic Strength Reduction in Atomic Nuclei: Implication for the Physical Meaning of Spectroscopic Factors // Phys. Rev. Lett. – 2009. – Vol. 103. – 242501.

187. Tribble R.E., Bertulani C.A., La Cognata M., Mukhamedzhanov A.M., Spitaleri C. Indirect techniques in nuclear astrophysics: a review // Reports on Progress in Physics. – 2014. – Vol. 77. – 106901.

188. Blokhintsev L.D., Savin D.A. Study of the Influence of Different Methods of Taking into Account the Coulomb Interaction on Determining Asymptotic Normalization Coefficients within the Framework of Exactly Solvable Model // Physics of Atomic Nuclei. – 2021. – Vol. 84. – P. 401-407.

189. Plattner G.R., Viollier R.D. Coupling constants of commonly used nuclear probes // Nucl. Phys. A. – 1981. – Vol. 365. – P. 8-12.

190. Centre for photonuclear experiments data. URL: http://cdfe.sinp.msu.ru (accessed: 28.04.2024).

191. Wiescher M., Kappeler F., Langanke K. Critical Reactions in Contemporary Nuclear Astrophysics // Annu. Rev. Astron. Astrophys. – 2012. – Vol. 50. – P. 165-210.

192. Dubovichenko S.B., Burkova N.A., Dzhazairov-Kakhramanov A.V., Beysenov B. Reaction rate of $p^{14}N \rightarrow^{15}O\gamma$ capture to all bound states in potential cluster model // International Journal of Modern Physics E. – 2020. – Vol. 29. – 1930007.

193. Dubovichenko S.B., Burkova N.A., Zazulin D.M. Reaction rate of radiative $p^{12}N$ capture // Nucl. Phys. A. – 2022. – Vol. 1028. – 122543.

194. Costantini H., Formicola A., Imbriani G., Junker M., Rolfs C., Strieder F. LUNA: a laboratory for underground nuclear astrophysics // Reports on Progress in Physics. – 2009. – Vol. 72. – 086301.

195. Skowronski J., Gesue R.M., Boeltzig A., Ciani G.F., Piatti D., Rapagnani D., Aliotta M., Ananna C., Barile F., Bemmerer D., Best A. Advances in radiative capture studies at LUNA with a segmented BGO detector // Journal of Physics G: Nuclear and Particle Physics. – 2023. – Vol. 50. – 045201.

196. Lemut A., Bemmerer D., Confortola F., Bonetti R., Broggini C., Corvisiero P., Costantini H., Cruz J., Formicola A., Fulop Zs., Gervino G., Guglielmetti A., Gustavino C., Limata B. First measurement of the $^{14}N(p,\gamma)^{15}O$ cross section down to 70 keV // Physics Letters B. – 2006. – Vol. 634. – P. 483-487.